

# **Oxide Based Functional Materials through Solid State and Electrochemical Synthesis**

Von der Fakultät Chemie der Universität Stuttgart  
Zur Erlangung der Würde eines Doktors der Naturwissenschaften (Dr. rer. nat.)  
genehmigte Abhandlung

Vorgelegt von  
**Vanya Todorova**  
aus Sofia  
Bulgarien

Hauptberichter: Prof. Dr. Dr. h.c. M. Jansen  
Mitberichter: Prof. Dr. T. Schleid  
Prüfungsvorsitzende: Prof. Dr. C. Stubenrauch

Tag der Einreichung der Arbeit: 08.11.2010  
Tag der mündliche Prüfung: 15.12.2010

Max-Planck-Institut für Festkörperforschung, Stuttgart  
2010



# Contents

<b>1. Zusammenfassung</b>	<b>5</b>
<b>2. Abstract</b>	<b>7</b>
<b>3. General part</b>	<b>9</b>
<b>3.1. Synthesis methods</b>	<b>9</b>
3.1.1. Solid state reaction	9
3.1.2. Metathesis reaction	10
3.1.3. High oxygen pressure autoclave	10
3.1.4. Hydrothermal synthesis	14
3.1.5. Electro crystallization from molten salts	15
<b>3.2. Characterization methods</b>	<b>17</b>
3.2.1. Introductory comments	17
3.2.2. X-Ray diffraction	17
3.2.2.1. The powder diffraction	18
3.2.2.2. Single crystal X-ray diffraction	21
3.2.3. Electron microscopy, Energy dispersive X-ray spectroscopy	23
3.2.3.1. Transmission Electron Microscopy	24
3.2.3.2. Scanning Electron Microscopy	24
3.2.3.3. Energy Dispersive X-ray spectroscopy	25
3.2.4. Inductively coupled plasma with optical emission spectrometry	25
3.2.5. Thermal methods of analysis TG, DTA, DSC	26
3.2.6. Electrical and ionic conductivity measurements	27
3.2.7. Seebeck coefficient measurements (Thermoelectric power)	29
3.2.8. Magnetic measurements	31
<b>4. Special part</b>	<b>33</b>
<b>4.1. Ternary and quaternary silver oxides – literature overview and motivation</b>	<b>33</b>
4.1.1. Systems Rh – O and Li – Rh – O	37
4.1.1.1. Synthesis of RhO <sub>2</sub> and Li <sub>2</sub> RhO <sub>3</sub>	37
4.1.1.2. Structural characterization of RhO <sub>2</sub> and Li <sub>2</sub> RhO <sub>3</sub>	39
4.1.1.3. Physical characterization of RhO <sub>2</sub> and Li <sub>2</sub> RhO <sub>3</sub>	45

4.1.2. System Ag – Co – O	56
4.1.2.1. Synthesis of AgCoO <sub>2</sub>	56
4.1.2.2. Structural characterization of AgCoO <sub>2</sub>	57
4.1.2.3. Physical characterization of AgCoO <sub>2</sub>	59
4.1.3. Systems Ag – Rh – O and Ag – Li – Rh – O	62
4.1.3.1. Synthesis of AgRhO <sub>2</sub> and Ag(Li <sub>1/3</sub> Rh <sub>2/3</sub> )O <sub>2</sub>	62
4.1.3.2. Structural characterization of AgRhO <sub>2</sub> and Ag(Li <sub>1/3</sub> Rh <sub>2/3</sub> )O <sub>2</sub>	63
4.1.3.3. Physical characterization of AgRhO <sub>2</sub> and Ag(Li <sub>1/3</sub> Rh <sub>2/3</sub> )O <sub>2</sub>	77
4.1.4. System Ag – Ir – O and Ag – Li – Ir – O	85
4.1.4.1. Synthesis of Ag(Li <sub>1/3</sub> Ir <sub>2/3</sub> )O <sub>2</sub>	87
4.1.4.2. Structural characterization of Ag(Li <sub>1/3</sub> Ir <sub>2/3</sub> )O <sub>2</sub>	87
4.1.4.3. Physical characterization of Ag(Li <sub>1/3</sub> Ir <sub>2/3</sub> )O <sub>2</sub>	92
4.1.5. Concluding remarks	96
<b>4.2. Cesium doped barium bismuthate – literature overview and motivation</b>	<b>97</b>
4.2.1. Synthesis of Cs <sub>x</sub> Ba <sub>1-x</sub> BiO <sub>3</sub>	102
4.2.2. Structural characterization of Cs <sub>x</sub> Ba <sub>1-x</sub> BiO <sub>3</sub>	105
4.2.3. Physical characterization of Cs <sub>x</sub> Ba <sub>1-x</sub> BiO <sub>3</sub>	110
4.2.4. Concluding remarks	115
<b>5. References</b>	<b>116</b>
<b>6. Appendix</b>	<b>129</b>
<b>6.1. Acknowledgements</b>	<b>137</b>
<b>6.2. List of Publication</b>	<b>139</b>
<b>6.3. Curriculum Vitae</b>	<b>140</b>

## 1. Zusammenfassung

Die vorliegende Arbeit ist in zwei Teile gegliedert. Es werden Techniken und Charakterisierungsmethoden der Festkörper- und Elektrochemie eingesetzt.

Im ersten Teil wird die Synthese und Untersuchung neuer ternärer und quaternärer Silber- und Lithiumoxide mit Schichtstruktur beschrieben. Es wurde versucht, das bekannte  $\text{AgCoO}_2$  um die Reihe  $\text{AgRhO}_2$  und  $\text{AgIrO}_2$  zu vervollständigen, die alle zu der Familie der Delafossite  $\text{AMO}_2$  gehören. Grundsätzlich kann jedes dreiwertige Kation  $M^{3+}$ , das mit Sauerstoff eine oktaedrische Koordination eingeht, in die reguläre ternäre Delafossitstruktur eingebaut werden.

- Im Falle von  $\text{AgCoO}_2$  wurde die Syntheseroute vereinfacht.
- Es wurde  $\text{AgRhO}_2$  dargestellt und dessen Struktur mittels Rietveld-Verfeinerung bestimmt.
- Die Darstellung von  $\text{AgIrO}_2$  wurde über verschiedene Synthesestrategien versucht. Trotz der bevorzugten Oxidationsstufe von +III für Iridium konnte überraschenderweise kein  $\text{AgIrO}_2$  mit Delafossitstruktur erhalten werden.

Es wurde jedoch eine quaternäre Delafossitvariante,  $\text{AgLi}_{1/3}\text{Ir}_{2/3}\text{O}_2$ , unter den milden Synthesebedingungen des Ionenaustausches dargestellt. Die Reaktion wurde mit  $\text{Li}_2\text{IrO}_3$  in  $\text{AgNO}_3/\text{KNO}_3$ -Schmelze durchgeführt, und es wurde ein entsprechender Austausch der einwertigen Ionen erreicht. Allerdings wurden nur 3/4 der Lithiumionen gegen Silber ausgetauscht, und Iridium bleibt weiterhin vierwertig. Da die Röntgenpulveraufnahme dieser Verbindung einige Besonderheiten aufwies, wurden HRTEM-Aufnahmen angefertigt. Diese wurden von DIFFAX-Simulationen unterstützt.

Im Ergebnis konnte gezeigt werden, dass die Struktur eine ausgeprägte Stapelfehlordnung aufweist. Diese kann unmittelbar auf die topochemische Synthese ausgehend von dem Kochsalz - Variante  $\text{Li}_2\text{IrO}_3$  zurückgeführt werden.

Zusätzlich wurde die Synthese des neuen quaternären Delafossits  $\text{AgLi}_{1/3}\text{Rh}_{2/3}\text{O}_2$  zur Bestätigung dieser neuen Struktur herangezogen. Hierbei werden zu dem die Ähnlichkeiten mit  $\text{AgRhO}_2$  ausgenutzt. Als Ausgangsmaterial für diesen quaternären Delafossit wurde die neue Verbindung  $\text{Li}_2\text{RhO}_3$  dargestellt und untersucht, die ebenfalls eine Schichtstruktur aufweist. Lithiumrhodiumoxid kristallisiert in der monoklinen Raumgruppe  $C2/m$ , wobei die Struktur als Kochsalz - Ordnungsvariante beschrieben werden kann, in dem die Sauerstoffatome eine kubisch dichteste Packung bilden und die Oktaederzwichenschichten entweder Rh oder  $\text{LiRh}_2$  enthalten. Das Silberrhodiumoxid,  $\text{AgLi}_{1/3}\text{Rh}_{2/3}\text{O}_2$  und  $\text{AgLi}_{1/3}\text{Ir}_{2/3}\text{O}_2$

weisen eine gemittelte Struktur auf, die weitgehend der trigonalen Delafossitstruktur in  $R\bar{3}m$  entspricht.

Diese Familie ternärer Oxide bietet reizvolle Beispiele von Ladungs-, Spin- und Orbitalordnung auf trigonalen Gittern und hat im Zusammenhang mit der Suche nach überlegenen thermoelektrischen oder (photo)katalytischen Materialien neuerdings erhebliches Interesse hervorgerufen.

Der zweite Teil der Arbeit wurde der Darstellung von Cäsiumdotiertem  $\text{BaBiO}_3$  gewidmet. In der Kristallstrukturen  $\text{BaBiO}_3$  wird die Verkipfung der  $\text{BiO}_6$ -Oktaeder von unterschiedlichen Bi-O-Bindungslängen verursacht. Werden die Ba- oder Bi-Plätze dotiert, so vermindert sich dieser Effekt. Außerdem weisen  $\text{Ba}_{1-x}\text{A}_x\text{BiO}_3$  ( $A = \text{K}, \text{Rb}$ ) und  $\text{BaPb}_{1-x}\text{Bi}_x\text{O}_3$  Supraleitfähigkeit mit einer der höchsten  $T_c$ -Werten unter den Nicht-Übergangsmetall-Supraleitern auf, wodurch sie zusätzliches Interesse auf sich gezogen haben. Im Gegensatz zu den Cuprat-Supraleitern mit zweidimensionalen  $\text{CuO}_2$ -Schichten zeigen diese Verbindungen Supraleitfähigkeit in der kubischen Phase. Dies lässt vermuten, dass die Zweidimensionalität keine notwendige Bedingung für Hochtemperatursupraleitung ist. Zusätzlich besitzen die Kaliumdotierten Bariumbismutate keinerlei magnetische Ordnung und widersprechen somit ebenfalls den Cupraten. Von der Synthese von Cäsiumdotiertem Bariumbismutat erhoffte man Ansätze zur Klärung offener Fragen zu den physikalischen Eigenschaften in diesen Systemen. Vor allem der Vergleich der Ionenradien von  $\text{Cs}^+$  und  $\text{K}^+$  könnte die Verkipfung der  $\text{BiO}_6$ -Oktaeder besser erklären, zusätzlich sollte man ein höheres  $T_c$  erwarten.

Das Ziel der Arbeit ist die Aufklärung des Zusammenhangs zwischen dem Anteil des intercalierten Cäsiums und der Zellparameter sowie die Dotierungsgrenzen, innerhalb derer die Verbindung Supraleitfähigkeit aufweist. Die höchste Dotierung mit Cäsium war  $\text{Cs}_{0.27}\text{Ba}_{0.63}\text{BiO}_3$ . Leider zeigten jedoch die  $\text{Cs}^+$ -dotierten Bariumbismutate keine supraleitenden Eigenschaften.

## 2. Abstract

The presented dissertation combines synthesis and characterization techniques of solid state chemistry and electrochemistry. The work is organized into two main parts.

The first part deals with the synthesis, structural characterization and investigation of the physical properties of new ternary and quaternary transition metal oxides with layered structures. Several compounds of delafossite structure  $ABO_2$  with silver on A position and different trivalent cation capable of adopting an octahedral coordination were synthesised previously. From the group 9 (Co, Rh, Ir) of the periodic table, only  $AgCoO_2$  had been known. The target of this thesis was the synthesis and characterization of  $AgRhO_2$  and  $AgIrO_2$ . Furthermore, a more simplified synthesis method for  $AgCoO_2$  was developed.

$AgRhO_2$  was successfully synthesized and its crystal structure characterized by Rietveld analysis.

Different synthesis approaches were applied to prepare  $AgIrO_2$ , but the delafossite structure has not been observed, although the valence state of 3+ is known to be one of the most common for iridium.

Instead, a new, delafossite type compound incorporating Ir (4+) has been found employing the method of a mild ion-exchange reaction. Treating  $Li_2IrO_3$  with molten  $AgNO_3/KNO_3$ , an exchange reaction of the monovalent cations was observed. However, only  $\frac{3}{4}$  of the lithium ions were substituted for silver, and iridium stayed in the oxidation state of 4+. The final product of composition  $AgLi_{1/3}Ir_{2/3}O_2$  represents a quaternary variant of the delafossite structure. Because the powder pattern of that compound exhibited *Warren peaks*, indicative of potential disorder phenomena, a closer investigation by HRTEM and DIFFAX simulations was conducted. The stacking fault was conclusively rationalized by elucidating the formation mechanism of the quaternary delafossite structure from the respective rock salt type variants of  $Li_2MO_3$ .

Additionally, the  $AgLi_{1/3}Rh_{2/3}O_2$  was synthesized. Also the starting material for this quaternary delafossite,  $Li_2RhO_3$ , another layered new compound was synthesized and characterized.  $Li_2RhO_3$  crystallizes in the monoclinic space group  $C2/m$ . The structure can be derived from the rock salt structure with a close packing of the oxygen atoms and alternating layers of Rh and  $Li_{1/3}Rh_{2/3}$ . Upon ion exchange with silver, a structural transition to the delafossite type in the trigonal space group  $R\bar{3}m$  has been observed.

This family of ternary oxides provides interesting examples of charge, spin, and orbital ordering in trigonal lattices and has recently attracted significant interest in the context of the search for superior thermoelectric or (photo)catalytic materials.

The second part of the work has been devoted to the synthesis of Cs-doped BaBiO<sub>3</sub>. In BaBiO<sub>3</sub>, the tilt of the octahedra BiO<sub>6</sub> is caused by the difference in the two Bi–O bond length, which disappears upon doping either the Ba or the Bi sites. Furthermore, Ba<sub>1-x</sub>A<sub>x</sub>BiO<sub>3</sub>, A = K, Rb and BaPb<sub>1-x</sub>Bi<sub>x</sub>O<sub>3</sub> were found to be superconductors causing additional interest, with one of the highest transition temperatures  $T_c \sim 30$  K among non-transition-metal superconductors. Unlike the cuprate superconductors (two-dimensional CuO<sub>2</sub> planes), these compounds exhibit superconductivity in the cubic phase, which suggests that the two-dimensionality is not an essential condition for high-temperature superconductors. Furthermore, the barium bismuthate systems and the potassium doped derivatives do not show any magnetic ordering, in contrast to the cuprates. The investigation of cesium doped barium bismuthate was conducted in order to shed more light into the interplay of physical properties of these systems. In principle the intercalation of the larger Cs ions compared to K<sup>+</sup> could be more effective by throwing light on the BiO<sub>6</sub> octahedrons tilts; furthermore a higher  $T_c$  is expected.

The primary goal of this work was to investigate the stability and phase diagram of Cs<sub>x</sub>Ba<sub>1-x</sub>BiO<sub>3</sub> and study the dependence of the structural and electronic parameters as a function of the doping level. Up to 0.27 Cs were successfully doped on the Ba position. But, unfortunately, it turned out that these phases did not exhibit superconducting properties.



### 3. General part

#### 3.1. *Synthesis Methods*

In solid state chemistry, there exists a whole bunch of synthetic approaches used to prepare the materials of interest. Solids can also be fabricated in a variety of forms, as ceramics, films, powders, single crystals, nanoparticles, etc. In this chapter of the present doctoral thesis, only the methods used for the purpose of the work itself are shortly commented.

##### 3.1.1. Solid State Reactions

A solid state reaction is a type of reaction in which the reactants are mixed together and are supposed to react without any presence of a solvent. Because of that reason, there are some defined conditions which must be fulfilled, and some restrictions which need consideration. Normally, the temperature region in which the reactions take place is from 973 to above 1373 K, and in case of ceramics even above 2273 K. The appropriate temperature for each particular case is different and it should not reach the decomposition temperature of reactants, although it should be high enough generally constituting  $2/3$  of the melting temperature of one of the components. Another parameter is the reaction duration which usually extends from couple of hours to several days, the reason for that being the huge structural reorganization taking place - migration of the ions throughout the solid. Therefore, the diffusion is a crucial issue in solid state reactions, postulating: the better the contact between reagents the easier the diffusion. The realization of solid state reactions could be done in a muffle furnace in air or in a tube oven where the atmosphere can vary. The two types of ovens are presented in Figure 3.1.1.



**Figure 3.1.1** Left: muffle furnace; right: tube oven

### 3.1.2. Metathesis Reactions

Metathesis reactions are prevalingly kinetically controlled and, therefore, the diffusion in and trough the solids and the media is important. The classical ion exchange reaction in an aqueous solution is deeply studied<sup>1, 2</sup>. In solid state chemistry, the role of liquid media by the ion exchange reactions is maintained from molten fluxes mostly nitrates or other salts. It is important that the ionic radii of the exchanged species are approximately the same in order to avoid expansion or shrinking of the structure. According to a study,<sup>3</sup> the kinetics of ion exchange for a specific condition could be expressed with the equations 3.1.1 - 3.1.3

$$F = \frac{Q_t}{Q_\infty} \quad (3.1.1)$$

$$F = 1 - \frac{6}{\pi^2} \sum_{n=1}^{\infty} \frac{e^{-n^2 Bt}}{n^2} \quad (3.1.2)$$

$$B = \frac{\pi D^i}{r^2} \quad (3.1.3.)$$

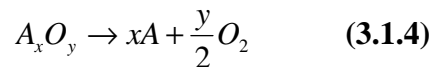
$F$  is an ion exchange rate,  $Q_t$  and  $Q_\infty$  is the amount of exchange after definite time,  $t$ , and infinite time, respectively.  $D^i$  is the effective diffusion coefficient of the two exchanging ions, and  $r$  is the ionic radius.

The excess of the exchange ion in the flux affects the diffusion in the solid state as a transfer rate. Smaller species and higher values of diffusion coefficients pander the ion exchange. For the aims of this doctoral thesis, this method has been used with lithium transition metal oxides aiming at obtaining silver transition metal oxides. The silver nitrate has been mixed with potassium nitrate to prevent the reduction to elementary silver,<sup>4, 5</sup> and according to Kleppa *et al.*,<sup>6</sup> to shift to the negative values of enthalpy stabilizing the mixture.

### 3.1.3. High Oxygen Pressure Autoclave

This method finds an application in case of unstable at atmospheric pressure and higher temperature starting oxides. The method is relatively simple: in a special steel body a defined amount of oxygen is condensed, which later upon increasing the temperature generates oxygen pressure compensating for the partial oxygen pressure of the oxides. From thermodynamic

point of view, if one considers the oxygen activity equal to its concentration and write the decomposition reaction, then:



The equilibrium constant for that reaction is:

$$K_p = \frac{p(A)^x * p(O_2)^{\frac{y}{2}}}{p(A_xO_y)} \quad (3.1.5)$$

Since the reaction is heterogeneous, the equilibrium constant is totally dependant on the oxygen partial pressure:

$$K_p = p(O_2)^{\frac{y}{2}} \quad (3.1.6)$$

Furthermore, the chemical thermodynamics relates the change in temperature to the change in the equilibrium constant for the given process providing the standard enthalpy change,  $\Delta H^\theta$  for a constant pressure and the total energy,  $\Delta U$ , for a constant volume. This equation was first derived by van't Hoff.

$$\frac{d \ln K}{dT} = \frac{\Delta U}{RT^2} \quad (3.1.7)$$

$$\ln K = \frac{\Delta U}{R} * \frac{1}{T} + c \quad (3.1.8)$$

One could integrate this equation, because U is approximately constant in relatively big temperature interval. The equilibrium pressure of oxygen over  $Ag_2O/Ag$  system is reported else where<sup>7</sup>. Figure 3.1.2 shows the partial oxygen pressure/temperature dependence for that system.

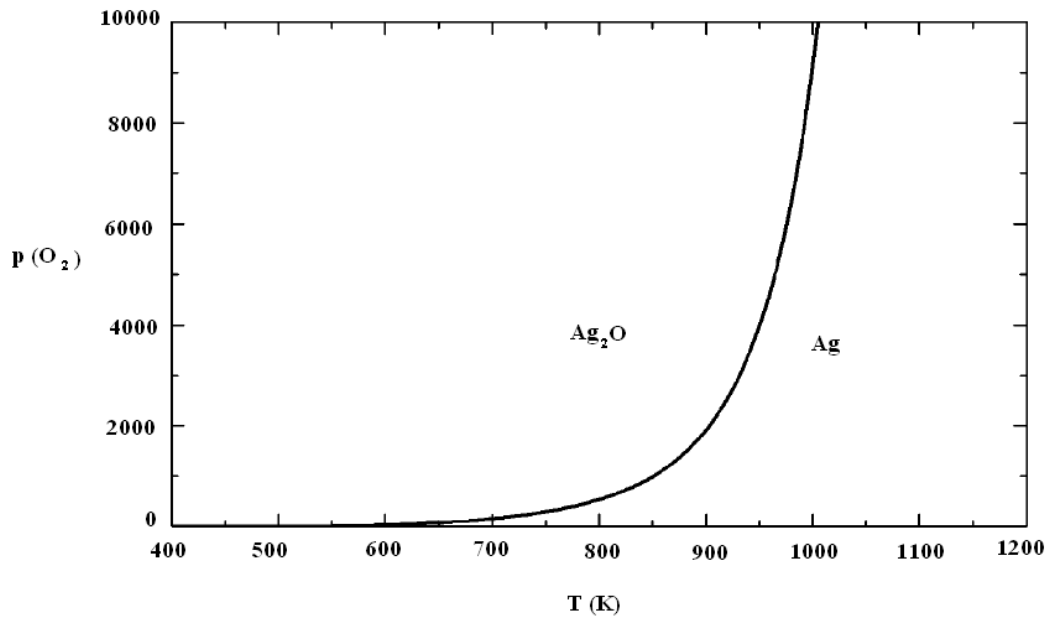


**Figure 3.1.2** Oxygen pressure/temperature dependence for  $\text{Ag}_2\text{O}/\text{Ag}$  system

The principle view of the autoclave is shown on Figure 3.1.3 and the pressure in it could be calculated in first approximation from the Van der Waals equation:

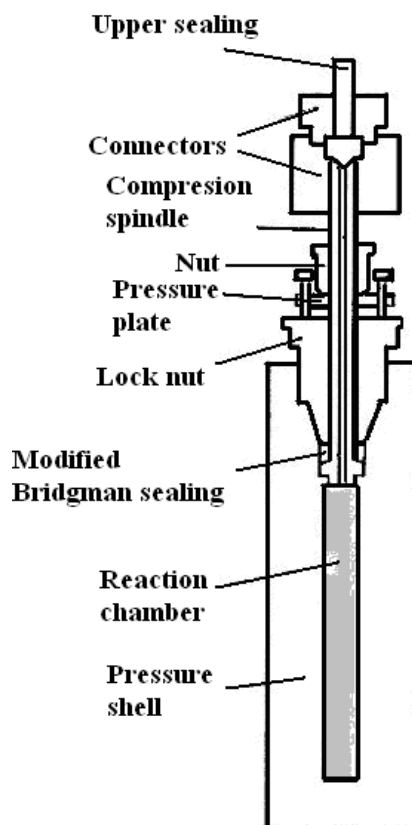
$$p = \frac{nRT}{V_{\text{eff}} - nb} - \frac{n^2 a}{V_{\text{eff}}^2} \quad (3.1.9)$$

Where:  $T$  is the temperature (K);  $p$  is pressure (Atm.);  $V_{\text{eff}}$  is the effective volume of autoclave (0,02 l);  $n$  – mol;  $R$  – universal gas constant (0,08206 atm.K<sup>-1</sup>.mol<sup>-1</sup>);  $a = 1,36$  atm.l<sup>2</sup>.mol<sup>-2</sup>;  $b = 0,03183$  l.mol<sup>-1</sup> ( $a$  and  $b$  are Van-der-Waals constants for oxygen<sup>8</sup>).

$$n_{\text{O}_2} = \frac{m}{M} = \frac{\rho * V}{M} \quad (3.1.10)$$

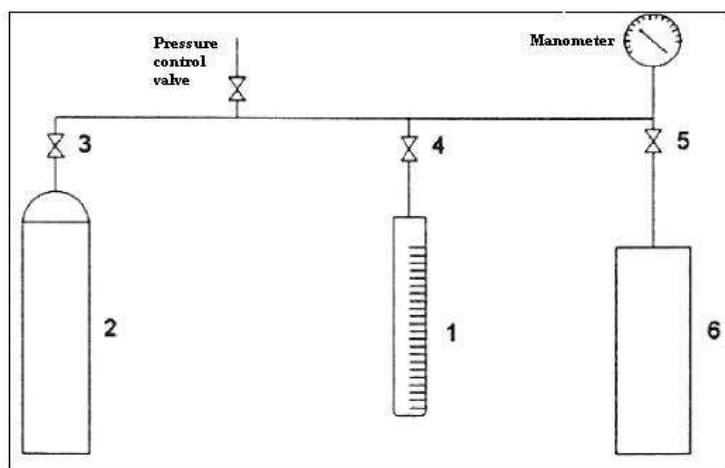
$\rho$  -oxygen density at 77 K (1,201g.cm<sup>-3</sup>);  $V$  – condensed oxygen volume (cm<sup>3</sup>);  $M$  – molar mass of oxygen (31,9988g.mol<sup>-1</sup>).

Figure 3.1.3 presents the schematic view of a high oxygen pressure autoclave.



**Figure 3.1.3** High oxygen pressure autoclave

In Figure 3.1.4 the scheme of filling equipment is shown. The autoclave is cooled in liquid nitrogen to 77 K and the pressure spindle 3 is connected to the filling equipment. When the oxygen bottle and the valves 3 and 4 are open the calculated amount of oxygen condenses in the autoclave. The charging of autoclave occurs when valve 3 is closed and valve 5 is open. Removing the cooling from the measuring cylinder lets the appropriate amount of oxygen condense in the autoclave. After separating the autoclave from the filling equipment it must be properly closed with the sealing.



**Figure 3.1.4** Filling equipment for the high oxygen pressure autoclave

### 3.1.4. Hydrothermal Synthesis

Rabenau *et al.*<sup>9</sup> define this kind of reaction as heterogeneous reaction in aqueous media above 100° C and 1 bar pressure. Under hydrothermal conditions, the reactants enter the solution as complexes and the conditions of chemical transport reactions are obtained. This method is appropriate for the synthesis of compounds of elements in hardly achievable oxidation states, metastable compounds and low-temperature phases. The principle is rather simple; the starting materials are mixed with water and heated at a temperature under the decomposition temperatures of the reagents. A necessary condition is that defined amount of compounds dissolve, so that sufficient diffusion occurs and the thermodynamically stable products build in certain reaction time. Normally metals, metal oxides and salts are used and their solubility could be influenced by adding complex ions. In temperature region over 373 K and pressure above 1 bar the physical properties of water change.<sup>10-13</sup> As far as it is a kind of transport reaction, the increase of temperature decreases the water viscosity which improves the ions mobility. The thermodynamic parameters of water at high temperature and pressure could be found in literature,<sup>12</sup> hence when the partial pressure over the solution is low the critical point of it is shifted to higher values. The reactions could be influenced by different mechanisms – tuning polarity and viscosity of the media, pH-variation, temperature, or reaction duration. The autoclaves used in this work are shown on Figure 3.1.5. The body and the closure cap are made of steel and inside a Teflon vessel covered with a Teflon closure cap with exactly the same size is placed. The volume is approximately 30 cm<sup>3</sup>. The advantage of the Teflon is its corrosion resistivity, but as a disadvantage could be mention the relatively lower temperature region –

below 240°C. After adjusting the exact stoichiometry of the reactants, they are introduced into the Teflon vessel; the water is added with or without mineralizer and the vessel is closed with the closure cap. The Teflon part is placed in the steel body and it is tightened with the steel closure cap. The autoclave is placed in a dryer in the temperature region 140-220°C, whereas the reaction time could vary from some hours to couple of days.



**Figure 3.1.5** The view of the hydrothermal autoclaves used in this work.

### 3.1.5. Electrocrystallization from Molten Salts

The electrolysis is a process in which non-spontaneous chemical reactions are driven from direct electrical current. The first electrolysis was performed on water obtaining hydrogen and oxygen. After that potassium, sodium and some other elements were discovered by Sir Davy using the electrolysis approach. To be performed, there are three important components, namely: supply of energy necessary for the chemical reaction – a DC source; free ions as electrical current carriers – electrolyte; an electrical conductor which provides the physical interface between the electrical circuit providing the energy and the electrolyte – electrodes.

Faraday postulated the two laws of electrolysis, which are:

- **First law:** The quantity of elements separated by passing an electrical current through a molten or dissolved salt is proportional to the quantity of electric charge passed through the circuit.
- **Second law:** The mass of the resulting separated elements is directly proportional to the atomic masses of the elements when an appropriate integral divisor is applied. This

provides strong evidence that discrete particles of matter exist as parts of the atoms of elements.

The principle arrangement of the equipment used for the purposes of this work is shown in Figure 3.1.6.

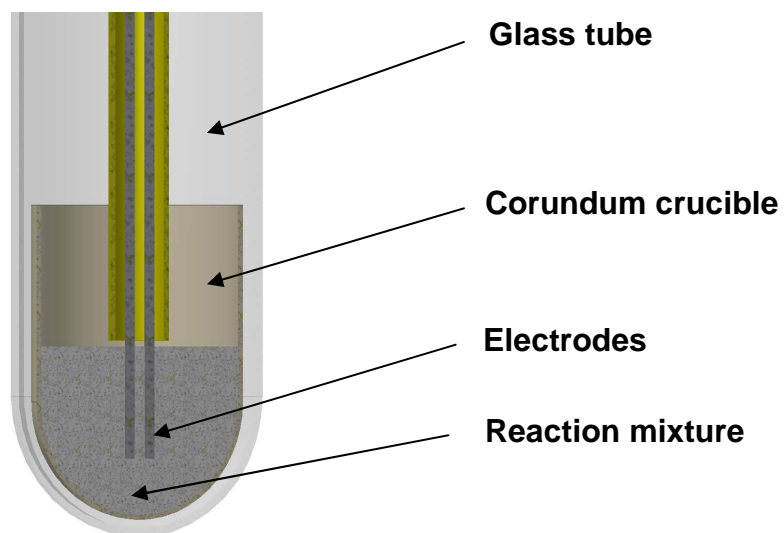


**Figure 3.1.6** Schematic representation of the electrocrystallization equipment



## **3.2. Characterization Methods**

### **3.2.1. Introductory Comments**

In the inorganic structural chemistry, two distinctively different types of solids are generally encountered provided their three dimensional architecture displays a certain order. To the first category one can attribute the so called molecular crystals, materials the crystal structure of which is defined by the specific packing of discrete molecular units. The second class of matter encompasses the extended solids, crystalline materials whose constitution develops throughout the physical dimensions of the individual crystallites. For molecular crystals, it usually suffices to determine the molecular constitution and geometry, and only rarely further investigation concerning the packing of these “building blocks” is carried out. However, in the case of extended solids the situation is completely different. Here, contrary to the “ideal”, defect-free molecular crystals, different types of defects and impurities are unavoidable. The effect of this gives rise to non-stoichiometry, i.e. variable composition, and induces dramatic differences in properties. Therefore, besides the determination of the average crystal structure, special attention should be paid to local structure. On a larger length scale, the properties of non-molecular solids depend also on the size and shape of individual crystallites, i.e. on their microstructure. Since the structural determination is concerned at several levels, a vast range of techniques is needed to characterize these solids. There are three main categories of physical techniques which are used for that purpose: diffraction, microscopic and spectroscopic analyses. In addition, other techniques such as thermal analysis and physical properties measurements provide valuable information in certain cases.

### **3.2.2. X-ray Diffraction**

X-ray diffraction is the principle technique in solid state chemistry and is used in two main areas, for “fingerprint” characterization of crystalline materials and for determination of their structure. The method is based on the interaction between incident X-rays with the atoms from the crystal lattice. The result of this interaction is that part of the beam is transmitted, part is absorbed by the sample, part is refracted and scattered (destructive interference), and part is diffracted (constructive interference). According to a theory developed by the British physicist Sir William Lawrence Bragg – since then known as the Bragg’s law – that the atoms in the

crystals repeat in a defined manner forming planes such that each acts as a semitransparent mirror (Figure 3.2.1), the following quantitative relation (3.2.1) can be expressed:

$$2d \sin \theta = n\lambda \quad (3.2.1)$$

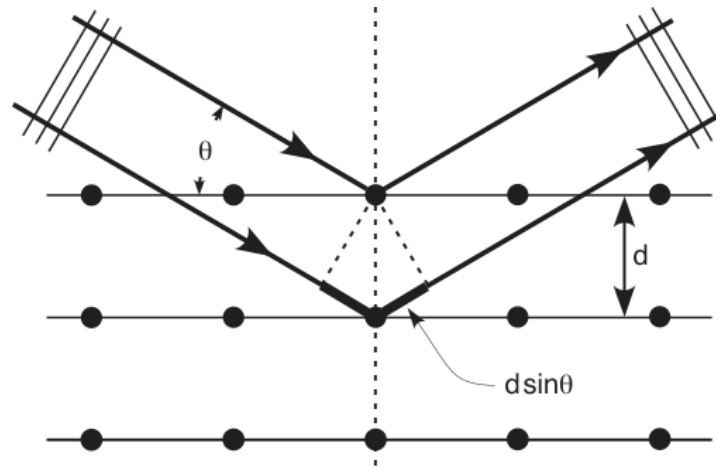


**Figure 3.2.1** Derivation of Bragg's Law

In Bragg's equation, **d** is the distance between adjacent planes of atoms, **θ** is the angle of incident X-ray beam, **n** is an integer (order of diffracted beam) and **λ** is the beam wavelength. When Bragg's law is satisfied, the reflected beams are in phase and interfere constructively. At angles of incidence other than the Bragg's angle, reflected beams are out of phase and destructive interference (cancelations) occurs. In real crystals where thousands of planes exist, Bragg's law imposes a stringent condition on the angles at which reflections may occur. Therefore, the characteristic set of d-spacings generated in a typical X-ray scan provides a unique "fingerprint" of the solid. Although the model suggested by Bragg is an oversimplification of the real processes taking place when X-rays interact with crystalline matter, it provides accurate solutions in crystallography and is widely accepted.

### 3.2.2.1. The Powder Method

The general principle of the powder diffraction method is depicted in Figure 3.2.2. Generally, in modern powder diffraction equipments a monochromatic source of radiation, most commonly Cu K<sub>α</sub> radiation, is used. The sample is in the form of fine powder consisting of crystals oriented in every possible direction so that the various lattice plains are also present in every possible orientation. Therefore, for each set of planes there are crystals oriented at the Bragg angle to the incident X-ray beam. The diffracted beams are usually detected by a

movable detector (scintillation counter) directly connected to a computer equipped with a compatible software.

There are two major factors which determine a powder pattern. The first one encompasses the size and symmetry of the unit cell, whereas the second takes into consideration the atomic number and specific positions of atoms within this unit cell. Therefore, a powder pattern has two characteristic features; the d-spacings of diffraction peaks, and their intensities. From the two, intensities are usually more difficult to measure accurately and therefore to compare, whereas d-spacings are more useful for phase identification analysis. In many cases using only d-spacings for qualification is enough, especially for materials with lower symmetry since the unit cell variables increase in number with decreasing the space group symmetry, making it almost impossible for two different materials to display the same powder pattern. However, for compounds possessing higher symmetry, especially cubic where only one variable exists, the likelihood of two phases to generate the same powder pattern increases substantially. In such cases the necessity to take into consideration the individual peak intensities is obvious.

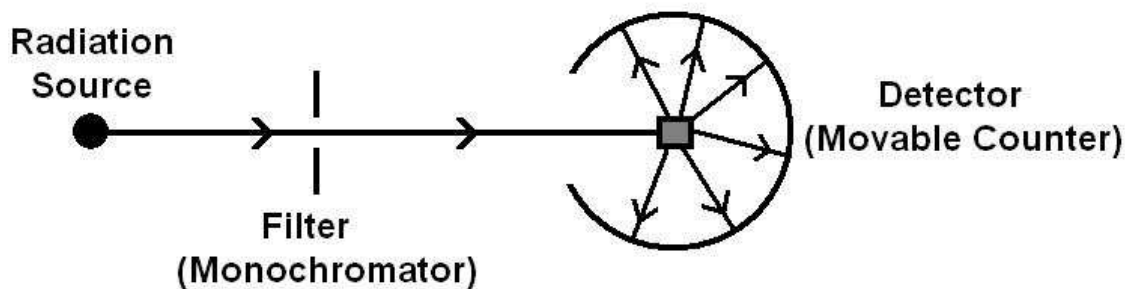


**Figure 3.2.2** Principle of the powder method

For the aims of this doctoral thesis, the equipments described in the following few lines have been used. Figure 3.2.3 shows two machines STADI-P from the Stoe&Cie (Darmstadt), both with germanium (111) monochromator and Cu  $K\alpha_1$  ( $\lambda=1,540598 \text{ \AA}$ ) radiation. The difference between these two machines is the detector: on the right hand site is shown the PSD1 (Position Sensitive Detector) with angular range of  $35^\circ$  and resolution of  $\Delta 2\theta = 0,15$ ; on the left hand site one can see the linear PSD 2 detector with angular range of  $6^\circ$  and resolution of  $\Delta 2\theta = 0,08$ , combined with IP-PSD (Image Plate Position Sensitive Detector) for angular range of  $140^\circ$  and resolution of  $\Delta 2\theta = 0,1$ . There are different measurements modes for air- and/or moisture sensitive samples: a capillary (Debye-Scherrer) and a flat transmission mode.



**Figure 3.2.3** Two STADI-P X-Ray diffractometers (Stoe&Cie, Darmstadt)

Aiming at a higher resolution and higher quality of the data, two more precise diffractometers have been used: the D8-Advance from Bruker AXS. In Figure 3.2.4, on the left hand side the flat- and on the right hand side the capillary mode are represented. The advantage of the flat mode is that up to nine samples could be loaded and measured without wasting operation time; a disadvantage is that it is not appropriate for unstable samples and the measurements should be performed at room temperature. The advantage of the capillary mode diffractometer is that it could perform cooling and heating measurements. The Bruker machines are with Ge (111) - Johanson monochromators, and differ in X-Ray source; they possess Cu  $K\alpha_1$  ( $\lambda=1,540598 \text{ \AA}$ ) as well as Mo  $K\alpha_1$  ( $\lambda=0,70930 \text{ \AA}$ ) radiation sources. The  $2\theta$  step width is from 0,01 to 0,008. The STADI-P diffractometers are used for phase analysis where a diffractogram generated is being compared either to an existing one from the database (available PDF data), or alternatively to a theoretically calculated one. The limit of detection is around 5 %. The Bruker machines have been used for structural determination combining the high quality of the diffractograms obtained with appropriate software (TOPAS) for structural solution.

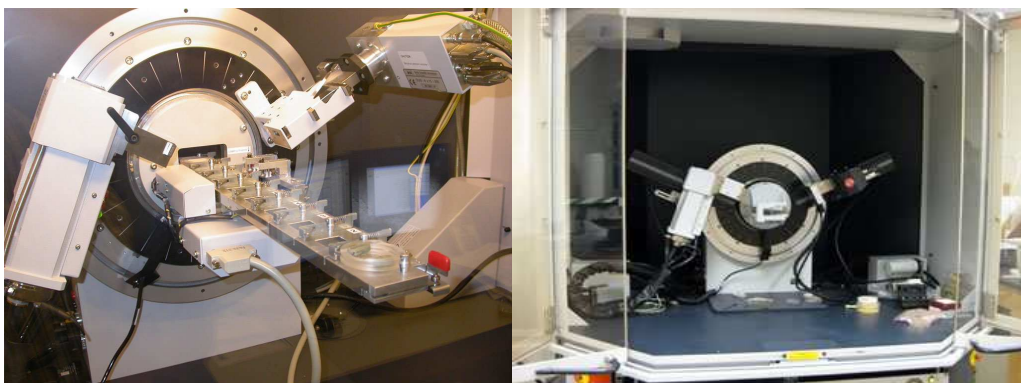


**Figure 3.2.4** Two Bruker X-Ray diffractometers (Bruker, Karlsruhe)

### 3.2.2.2. Single Crystal X-ray Diffraction

Usually, crystal structures contain from several hundred to several thousand unique reflections, the spatial arrangement of which is referred to as a diffraction pattern. Indices (hkl) may be assigned to each reflection, indicating its position within the diffraction pattern. This pattern has a reciprocal Fourier transform relationship to the crystal lattice and the unit cell in real space. This step is referred to as the solution of the crystal structure. After the structure is solved, it is further refined using the least-squares techniques.

Molybdenum is the most common radiation source for single crystal diffraction, with  $\text{Mo}_{K\alpha}$  radiation =  $0.7107\text{\AA}$ . These X-rays are collimated and directed onto the sample. When the geometry of the incident X-rays impinging the sample satisfies the Bragg's Law, constructive interference occurs. Figure 3.2.5 represents schematically the set-up of a single crystal X-ray diffractometer. That is a three axis system comprising of fixed-chi stage (chi angle  $\sim 54.74^\circ$ ) and phi drive with  $360^\circ$  rotation. The X-rays which are not diffracted are either transmitted through the crystal or reflected off the crystal surface. A beam stop is located directly opposite the incident beam to block transmitted rays and prevent burn-out of the detector. Reflected rays are not picked up by the detector due to the different angles involved. Diffracted rays at the correct orientation are then collected by the detector.

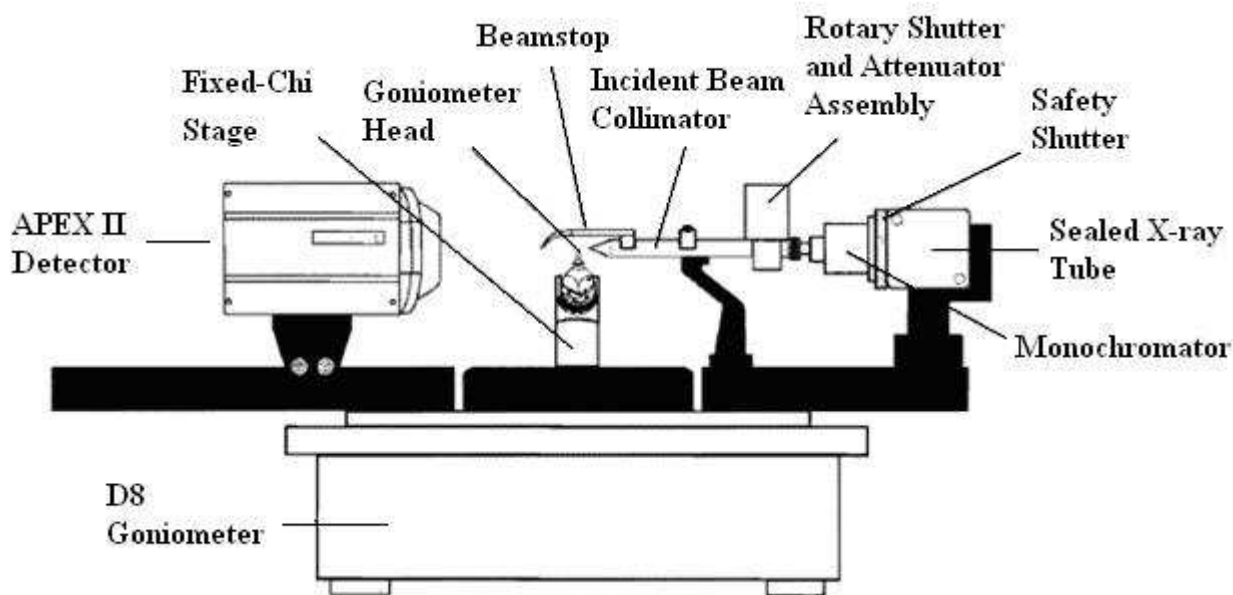


Figure 3.2.5 Schematic representation of a single crystal X-ray diffractometer

Once the crystal is mounted and centered, a preliminary rotational image is collected to screen the sample quality and to select parameters for later steps. An automatic collection routine can then be used to collect a preliminary set of frames for determination of the unit cell. Reflections from these frames are auto-indexed to select the reduced primitive cell and calculate the orientation matrix which relates the unit cell to the actual crystal position within the beam. The primitive unit cell is refined using least squares and then converted to the appropriate crystal system and Bravais lattice. This new cell is also refined using least squares to determine the final orientation matrix for the sample. After the refined cell and orientation matrix have been determined, intensity data is collected. Generally this is done by collecting a sphere or hemisphere of data using an incremental scan method, collecting frames in  $0.1^\circ$  to  $0.3^\circ$  increments (over certain angles while others are held constant). Data is typically collected between  $4^\circ$  and  $60^\circ$   $2\theta$  for molybdenum radiation. A complete data collection may require anywhere between 6 – 24 hours, depending on the specimen and the diffractometer. Exposure times of 10 – 30 seconds per frame for a hemisphere of data will require total run time of 6 – 13 hours.

The equipment used in this work for collecting the single crystal data are Smart APEX I diffractometer (Bruker AXS, Karlsruhe, Germany, Mo-  $K_\alpha$  radiation,  $\lambda = 0.7107\text{\AA}$ ) and a dual wavelength three circle single crystal diffractometer Smart APEX II (Bruker AXS, Karlsruhe, Germany) equipped with a CCD – detector, a Siemens X – ray scaled tube (Mo-  $K_\alpha$  radiation,  $\lambda = 0.7107\text{\AA}$ ), an Incoatec (Geesthacht; Germany), microfocus X – ray source I $\mu$ S (Cu-  $K_\alpha$  radiation,  $\lambda = 1.54178\text{\AA}$ ).

After the data have been collected, corrections for instrumental factors, polarization effects, X-ray absorption and (potentially) crystal decomposition must be applied to the entire data set. This integration process also reduces the raw frame data to a smaller set of individual integrated intensities. The reduction of the data is done either with SAINT<sup>14</sup> or X-RED<sup>15</sup>, and absorption correction is performed with the program SADABS<sup>16</sup> or X-SHAPE.<sup>17</sup> When the final data set have been produced, the phase problem must be solved to find the unique set of phases that can be combined with the structure factors to determine the electron density and, therefore, the crystal structure. A number of different procedures exist for solving the phase problem, but the most common method is the least squares. Solution of the phase problem leads to the initial electron density map. Elements can be assigned to intensity centers, with heavier elements associated with higher intensities. Distances and angles between intensity

centers can also be used for atom assignment based on likely coordination. If the sample is of a known material, a template may be used for the initial solution. Once the initial crystal structure is solved, various steps can be done to attain the best possible fit between the observed and calculated crystal structure. The final structure solution will be presented with an R value, which gives the percent variation between the calculated and observed structures.

### 3.2.3. Electron Microscopy, Energy Dispersive X-ray Spectroscopy

Electron microscopies provide a tremendously wide range of resolution covering the region from the micrometer level down to the atomic scale. This is achieved by exposing the specimen under consideration to an electron beam and exploiting the various phenomena which take place as a direct consequence of electron-matter interaction (Figure 3.2.6).

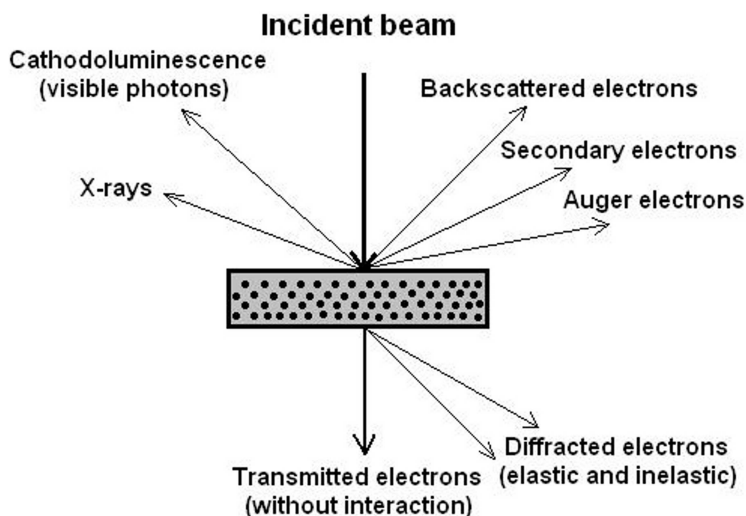


**Figure 3.2.6** An illustration of different types of interactions and consequent phenomena between electron beam and matter

Electron microscopes operate either in reflection or transmission modes. For transmission, samples should be thinner than 200 nm because matter adsorbs electrons strongly. In reflection mode sample thickness is not a matter of debate, since the image is formed by secondary and backscattered electrons.

### 3.2.3.1 Transmission Electron Microscopy

A schematic representation of the transmission electron microscope (TEM) is shown in Figure 3.2.7. The objective lens (an electromagnetic lens) forms a 2D diffraction pattern in the back focal plane with electrons scattered by the sample, and combines them to generate an image in the image plane (1. intermediate image). Therefore, diffraction pattern and image are simultaneously present in TEM. It depends on the intermediate lens which of them appears in the plane of the second intermediate image. Switching from real space (image) to reciprocal space (diffraction pattern) is easily achieved by changing the strength of the intermediate lens. In imaging mode, an objective aperture can be inserted in the back focal plane to select one or more beams that contribute to the final image, namely: bright field (BF), dark field (DF), or high resolution TEM (HR-TEM). For selected area electron diffraction (SAED), an aperture in the plane of the first intermediate image defines the region of which the diffraction is obtained.

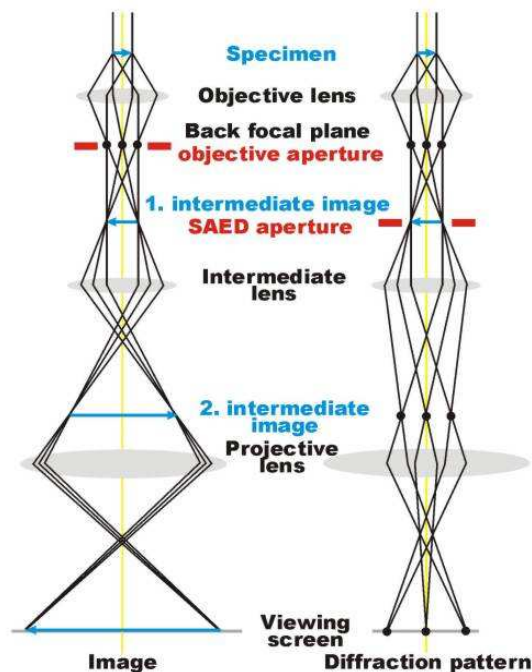


Figure 3.2.7 Schematic diagram of the working principle in TEM

### 3.2.3.2 Scanning Electron Microscopy

In scanning electron microscopy (SEM), the image is obtained by scanning a finely focused electron probe in a raster pattern over the sample surface in synchrony with writing the detector signals. Strong detector responses result in high brightness in the image. Magnification is determined by the ratio of the area scanned to the display area. One imaging mode makes use



of the secondary electrons emitted by the sample surface upon excitation from the incident electron beam. These secondary electrons are low in energy, making it very easy to collect them by an appropriately biased scintillator. The number of electrons emitted depends on the angle of the specimen surface with respect to the electron beam and the detector. The resultant differences in brightness, therefore, reveal the surface topography. Another imaging mode within a SEM makes use of backscattered electrons. These electrons possess much higher energies comparable to those of the incident beam electrons (1-30 keV). Therefore, the signal intensity is less sensitive to surface topography (higher penetration depth of the incident beam) but instead depends on the chemical composition of the specimen. This imaging mode is capable of providing excellent atomic number contrast.

The machine used for the purpose of this work is SEM – XL 30 TMP, Philips Electron Optics (Eindhoven, the Netherlands) with tungsten cathode, and acceleration potential of 30 keV.

### **3.2.3.3 Energy Dispersive X-ray Spectroscopy**

Energy dispersive X-ray spectroscopy (EDS or EDX) is the most commonly used analytical technique in an electron microscope. Electron excitations caused by the high voltages usually used in microscopes lead to ionization within the sample. The consequent relaxation in energy results in emission of X-rays that can be analyzed by a solid-state energy-dispersive detector. Qualitative analysis by this method is straightforward since each element has a unique pattern of X-ray lines from the K, L, and M shells. EDS method can provide, however, only semi-quantitative analysis.

For the aims of this doctoral thesis, the EDS supplied with the SEM (described in chapter 3.2.3.2) is used. The system specifications are: EDAX (Traunstein-Neuhof) with S-UTW-Si (Li)-Detector (Super Ultra Thin Window).

### **3.2.4 Inductively Coupled Plasma with Optical Emission Spectroscopy**

Inductively coupled plasma with optical emission spectroscopy (ICP-OES) is a method for elemental analysis. A high-frequency current (typically 27 or 41 MHz) is sent through a coil, generating a magnetic field. Plasma is then formed from the gas (argon) flowing through the coil. In the plasma, the same number of Ar<sup>+</sup> and electrons coexist, maintaining the charge balance. The argon plasma reaches a temperature of 6000 to 8000K. When the sample, in the

form of fine aerosol, is introduced into the plasma via a carrier gas, nearly all of the elements in the sample become highly excited by the energy from the plasma and begin emitting light. Each element emits light with a wave length (spectrum) specific to that element (usually in the range 165 – 800 nm). It is, therefore, possible to analyze and identify the elements in the test sample by separating the emitted light into its spectral components using a high-performance spectrometer. The emission intensity for each element is monitored for each standard solution and a calibration curve of emission intensity versus element concentration can be constructed. A schematic representation of an ICP chamber can be seen in Figure 3.2.8. The analyses in this work are performed with the help of Vista-Pro (Simultaneous ICP-OES, CCD detector, with axial plasma, Varian). The digestion of the samples is performed using a Berghof-Pressure-System with PTFE coating.

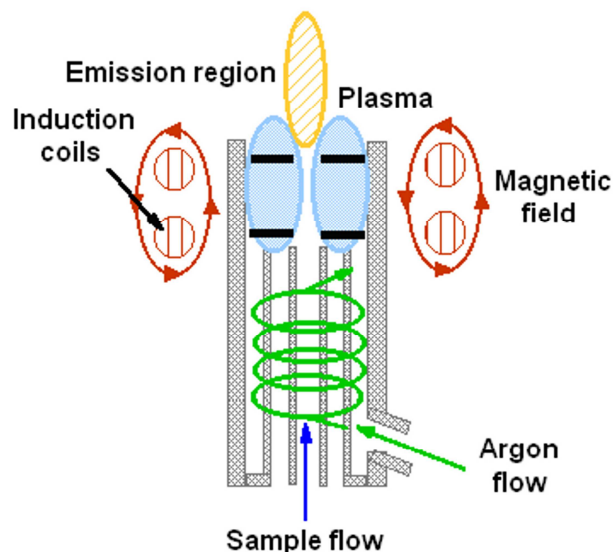


**Figure 3.2.8** Schematic representation of the ICP chamber

### 3.2.5 Thermal Methods of Analysis

Thermal analysis refers to a group of techniques in which a physical property (e.g. enthalpy, heat capacity, mass etc.) of a sample is monitored against time or temperature while the temperature of the sample, in a specified atmosphere, is programmed. The principle techniques of thermal analysis are thermogravimetry (TG), differential thermal analysis (DTA) and differential scanning calorimetry (DSC).

TG monitors the sample change in mass as a function of time or temperature. The sample is usually heated at constant rate and the percentage change in mass is plotted against temperature ramp. This method can be used for monitoring and quantification of compositional changes.

Many variables such as particle size or the atmosphere in contact with the sample are of crucial importance, therefore the observed temperatures inducing changes are not necessarily the equilibrium temperatures.

In DTA the temperature of the test material is measured relative to that of an adjacent inert material. A thermocouple imbedded in the test piece and another in the inert material are connected so that any differential temperatures generated during the heating cycle are graphically recorded as a series of peaks. The temperatures should be equal until a thermal event such as decomposition, melting or change in crystal structure takes place. In such a case the sample temperature either lags behind (endothermic event), or leads (exothermal event). The results are presented as  $\Delta T$  against temperature.

In DSC a sample and a referent material are used as well, but here the cell design is different. The sample and reference are maintained at the same temperature during heating and the extra heat input (to sample or reference depending on either the process being endo- or exothermal) required to keep the balance is measured. Therefore, enthalpy changes are directly measured.

The principal assembly of a thermoanalyzer is given in Figure 3.2.9. The equipment used in this work is from the Netzsch company; DTA/TG device STA 409.

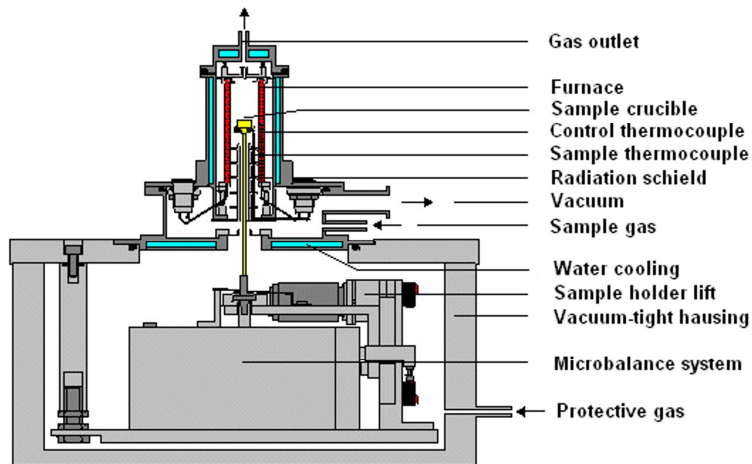


**Figure 3.2.9** Schematic representation of a thermal analyzer

### 3.2.6 Electrical and Ionic Conductivity Measurements

For the electrical conductivity measurements the Van der Pauw method<sup>18, 19</sup> is used, where the resistance of sample is measured with respect to its geometry. Figure 4.2.10 shows a schematic drawing of that experiment. The contacts are numbered from 1 to 4 in a counter-clockwise order. The current  $I_{12}$  is a positive DC current injected into contact 1 and taken out of contact 2, measured in amperes (A). The voltage,  $V_{34}$ , is a DC voltage measured between contacts 3 and 4

with no externally applied magnetic field, measured in volts (V). The resistance  $R_S$  is measured in ohms ( $\Omega$ ) and calculated from the Ohm's law (3.2.2):

$$R_{12,34} = \frac{V_{34}}{I_{12}} \quad (3.2.2)$$

The conductivity is normally given as S/m and according to the numbers one can define different compound classes; metallic conductors with  $10^6$ - $10^4$  S/m, semiconductors  $10^0$ - $10^{-6}$  S/m and insulators up to  $10^{-10}$  S/m.<sup>20</sup>

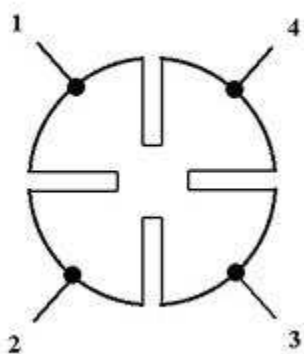


**Figure 3.2.10** Van der Pauw contact placement

The ionic conductivity<sup>21</sup> is measured by electrochemical impedance spectroscopy, a technique, measuring the dielectric properties of a medium as a function of frequency.<sup>22-25</sup> Electrical impedance extends the concept of resistance to alternating current circuits (AC), describing not only the relative amplitudes of the voltage and current, but also the relative phase. When the circuit is driven with direct current (DC), there is no distinction between impedance and resistance; the latter can be thought of as impedance with zero phase angles. After such measurement the total conductivity is defined and the electrical conductivity should be subtracted to get the conductivity due to ions.

The specific electrical resistance is measured with a self assembled device (Chemistry service group, Max Planck Institute für Festkörperforschung, Stuttgart). The samples are cooled with a cryostat (Fa. Keithley). The current is measured by a digital multimeter (Kryovac, Fa. Keithley) and the voltage is monitored by a nano-voltmeter (HP 4208, Fa. Hewett Packard). The temperature dependent AC impedance spectra are recorded with a Novocontrol Alpha A 4.2 analyzer combined with the impedance interface ZG 4 in a double-wire arrangement in the frequency region 0.5 to 20 MHz. Measurements and data recording are carried out with the

WinData program.<sup>26</sup> Typically, 50 mg sample are pressed in a press-tool with diameter of 6 mm, at 359 MPa. The pellet is sintered at 673 K for 48 h, and then placed between two ion-blocking silver electrodes in a quartz glass cell.<sup>27</sup>

The temperature dependence of the impedance spectra is fitted with WinFit<sup>28</sup> and the bulk ionic conductivity is determined by non linear mean square deviation.

### 3.2.7. Seebeck Effect Measurements

The Seebeck effect is one of the three so called thermoelectric effects; the other two are the Peltier effect, and the Thomson effect. In many textbooks, thermoelectric effect is called the Peltier–Seebeck effect. This separation derives from the independent discoveries of French physicist Peltier and Estonian-German physicist Seebeck. The Peltier–Seebeck and Thomson effects can in principle be thermodynamically reversible<sup>29</sup>. The thermoelectric effect is the direct conversion of temperature differences to electric voltage and vice versa. A thermoelectric device creates a voltage when there is a different temperature on each side. Conversely when a voltage is applied to it, it creates a temperature difference (known as the Peltier effect). At atomic scale an applied temperature gradient causes charged carriers in the material, whether they are electrons or electron holes, to diffuse from the hot side to the cold side, similar to a classical gas that expands when heated; hence, the thermally induced current. This effect can be used to generate electricity, to measure temperature, to cool objects, or to heat them or cook them. Because the direction of heating and cooling is determined by the polarity of the applied voltage, thermoelectric devices make very convenient temperature controllers. The Seebeck effect is the conversion of temperature differences directly into electricity.

There is a value called *figure of merit*, which is important for the thermoelectric devices, given by the formula (3.2.3):

$$Z = \frac{\sigma * \alpha^2}{k} \quad (3.2.3)$$

Where  $\sigma$  is the electrical conductivity,  $\alpha$  is the Seebeck coefficient and  $k$  the thermal conductivity. If one would like to get the *dimensionless figure of merit*  $ZT$ , an average temperature is necessary. Values of  $ZT = 1$  are considered good, and values of at least the 3–4 range are considered to be essential for thermoelectrics to compete with mechanical generation and refrigeration in efficiency. To date, the best reported  $ZT$  values have been in the 2–3 range<sup>30, 31</sup>. The Seebeck coefficient is expressed as follows:

$$\alpha = \frac{k_B}{e} \left[ \ln\left(\frac{N_D}{n}\right) + C \right] \quad (3.2.4)$$

Where  $k_B$  is the Boltzmann constant,  $e$  the electronic charge,  $N_D$  the density of states,  $n$  the carrier density,  $C$  the transport constant. That equation suggests that high density of states leads to high Seebeck coefficient.

The Seebeck coefficient (the thermopower) of the material depends mostly of the material's temperature and the crystal structure. As far as it measures the magnitude of an induced thermoelectric voltage in response to a temperature difference across that material from its sign – positive or negative one can draw conclusion for the charge carriers in the materials – electrons or holes respectively. Only an increase in the temperature difference can resume a build up of more charge carriers on the cold side and thus lead to an increase in the thermoelectric voltage. Incidentally the thermopower also measures the entropy per charge carrier in the material. To be more specific, the partial molar electronic entropy is said to equal the absolute thermoelectric power multiplied by the negative of Faraday's constant<sup>32</sup>.

The measurements of thermoelectric power (Seebeck coefficient) of the samples were carried out in a homemade device, developed by Professor Dr. Jose Rivas Rey's Group of Solids Magnetism, from the Department of Applied Physics in the University of Santiago de Compostela shown in Figure 3.2.11. This equipment allows carrying out measurements ranging from 85 K to 450 K, and consists of:

- Nitrogen cryostat where is introduced the measurement cell.

- A sample holder, consisting of two teflon cylinders, inside each one there is a copper block in where there is a heater coil which creates the temperature gradient between the two blocks. The sample is located between two copper plates.
- A nanovoltmeter, to measure the voltage difference generated due to the temperature difference.
- Two temperature controllers to regulate the temperature gradients.

Measures in this equipment were made as follows: the samples in form of tablets were placed between the two copper plates covered with gold and then the potential difference generated by applying a temperature difference  $T = 1 \text{ K}$  between the plates was measured.

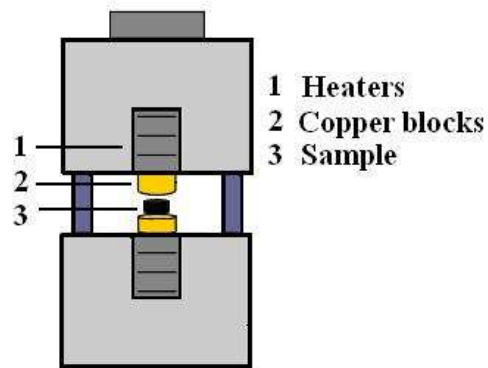


Figure 3.2.11 Cell for thermoelectric power measurement

### 3.2.8 Magnetic Measurements

The principle aim of magnetometry is to measure the magnetization (either intrinsic or induced by an applied field) of a material. This can be achieved in a number of ways utilizing various magnetic phenomena. The various types of magnetometers fall within two categories:

1. Measuring the force acting on a sample in an inhomogeneous magnetic field
  - Magnetic balance
  - Magnetic pendulum

## 2. Measuring the magnetic field produced by a sample.

- Vibrating Sample Magnetometer (VSM)
- Superconducting Quantum Interference Device (SQUID)

Magnetometry data in this thesis has been recorded using a SQUID. The SQUID device consists of two superconductors separated by thin insulating layers to form two parallel Josephson junctions. The device may be configured as a magnetometer to detect incredibly small magnetic fields. Therefore, SQUIDs are very sensitive vector magnetometers, with noise levels as low as  $3 \text{ fT/Hz}^{0.5}$  in commercial instruments and up to  $0.4 \text{ fT/Hz}^{0.5}$  in experimental devices. The great sensitivity of the SQUIDs is associated with measuring changes in magnetic field associated with one flux quantum. One of the discoveries associated with Josephson junctions was that flux is quantized in units. If a constant biasing current is maintained in the SQUID device, the measured voltage oscillates with the changes in phase at the two junctions, which depends upon the change in the magnetic flux. Counting the oscillations allows one to evaluate the flux change which has occurred. A schematic representation of a SQUID device is shown in Figure 3.2.12. The SQUID magnetometer used for the purpose of this doctoral thesis, MPMS 5.5. Fa. Quantum Design, is utilized in the temperature range between 2 and 330 K.

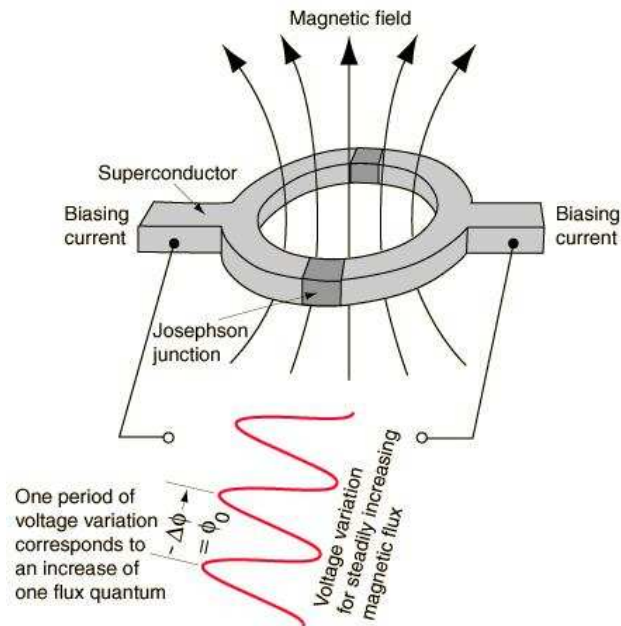


**Figure 3.2.12** Schematic representation of a SQUID magnetometer



## 4. Special Part

### 4.1. Ternary and quaternary silver oxides – literature overview and motivation

The delafossite structure was first reported by Friedel in 1873, a copper - iron mineral, named after the french mineralogist and crystallographer Gabriel Delafosse.<sup>33</sup> Later it was confirmed that the synthetic  $\text{CuFeO}_2$  has the same structure as the mineral.<sup>34</sup> The structure is build up of alternating layers of two - dimensional closed packed  $\text{Cu}^+$  with linear coordinated O and slightly distorted edge - shared  $\text{FeO}_6$  octahedra. The oxygen is coordinated by one  $\text{Cu}^+$  and three  $\text{Fe}^{3+}$  cations in a pseudo tetrahedral arrangement. The sum formula of that class of compounds is  $A^+B^{3+}O_2^-$ , with  $A = \text{Ag, Cu, Pd or Pt}$ , and  $B$  being a trivalent cation from the d-block elements. Furthermore the ionic radii of the  $B$ -site ions should be in the range  $0.53 \text{ \AA} < r(B^{3+}) < 1.03 \text{ \AA}$ .<sup>35, 36</sup> Depending on the stacking of the double layers (close-packed  $A^+$  cations and  $BO_6$  octahedra), two polytypes are prevailing, a rhombohedral 3R ( $R\bar{3}m$ ) and a hexagonal 2H ( $P6_3/mmc$ )<sup>37, 38</sup> structures. According to the Ramsdell<sup>39</sup> nomenclature the numbers 3 and 2 refer to the number of layers after which the stacking is repeated, and the letters R or H to the crystal system – rhombohedral or hexagonal, respectively. The two polytypes are shown in Figure 4.1.1.

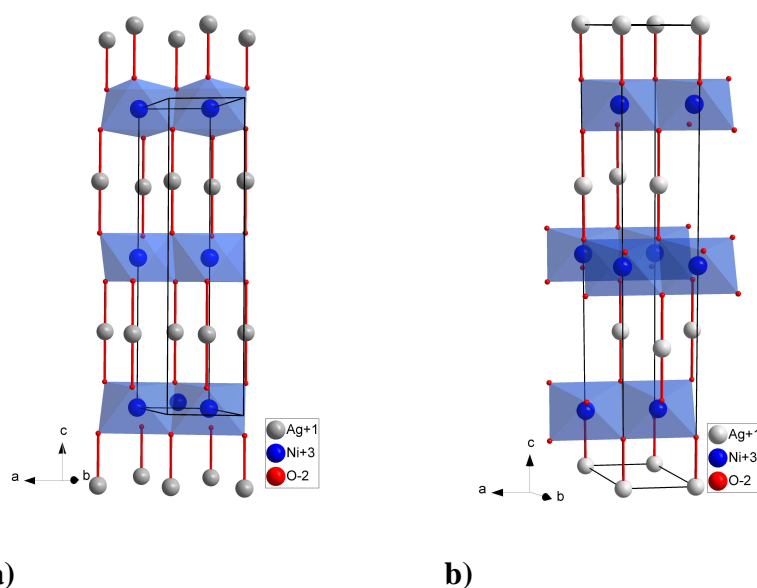


**Figure 4.1.1.** The two polytypes of  $\text{AgNiO}_2$ . a) 2H – type of the delafossite, “AaBbAaBb”<sup>40</sup>, b) 3R - type of the delafossite, “AaBbCcAaBbCc”.<sup>4</sup>

Both polytypes exhibit a two - dimensional equilateral triangular lattice by  $A^+$  with the edge length being equal to the length of the  $a$  axis<sup>41</sup>. While the  $a$  cell edge increases with increasing ionic radii of  $B^{3+}$ , the  $c$  cell parameter does not change significantly. For a full structural description of these compounds, only the cell parameters and the  $z$  coordinate of O are necessary because the cations are located on special positions. (Table 4.1.1. and Table 4.1.2.)

Table 4.1.1. Atomic position of 3R – type  $CuFeO_2 (R\bar{3}m (166))^{38}$

Atom	Wyckoff Position	$x$	$y$	$z$
A	$3a$	0	0	0
B	$3b$	0	0	1/2
O	$6c$	0	0	0.1066(5)

Table 4.1.2. Atomic position of 2H – type  $CuFeO_2 (P6_3/mmc (194))^{42}$

Atom	Wyckoff Position	$x$	$y$	$z$
A	$2a$	1/3	2/3	1/4
B	$2b$	0	0	0
O	$4c$	1/3	2/3	0.0892(2)

Structures, which have the same general formula and are built up from particular identical building blocks, can be described as belonging to a structural family<sup>43</sup>. The structure field diagram of compounds with general formula  $A^+B^{3+}O_2^{2-}$  is shown in Figure 4.1.2.. The structures are classified according to different polytypes, where  $\alpha$  -  $NaFeO_2$  and  $\beta$  -  $NaFeO_2$  are the most common ones. If  $A^+$  is an alkali metal the compounds crystallize in the  $\alpha$  -  $NaFeO_2$  structural type in the  $R\bar{3}m$  space group, where the coordination of  $A^+$  by oxygen is not longer linear but octahedral; examples are  $NaFeO_2^{44}$ ,  $LiCoO_2^{45}$ ,  $NaCoO_2^{46}$ ,  $NaRhO_2^{47}$ ,  $LiNiO_2^{48}$  etc.. In the  $\beta$  -  $NaFeO_2$  type, all cations are tetrahedrally coordinated, the structure is orthorhombic and the compounds crystallize in the  $Pn2_1a$  space group, e.g.  $LiGaO_2^{49}$ ,  $NaGaO_2^{50}$ . If the ratio  $r_{A^+}/r_{B^{3+}}$  is bigger than 1.6 and  $B^{3+}$  ion is relatively large cation, the favored structure type is  $\beta$  -

RbScO<sub>2</sub><sup>51</sup>, where the Sc is octahedrally coordinated by oxygen and the coordination of Rb is a trigonal prism, e.g. CsYO<sub>2</sub><sup>52</sup>.

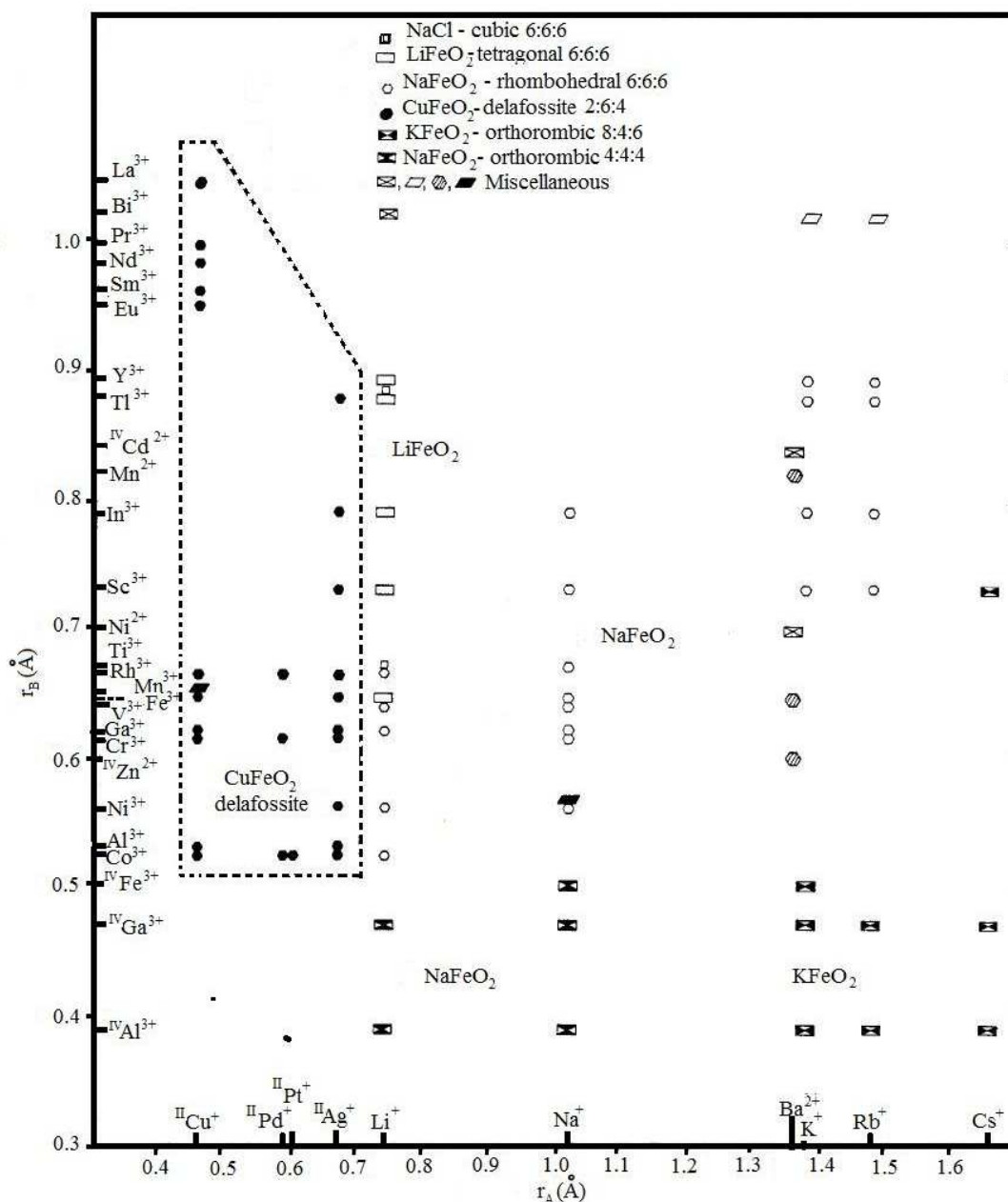


Figure 4.1.2. Structure field diagram for ABO<sub>2</sub> type compounds<sup>43</sup>.

For a  $r_A/r_B$  ratio between 1.13 - 1.17, two modifications exist. For example NaTiO<sub>2</sub><sup>53</sup> crystallizes in a low- and high temperature form, the low-temperature phase exhibits a cubic rock salt type of structure, with a statistical arrangement of the cations, whereas the high-temperature modification belongs to the  $\alpha$ -NaFeO<sub>2</sub> type. If the cation ratio is 0.86, e.g. for

LiTiO<sub>2</sub><sup>54</sup>, different types of structures can be realized, depending on the temperature: a rhombohedral (480 – 570 ° C)<sup>55</sup>, a tetragonal (570 – 640 ° C) or a rock salt type of structure (above 640 ° C). In the literature quaternary oxides  $A^+(M_{1-x}M_x)^{3+}O_2$  with delafossite type structure have been investigated mainly in terms of their physical properties<sup>56-58</sup> and just a few structural reports can be found<sup>59, 60</sup>. Both modifications 3R and 2H occur exhibiting either fully ordered or disorder  $M / M'$  site<sup>59, 61-63</sup>.

The delafossite compounds are interesting not only because of their structural properties, but also because of their different physical properties, which explain the considerable variety of their application. In this respect the specific cation combination is of significant importance. Kawazoe et al.<sup>64</sup> showed in their work for example that the incl... of Cu<sup>+</sup> and Ag<sup>+</sup> (d<sup>10</sup> ions) improves optical properties. The authors reported 70% transmission of visible light by a thin film of CuAlO<sub>2</sub>. Further transparent conducting oxides, which belong to that family, are studied by Ginley<sup>65</sup>. Formally, if improvement of the electrical properties is the main goal, Pd<sup>+</sup> or Pt<sup>+</sup> cations on A<sup>+</sup> site are preferred.<sup>66, 67</sup> Owing to the optical absorption from d – d electron transmission, trivalent B – site cations suitable for transparency must possess empty or closed d – shells, while partially filled d – electron shells are more appropriate for catalysts<sup>68-71</sup> or batteries<sup>72-74</sup>. Another important property of this family of compounds is luminescence<sup>75-77</sup>, or the thermoelectric properties observed in many systems as AgIn<sub>1-x</sub>Sn<sub>x</sub>O<sub>2</sub><sup>78</sup>, CuFe<sub>1-x</sub>Ni<sub>x</sub>O<sub>2</sub><sup>79</sup>, CuCr<sub>1-x</sub>Ni<sub>x</sub>O<sub>2</sub><sup>80</sup>, CuAlO<sub>2</sub><sup>81</sup>, CuLaO<sub>2</sub><sup>82, 83</sup>.

One should point out that almost all synthesis methods described in previous part might be used and have been used, the final choice depends mostly on the stability of the oxides (decomposition point).

Within this thesis, the first goal was the synthesis of AgRhO<sub>2</sub> and AgIrO<sub>2</sub> in a delafossite arrangement and their structural characterization. Two modifications of AgCoO<sub>2</sub> are reported in the literature<sup>38, 84, 85</sup>. Further, silver de- or intercalation is of particular interest, in order to obtain new compounds containing mixed valence transition metals or subvalent silver. All those possible compounds could provide better understanding on basic questions concerning the nature of chemical bonds, the orbital interactions and phenomena as charge ordering or Jahn-Teller distortion. Another challenge was the synthesis of new quaternary delafossite oxides ( $A^+(Li_{1/3}^+M_{2/3}^{4+})O_2^{2-}$ ), and consistently comparison between their structures and physical properties with those of the analogues ternary transition metal oxides.

#### 4.1.1. Systems Rh – O and Li – Rh – O

In the context of our investigations on delafossite,  $\text{RhO}_2$  and  $\text{Li}_2\text{RhO}_3$  serve as starting and reference materials.

$\text{RhO}_2$  is a black air stable powder, with low degree of crystallinity. It crystallizes in rutile type structure –  $P4_2/mnm$ , as known for many oxides  $\text{MO}_2$  ( $M = \text{Pb, Ti, Cr, Rh, Ir}$  etc.) or fluorides  $\text{MF}_2$  ( $M = \text{Mn, Mg, Co, Fe, Ni}$  etc.). Some of these compounds are of importance for industry because of their physical properties. Examples are  $\text{TiO}_2$  as a white pigment in the paints and floor polishes<sup>86</sup>, and  $\text{CrO}_2$  with its ferromagnetic behavior at room temperature, used for long as magnetic recording material for data storage. The synthesis of some of those oxides -  $\text{CrO}_2$ <sup>87, 88</sup>,  $\text{RhO}_2$ <sup>87, 89</sup> is not possible at ambient conditions, instead requires to apply high oxygen pressure.

$\text{Li}_2\text{RhO}_3$  is also a black air stable powder with quite good crystallinity. The compound belongs to the family of  $\text{Li}_2\text{MO}_3$  oxides ( $M$  any element capable to display 4+ oxidation number) which have layered structures. The packing is built up from oxygen atoms and the layers of octahedral interstices are alternately filled either with  $\text{Li}^+$  only, or with  $1/3 \text{Li}^+$  and  $2/3 M^{4+}$ . The transition-metal containing layers are further ordered into a continuous honeycomb-like network. Two polymorphs displaying those characteristics are known, the  $\text{Li}_2\text{SnO}_3$ -type<sup>90-92</sup> in  $C2/c$ , or to the  $\text{Li}_2\text{MnO}_3$ -type<sup>93, 94</sup> in  $C2/m$  space group. There are data on  $\text{Li}_2\text{MnO}_3$ ,  $\text{Li}_2\text{SnO}_3$  and  $\text{Li}_2\text{IrO}_3$  indicating the compounds to be fully ordered,<sup>91, 93, 94</sup> as well as reports on partially disordered structures<sup>95-97</sup>.

##### 4.1.1.1. Synthesis of $\text{RhO}_2$ and $\text{Li}_2\text{RhO}_3$

###### **$\text{RhO}_2$**

High pressure oxygen autoclaves were used to synthesize single phase  $\text{RhO}_2$ . This synthesis method was chosen according to the phase stability diagram of Rh – O system<sup>98</sup>. As starting material  $\text{Rh}(\text{NO}_3)_3 \cdot x\text{H}_2\text{O}$  (ChemPur, 36% Rh ) was used. The powder was filled in a glass tube and decomposed in air at 473 K for 48 h. The obtained amorphous residue was treated at 50-70

MPa oxygen pressure and a temperature of 723 K for 60 hours. The powder diffraction pattern of calculated and measured  $\text{RhO}_2$  is shown in Figure 4.1.3.

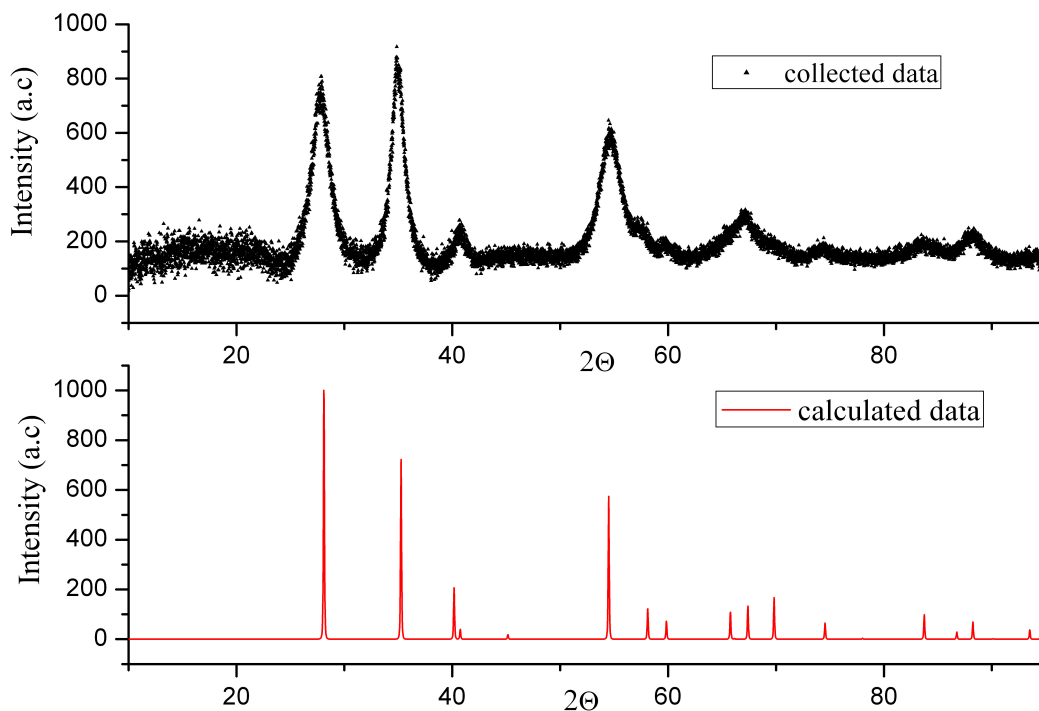


**Figure 4.1.3.** Powder pattern of measured and calculated  $\text{RhO}_2$  ( $P4_2/mnm$ )

### **$\text{Li}_2\text{RhO}_3$**

$\text{Li}_2\text{RhO}_3$  was prepared by reacting stoichiometric mixtures of  $\text{RhO}_2$  and  $\text{LiOH}$  (Alfa Aesar, anhydrous 99.9%). The mixture was carefully ground, placed in corundum crucible and heated with 10 K/min up to 1123 K in an oxygen flow, the sample was held at that temperature for 48 h before cooling down to room temperature with the same rate as heating. The powder diffraction pattern of calculated and measured  $\text{Li}_2\text{RhO}_3$  is shown on Figure 4.1.4.

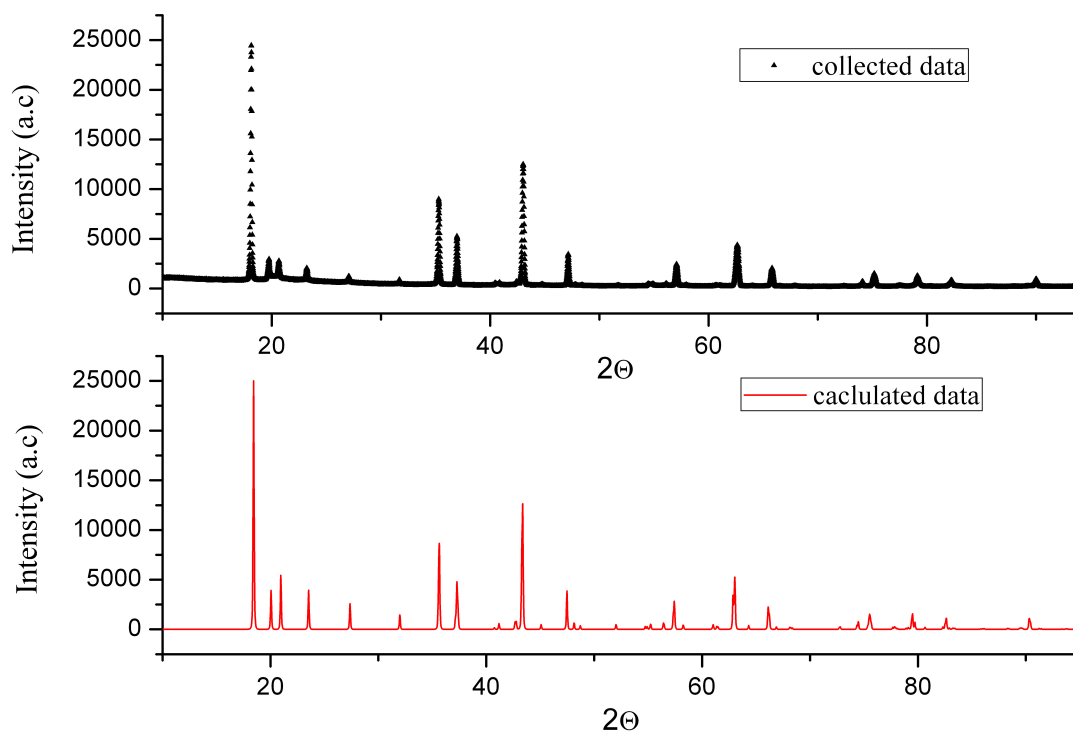


**Figure 4.1.4.** Powder pattern of measured and calculated  $\text{Li}_2\text{RhO}_3$  ( $C2/m$ ).

#### 4.1.1.2. Structural characterization of $\text{RhO}_2$ and $\text{Li}_2\text{RhO}_3$

##### $\text{RhO}_2$

The cell parameters of  $\text{RhO}_2$  were refined using the LeBail method with space group  $P42/mnm$ . The LeBail fit comply well with the literature data<sup>99, 100</sup> and the refined lattice constant  $a = 4.41(1) \text{ \AA}$  and  $c = 3.051(1) \text{ \AA}$  are as expected. Figure 4.1.5. shows the results of the cell refinement.

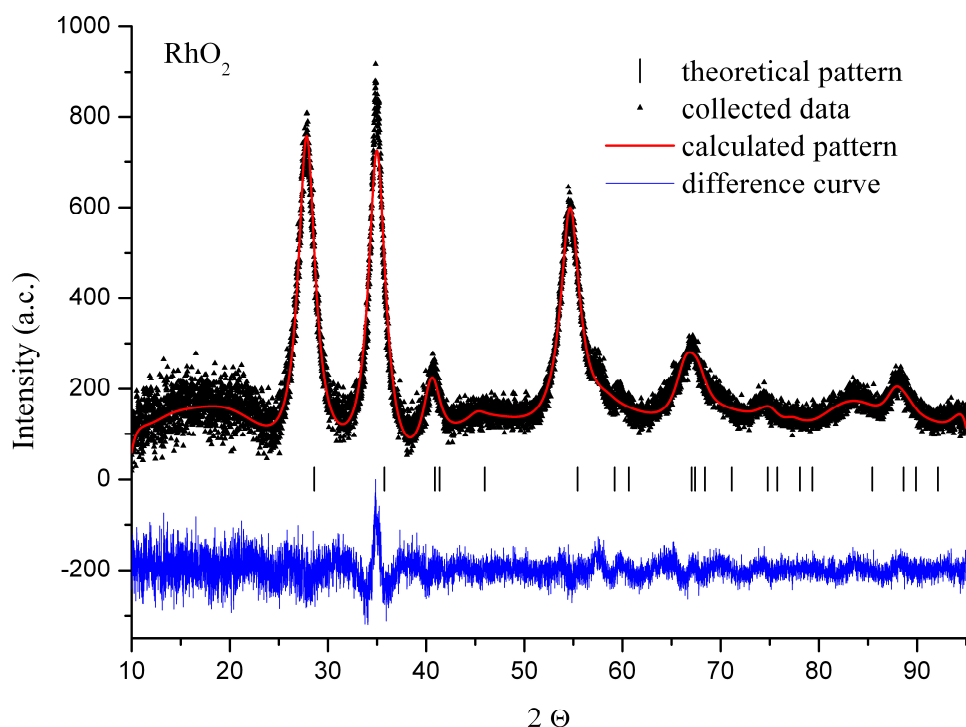


**Figure 4.1.5.** LeBail fit of  $\text{RhO}_2$  ( $P42/mnm$ ).

### $\text{Li}_2\text{RhO}_3$

The structural similarity of  $\text{LiRhO}_2$ <sup>101</sup> and  $\text{Li}_2\text{RhO}_3$  easily follows up from their building principles, based on a ccp arrangement of oxygen. As already mentioned there are two polymorphs known for the family of  $\text{Li}_2\text{MO}_3$ , with space groups  $C2/m$  or  $C2/c$ , depending on the  $\text{LiM}_2$  order<sup>91, 93, 94, 96, 102</sup>. In the literature, there is some debate on the proper choice of unit cell and space group symmetry for the  $\text{Li}_2\text{MO}_3$  phases. In particular, previous studies<sup>90, 103</sup> suffered from insufficient angular resolution of the powder patterns, and erroneously trigonal or orthorhombic crystal systems were assigned. Single crystal work<sup>91, 94</sup> eventually has settled this issue. Thus far, two polymorphs, the  $\text{Li}_2\text{MnO}_3$  - type<sup>93</sup> and  $\text{Li}_2\text{SnO}_3$  - type<sup>91</sup> have been confirmed.  $\text{Li}_2\text{RhO}_3$  crystallizes in space group  $C2/m$  with cell parameters  $a = 5.1198(1)$ ,  $b = 8.8497(1)$ ,  $c = 5.1030(1)$  Å,  $\beta = 109.61(6)^\circ$  and  $Z = 4$ , isostructural to  $\text{Li}_2\text{MnO}_3$ <sup>93, 94</sup>. The structural parameters were refined using the Rietveld procedure, the experimental and calculated powder patterns are shown in Figure 4.1.6 and the refined parameters are given in Table 4.1.3. and Table 4.1.4.



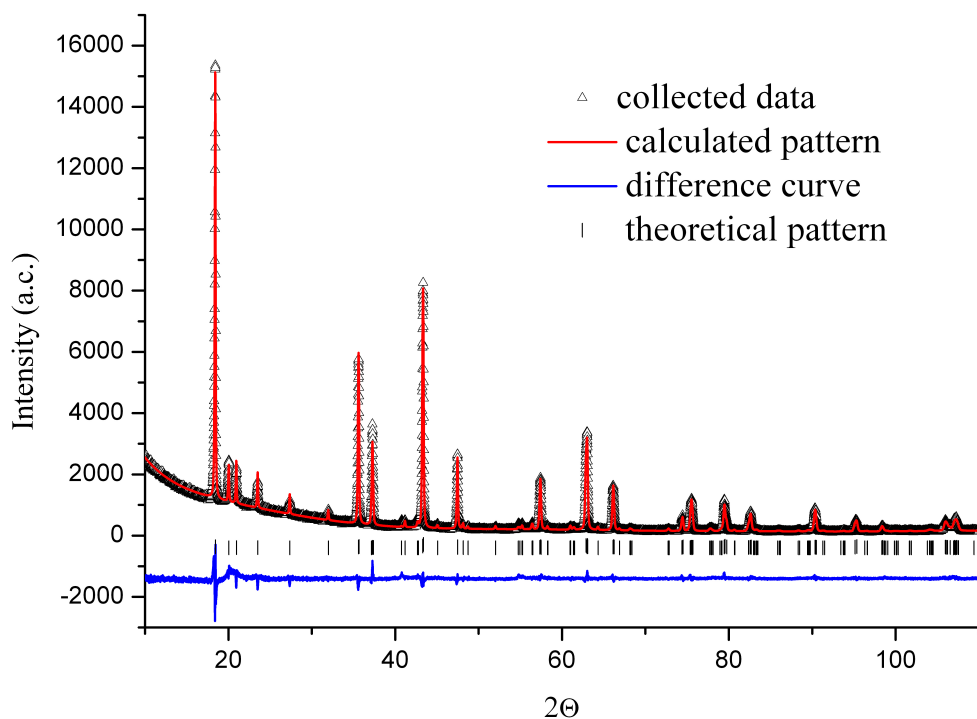


**Figure 4.1.6.** Observed (black), calculated (red) and difference (blue) tracks of X-ray powder diffraction for  $\text{Li}_2\text{RhO}_3$ . Tick marks represent the calculated peak positions.

Table 4.1.3. Atomic positions of  $\text{Li}_2\text{RhO}_3$ .

Atom	Wyckoff Positions	$x$	$y$	$z$	Occ.	Beq
Rh(1)	4g	0	0.333	0	0.869(3)	0.01
Li(1)	4g	0	0.333	0	0.131(3)	0.02
Rh(2)	2a	0	0	0	0.263(2)	0.01
Li(2)	2a	0	0	0	0.737(2)	0.02
Li(3)	4h	0	0.819(1)	0.5	1	0.02
Li(4)	2d	0	0.5	0.5	1	0.02
O(1)	8j	0.245(1)	0.321(1)	0.759(1)	1	0.03
O(2)	4i	0.255(1)	0	0.773(1)	1	0.03

Table 4.1.4. Crystallographic and refinement details for  $\text{Li}_2\text{RhO}_3$  refined by the Rietveld method.

Space group	$C2/m$
$a / \text{Å}$	5.1198(1)
$b / \text{Å}$	8.8497(1)
$c / \text{Å}$	5.1030(1)
$\beta / ^\circ$	109.61(2)
$V / \text{Å}^3$	217.80(1)
$Z$	4
Rexp (%)*	3.81
Rp (%)*	4.98
Rwp (%)*	6.93
gof *	1.82
R(F2) (%)*	2.63

In  $\text{Li}_2\text{RhO}_3$ , every second inter layer of octahedral voids is occupied exclusively by lithium, whereas the remaining octahedral sites are statistically occupied by lithium and rhodium with an average ratio of 1:2 (Figure 4.1.7). From the data of the Rietveld refinement and the elemental analysis the ratio between Li, Rh and O was established to be 2:1:3. The Li–O and Rh–O bond distances cover the range from 1.992 – 2.274 Å, and thus are in a good agreement with the typical values found for ternary oxides of Li and Rh<sup>104-108</sup>. The same crystal structure also displaying disorder on  $\text{Li}^+$  and  $\text{Ir}^{4+}$  sites has been reported for  $\text{Li}_2\text{IrO}_3$ <sup>95,96</sup>, previously. Considering the big difference in the atomic masses of  $\text{Li}^+$  and  $\text{Rh}^{4+}$ , a small deviation from the ideal stoichiometry would cause a big density difference. Therefore, the density of the synthesized material was measured and compared to the crystallographically calculated one. It was found that both values are in a good agreement (calculated: 5.11 g cm<sup>-3</sup>, measured: 5.09 g cm<sup>-3</sup>). Additionally, the bond valence sums of Li, Rh and O in  $\text{Li}_2\text{RhO}_3$  were determined

according to the method of Brown and Altermatt<sup>109, 110</sup>. As it is shown in Table 4.1.5, the valence sums are in good agreement with the expected average oxidation states.

Table 4.1.5. Bond distances and bond valence sums, which are calculated for the most abundant ion in case of partial occupancy.

Bond Type	Bond Length (Å)	Number of Bonds	Bond Valence	Bond Valence Sum
Rh1/Li1-O1	1.996(6)	2	0.6839	<b>3.87</b>
	2.048(7)	2	0.5940	
Rh1/Li1-O2	2.012(6)	2	0.6548	
Rh2/Li2-O1	2.013(9)	4	0.2155	<b>1.31</b>
Rh2/Li2-O2	1.992(2)	2	0.2286	
Li3-O1	2.045(8)	2	0.2086	<b>0.93</b>
	2.188(9)	2	0.1417	
Li3-O2	2.274(4)	2	0.1125	
Li4-O1	2.122(9)	4	0.1694	<b>0.96</b>
Li4-O2	2.187(8)	2	0.1421	
O1- Rh1/Li1	1.996(6)		0.6838	<b>2.17</b>
O1- Rh2/Li2	2.013(9)		0.2275	
O1- Rh1/Li1	2.048(7)		0.5940	
O1- Li3	2.045(8)		0.2087	
O1- Li4	2.018(8)		0.2245	
O1- Li3	2.122(9)		0.1694	
O1- Rh1/Li1	2.012(6)	2	0.6838	<b>1.962</b>
O1- Rh2/Li2	1.992(2)		0.2274	
O1- Li3	2.274(4)	2	0.1124	
O1- Li4	2.188(9)		0.1417	

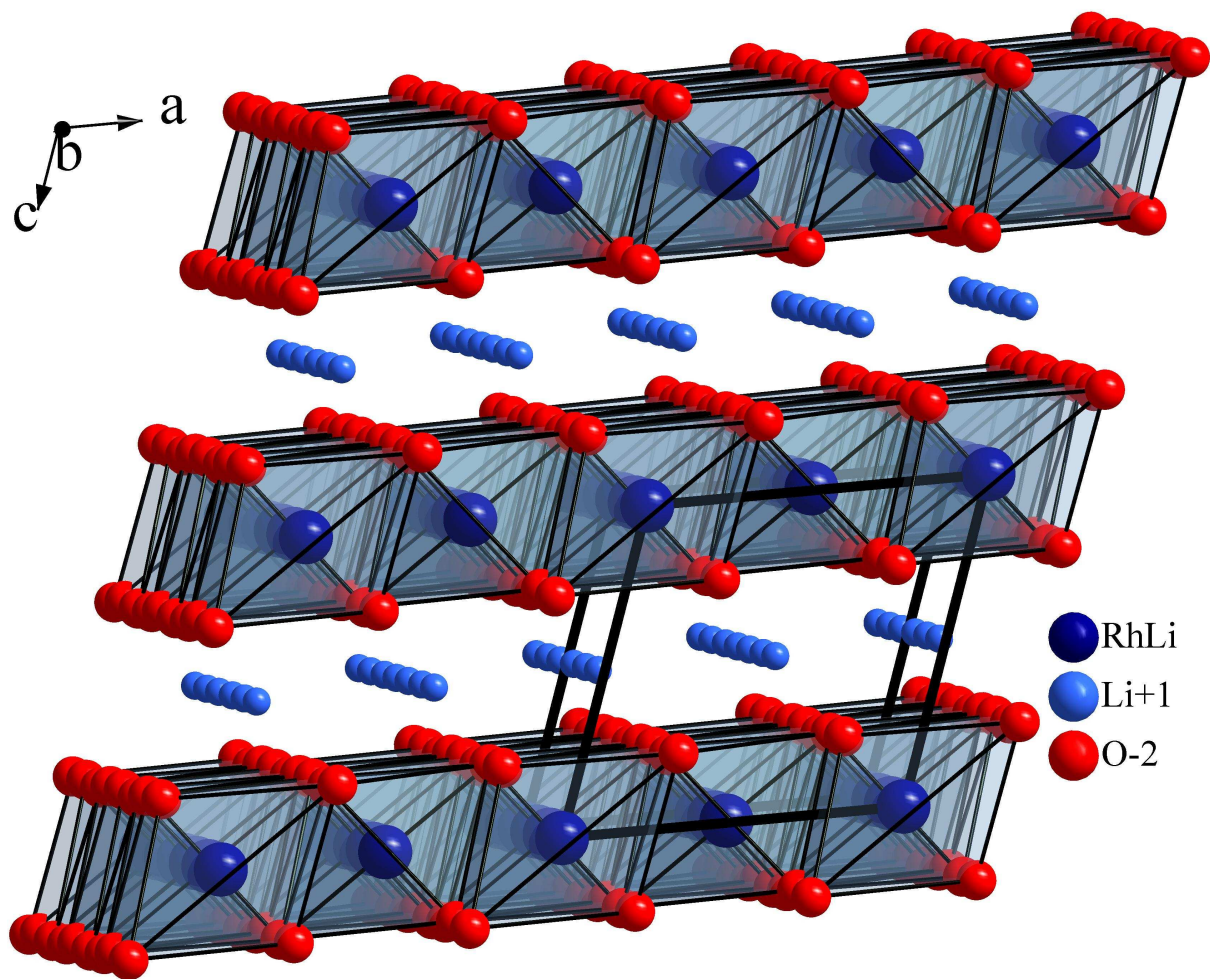


**Figure 4.1.7.** Structure of  $\text{Li}_2\text{RhO}_3$ , with view along the  $b$ -axis.

#### 4.1.1.3. Physical characterization of RhO<sub>2</sub> and Li<sub>2</sub>RhO<sub>3</sub>

##### RhO<sub>2</sub>

The thermal stability was reported by G. Bayer and H. G. Wiedemann<sup>89</sup>. RhO<sub>2</sub> decompose irreversibly and probably topotactically to  $\alpha$  – Rh<sub>2</sub>O<sub>3</sub> above 1023 K and 1 atmosphere oxygen partial pressure. That phase transition is imaginable, because both structure – rutile and corundum have similar hexagonal oxygen packing, but different occupancy of the interstitial octahedral voids. The thermal decomposition of the  $\alpha$  – Rh<sub>2</sub>O<sub>3</sub> and  $\beta$  – Rh<sub>2</sub>O<sub>3</sub> depends on the oxygen pressure. Around 1173 K and normal pressure a phase transition from  $\alpha$  – into  $\beta$  - form accrues, not detectable in the DTA signal, followed by decomposition above 1403 K.

##### *Magnetic Susceptibility*

The magnetic susceptibility was measured as function of the temperature for different magnetic fields at 0.1, 1, 3 and 7 T. Rh<sup>4+</sup> is a d<sup>5</sup> system and in ideal case could have spin 1/2 ( $\mu_{\text{eff}} = 1.73 \mu_{\text{B}}$ , low-spin configuration) or 5/2 ( $\mu_{\text{eff}} = 5.92 \mu_{\text{B}}$ , high-spin configuration) indicating paramagnetic behavior. Figure 4.1.8. shows the molar susceptibility and its reverse as a function of temperature, indicating such a paramagnetic behavior. The deviation from the linearity at low temperatures highly indicates ferromagnetic impurities, if the molar susceptibility is field dependent. After applying Honda<sup>111</sup> Owen<sup>112</sup> correction the curve displaying the reverse susceptibility as function of temperature must be linear. In the temperature range from 150 to 300 K the Curie law was applied and an effective magnetic moment of 4.51  $\mu_{\text{B}}$  was calculated. This number is too small for the high-spin configuration of Rh<sup>4+</sup> and too big for the low-spin configuration. Therefore an assumption that the Rh<sup>4+</sup> sample is contaminated with Rh<sup>3+</sup> species ( $\mu_{\text{eff}} = 4.9 \mu_{\text{B}}$ , S = 2, high spin of Rh<sup>3+</sup>) was made, furthermore there is a report about the mixed valence  $[\text{Rh}^{4+}_{1-x}\text{Rh}^{3+}_x\text{O}_{2-x}(\text{OH})_x]$ <sup>113</sup>. The equations 4.1.1 and 4.1.2 were applied in order to determine the potential amount of Rh<sup>3+</sup> ions but no conclusive solution was found, as well as no evidence of H<sub>2</sub>O or OH were found (Appendix Figure 1).

$$\chi = v \times \chi_{Rh^{4+}} + (1-v) \times \chi_{Rh^{3+}} \quad (4.1.1)$$

$$\mu_{eff} = \sqrt{v \times \chi_{Rh^{4+}}^2 + (1-v) \times \chi_{Rh^{3+}}^2} \quad (4.1.2)$$

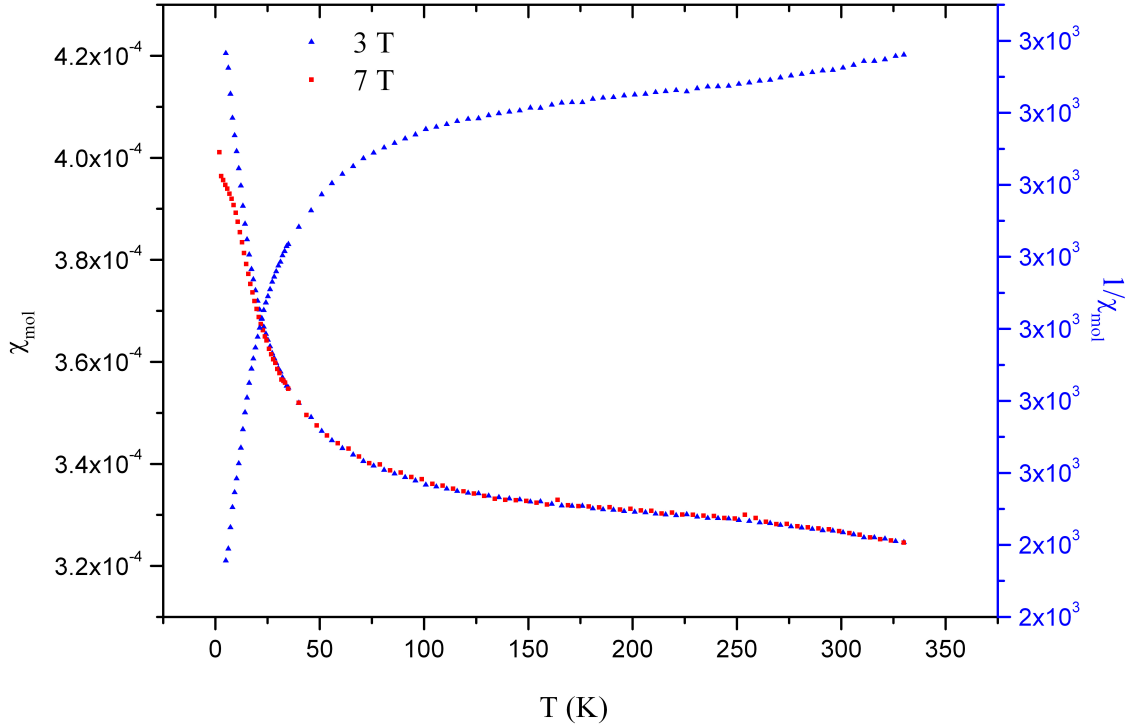


**Figure 4.1.8.** Molar susceptibility and inverse molar susceptibility for  $RhO_2$  as a function of temperature.

Another possible explanation would be, that the five d-orbitals of rhodium are not more fully degenerated<sup>87</sup>. According to Goodenough<sup>114</sup> that can be derived from the rutile structure (Figure 4.1.9a). In that work the structural family has been investigated and the importance of the  $c/a$  ratio discussed. The phenomenological parameter  $B$  is introduced expressing the interaction between d – orbitals of an atom and its neighbors. The parameter  $B$  can be related to physically measurable parameters like the cation - cation distance  $R_{cc}$  ( $R_{cc}$  is the distance between cations along  $c$  axis). Furthermore the variable  $\lambda_\pi$ , and the constants  $R_c$  and  $\lambda_c$  have been postulated, where  $R_c$  is a critical distance for electrons localization or delocalization,  $\lambda_\pi$  is parameter of covalent coupling between the d-orbitals of the cation and  $p_\pi$  orbitals of the ion, and  $\lambda_c$  is a critical value of that parameter. The author distinguished between two classes of metal oxides, namely class I and class II (Figure 4.1.9b).

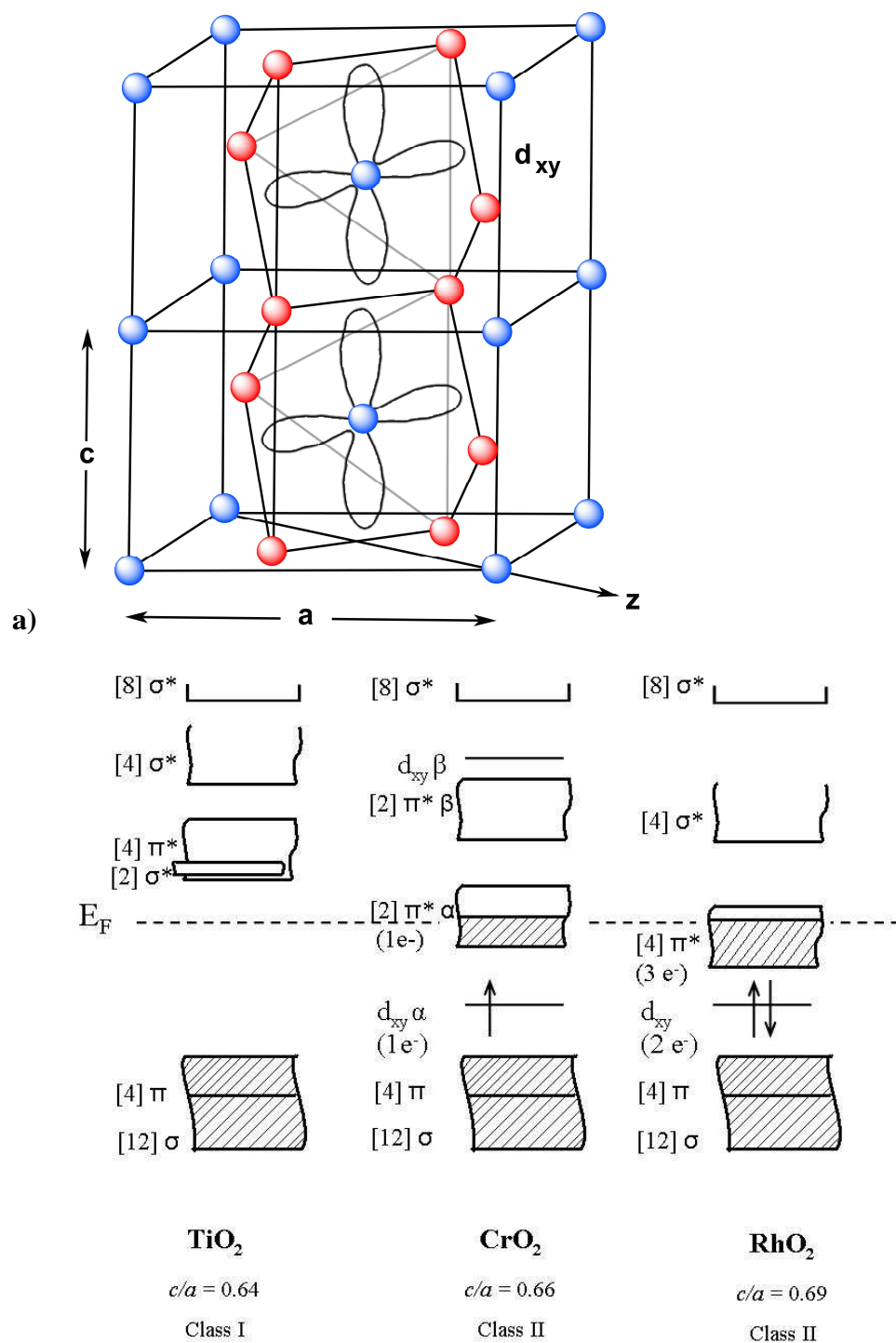


**Figure 4.1.9.** a) The structure of RhO<sub>2</sub> with delocalization of electrons in  $d_{xy}$ <sup>87</sup> viewing direction [110]. b) Energy level diagram of the two oxide classes<sup>114</sup>.

According to that classification, metal oxides showing high values of  $B$ , thus are the cation-cation interactions strong, results in short interatomic distance fulfilling  $R_{cc} < R_c$  and  $\lambda_\pi > \lambda_c$ , belong to the class I. In fact Goodenough postulated that  $\lambda_\pi > \lambda_c$  equation is fulfilled in all metal cations (+IV) except  $Mn^{4+}$ . In the case of metal oxide class II, the value of  $B$  is high but the interaction is not longer cation-cation, but cation-anion-cation, expressed with  $R_{cc} > R_c$  and  $\lambda_\pi > \lambda_c$ . An example for class I is  $TiO_2$ , where  $R_{cc} = 2.96 \text{ \AA}$ ,  $R_c = 3.00 \text{ \AA}$ , shown on Figure 4.1.9.b) left hand site; and for class II  $CrO_2$  (Figure 4.1.9.b) in the middle)  $R_{cc} = 2.92 \text{ \AA}$ ,  $R_c = 2.86 \text{ \AA}$ .

In the case of  $RhO_2$  (Figure 4.1.9.b) right hand site) the  $c/a$  ratio is above the critical value of 0.66 ( $CrO_2$ ) which favors the localization of the electrons in the  $d_{xy}$  ( $\parallel$  to the  $c$  axis). The residual three electrons are located in antibonding  $\pi^*$  orbital overlapping with the conductivity band.

Making use of that model, the magnetic behavior of  $RhO_2$  can be rational interpret. An effective magnetic moment of  $4.51 \mu_B$  is found applying Curie – Weiss law. As discussed,  $Rh^{5+}$  has to be considered as  $d^3$  system by calculating the ideal values for spin-only or for spin-orbit coupling, respectively. Via equations 4.1.3 and 4.1.4, the spin-orbit coupling for  $^4F$  system ( $L = 4$  and  $S = 3/2$ ) is calculated.

$$\mu_{eff} = g\sqrt{J(J+1)} \quad (4.1.3)$$

$$J = |L - S| \quad (4.1.4)$$

Where  $J$  is the spin-orbit coupling constant,  $\mu_{eff} = 3.87 \mu_B$  and  $\mu_{eff} = 5.92 \mu_B$  are calculated, normally numbers between the spin – only and the spin – orbit coupling is reported<sup>115</sup>, which correspond to the calculated for  $RhO_2$ . Analysis of the magnetic behavior of  $RhO_2$  was of interest as far as it was used as a precursor for the synthesis of  $Li_2RhO_3$ , which shows slightly bigger effective magnetic moment, as expected  $1.73 \mu_B$  (See Chapter 4.1.1 /4.1.1.3.).

### *Electronic Conductivity*

The measurement was performed in the temperature range from 3 to 300 K, and the result is in a good agreement with the magnetic behavior of the  $RhO_2$ . The resistivity increases with



increasing temperature over the whole temperature range (Figure 4.1.10). When an electrical potential difference is placed across the sample, its movable charges flow, giving rise to an electric current. The electrical conductivity is strongly dependent of the temperature and over a limited temperature range is approximately directly proportional to it. At ambient conditions the resistivity has a value of  $8.0 \cdot 10^{-3} \Omega \cdot \text{cm}$ , which leads to a specific conductivity of  $124.91 \Omega^{-1} \cdot \text{cm}^{-1}$ .

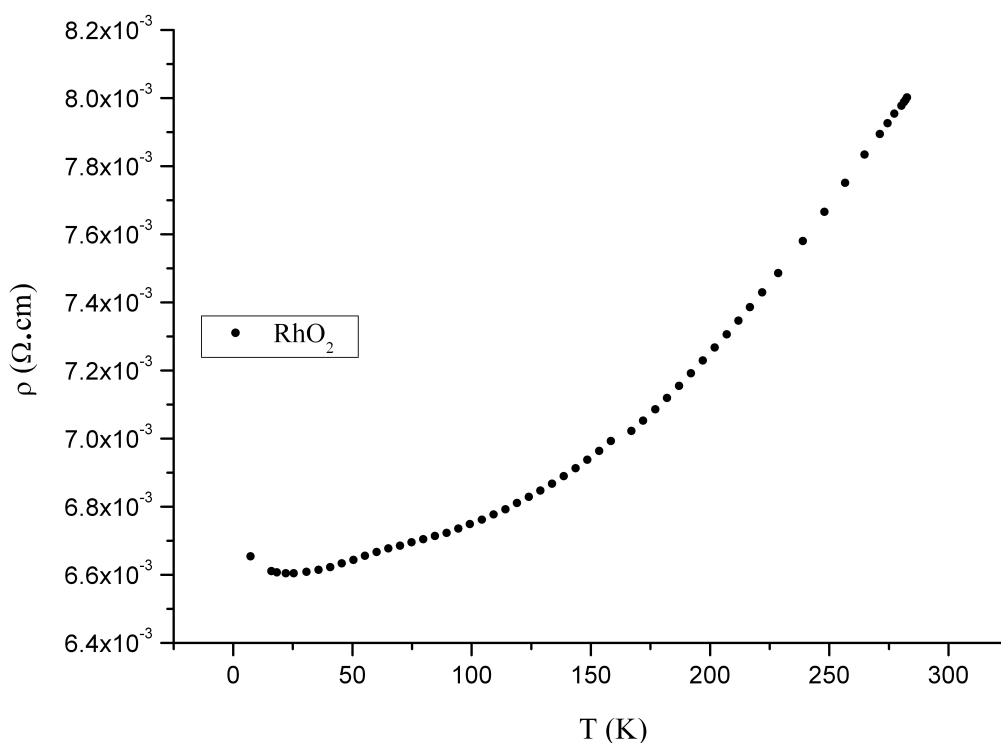


**Figure 4.1.10.** Temperature dependence of the specific resistivity of  $\text{RhO}_2$ .

### **$\text{Li}_2\text{RhO}_3$**

#### *Thermal Stability*

The thermal stability was investigated using simultaneous differential thermal analysis (DTA) and thermogravimetry experiments (TG) in argon atmosphere. The compound is stable up to 1300 K (Figure 4.1.11). Above this temperature the sample starts to decompose. In a second experiment, the sample was heated up to 1350 K and held at that temperature for 3 h. The

experimental weight loss of 19 % is in good agreement with that calculated for the loss of one oxygen molecule per formula unit. According to the thermal stability of the individual metal oxides ( $\text{Li}_2\text{O}$  up to 1843 K,  $\text{RhO}_2$  up to 1323 K), and the measured weight loss, an appropriate decomposition reaction could be expressed as follows:  $\text{Li}_2\text{RhO}_3 \rightarrow \text{Li}_2\text{O} + \text{RhO}_2 \rightarrow \text{Li}_2\text{O} + \text{Rh} + \text{O}_2$ . In the DTA experiments, no phase transition was observed in the temperature region from 298 to 1623 K.

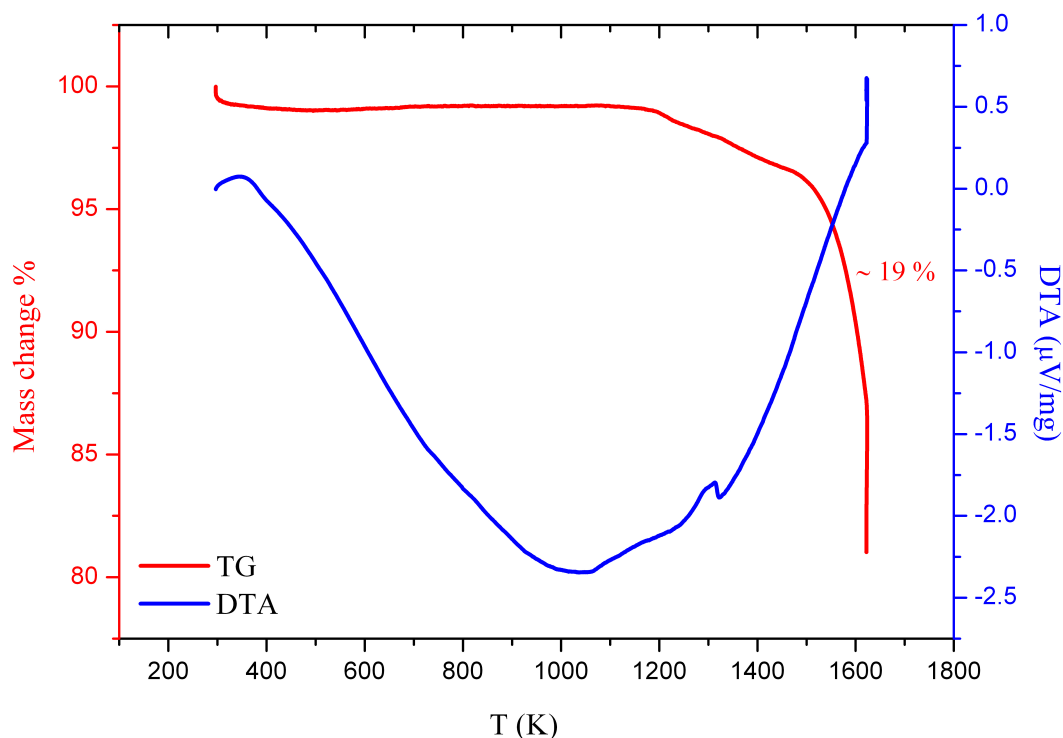
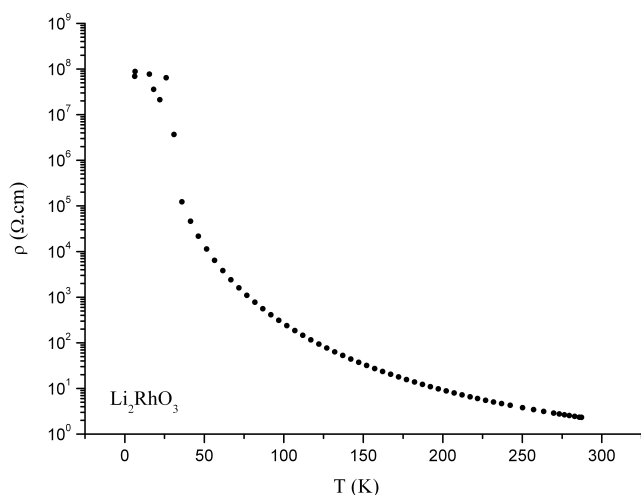


**Figure 4.1.11.** Thermal stability of  $\text{Li}_2\text{RhO}_3$ .

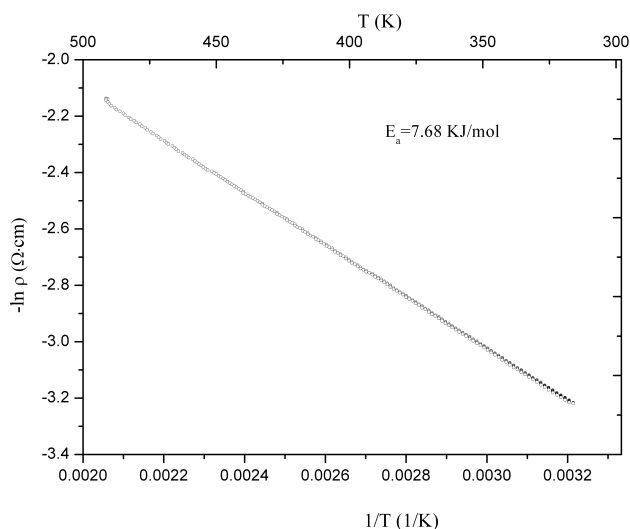
### *Impedance Spectroscopy*

Conductivity measurements using ion blocking electrodes showed  $\text{Li}_2\text{RhO}_3$  to be a predominantly electronic conductor. When applying direct current conditions, no current drop was perceivable, even during long term measurements. The temperature characteristic of the resistivity indicates semiconducting behavior with activation energy of  $7.68 \text{ kJ mol}^{-1}$  (Figure 4.1.12a) and Figure 4.1.12b)). According to impedance spectroscopy, the specific conductivity

increases from  $0.04 \Omega^{-1}\cdot\text{cm}^{-1}$  at room temperature to  $0.12 \Omega^{-1}\cdot\text{cm}^{-1}$  at 473 K, which is one order of magnitude higher than reported for other compounds of  $\text{Li}_2\text{MO}_3$ -type. The conductivity can be further examined through the dependence between the frequency and the specific resistivity. It was shown that the conductivity is frequency independent in the whole region from 1 to 10 MHz and at temperatures from 300 to 500 K. In general, there exists scarce literature data on the physical properties of the known compounds belonging to this structural family. For  $\text{Li}_2\text{IrO}_3$  metallic conductivity with little temperature dependence is reported<sup>95</sup>, and for  $\text{Li}_2\text{PtO}_3$  recent values, twice as high as previously reported, have led to certain confusion and discrepancy<sup>96, 116</sup>.



a)



b)

**Figure 4.1.12.** Temperature dependence of **a)** specific resistivity **b)** logarithm of the specific conductivity for  $\text{Li}_2\text{RhO}_3$ .

### Seebeck coefficient

The temperature dependence of the Seebeck coefficient is shown on Figure 4.1.13. The sign of the Seebeck coefficient is negative, indicating an n-type conductor. The value of that coefficient for room temperature is  $-20 \mu\text{V}\cdot\text{K}^{-1}$ . From 80 to 150 K the values decrease linear, above that temperature it is steel linear but starts to increase indicating change in the conducting mechanism. The Seebeck coefficient for a highly degenerate electron gas, predicting such behavior<sup>117</sup>, is given by the formula:

$$\alpha = 86.2 * (r + 1) * \frac{\pi^2}{3} * \left(\frac{k_B * T}{E_F}\right) \quad (4.1.5)$$

Where  $r = 1$  for a ionic lattice,  $k_B$  – Boltzmann constant,  $T$  – absolute temperature,  $E_F$  – Fermi energy. This experimental result indicates the existence of collective carriers, although the temperature dependence of the resistivity shows a semiconducting but not metallic behavior.

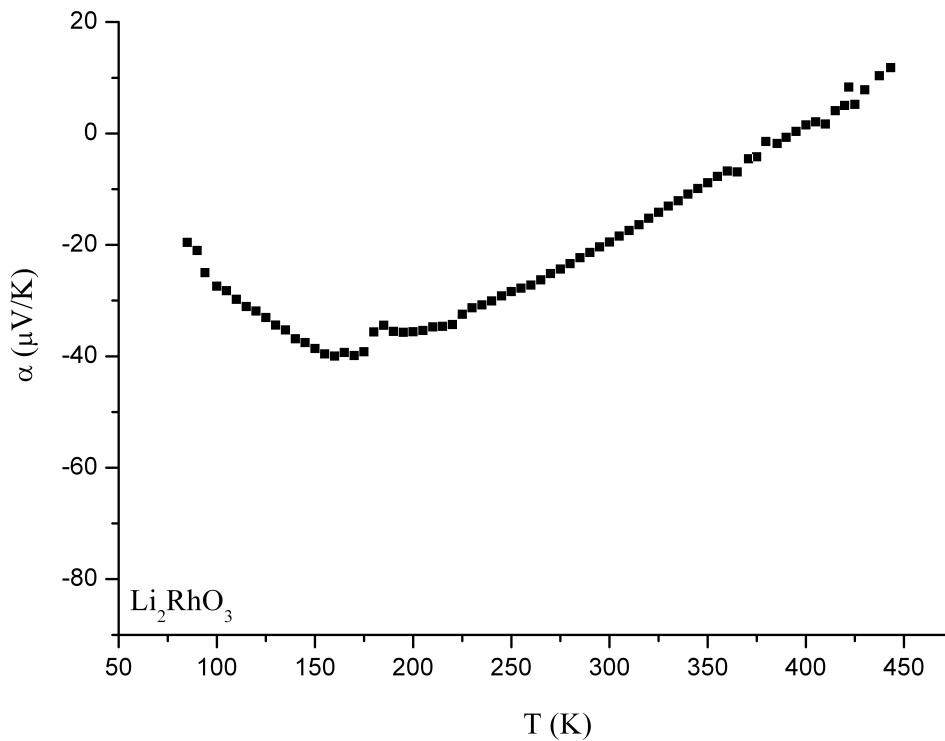


**Figure 4.1.13.** Temperature dependence of Seebeck coefficient of  $\text{Li}_2\text{RhO}_3$ .

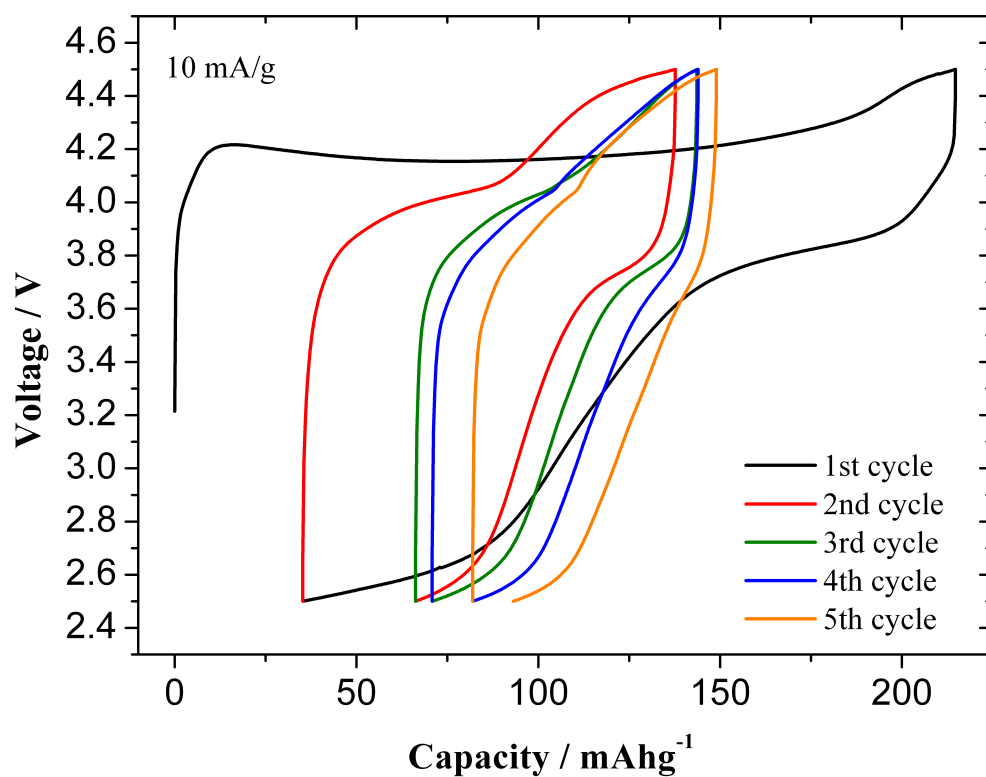
Combining the data of electronic conductivity and this one from Seebeck coefficient one could calculate the thermoelectric power factor, and if there is thermal conductivity data even the *figure of merit*  $ZT$ , for thermal-electrical power generation. The thermoelectric power factor ( $\tau_p$ ) is given by the equation:

$$\tau_p = \alpha^2 * \sigma \quad (4.1.6)$$

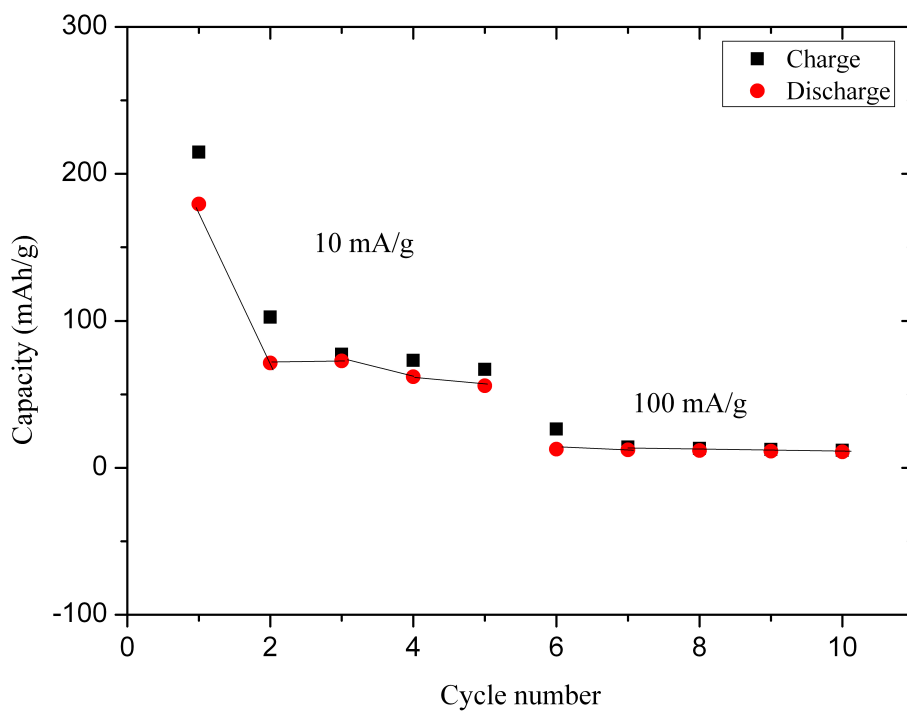
Where  $\sigma$  is the conductivity and  $\alpha$  Seebeck coefficient. The  $\tau_p$  for room temperature equal  $1.07 \cdot 10^{-4} \text{ W} \cdot \text{m}^{-1} \cdot \text{K}^{-2}$  ( $\alpha = -20 \text{ } \mu\text{V} \cdot \text{K}^{-1}$   $\sigma = 3.99 \cdot 10^{-3} \text{ } \Omega^{-1} \cdot \text{cm}^{-1}$ ), which is a quite good value and the material could be consider as a promising n-type thermoelectric material<sup>78</sup>.

### *Electrochemical Properties*

The lithium insertion and deintercalation of the  $\text{Li}/\text{Li}_2\text{RhO}_3$  couple was examined in the potential range between 2.5 and 4.5 V with specific currents of 10 mA/g and 100 mA/g. Figure 4.1.14 a) shows five charge - discharge cycles. In the first cycle, charge capacities of around 200 mAh/g were achieved. However, already the first discharge cycle shows that there is a large irreversible capacity. The charge curve indicates that the electrochemical kinetics is sluggish. Possibly, the large crystallite size prevents efficient Li diffusion, and gives rise to huge concentration polarisation. The following cycles 2 - 5 show higher columbic efficiencies (discharge divided by charge capacity), but only give capacities in the order of 70 %. An existence of a plateau in the charge/discharge curve is an indication for the coexistence of two phases in the electrode material. Two plateaus can be identified. Very likely there is a  $\text{Rh}^{4+}/\text{Rh}^{3+}$  couple at 4.1 V vs  $\text{Li}/\text{Li}^+$  (equivalent to 1.0 V vs. SHE) and a  $\text{Rh}^{3+}/\text{Rh}^{2+}$  couple at 4.5 V (equivalent to 1.5 vs. SHE) The dependence of material capacity on the number of the cycles (Figure 4.1.14 b) shows a rather poor rate performance compared to the widely used  $\text{LiCoO}_2$ <sup>118, 119</sup>. On the other hand, if the electrochemical behavior is compared to  $\text{Li}_2\text{IrO}_3$ <sup>95</sup> or  $\text{Li}_2\text{RuO}_3$ <sup>120</sup>,  $\text{Li}_2\text{RhO}_3$  is clearly showing better performance.



a)



b)

**Figure 4.1.14 a).** The charge - discharge curves of Li/Li<sub>2</sub>RhO<sub>3</sub> as a function of capacity. **b)** The capacity as a function of the cycle number.

## Magnetic Susceptibility

$\text{Li}_2\text{RhO}_3$  is paramagnetic and its magnetic behavior follows the Curie-Weiss law at temperatures above 150 K. The magnetic susceptibility was scanned as a function of temperature for different magnetic fields. The dependence of the inverse molar susceptibility on temperature is plotted in Figure 4. The linear fit of the temperature region from 150 to 330 K yields a magnetic moment of  $2.04 \mu_B$ . The effective magnetic moment  $\mu_{\text{eff}}$  saturates while approximating  $1.97 \mu_B$  at 300 K (Figure 4.1.15). The ideal value for the low-spin state of  $\text{Rh}^{4+}$  ( $S = 1/2$ ), considering a spin-only contribution to the magnetic moment, would be  $1.73 \mu_B$ , whereas the obtained one is substantially higher indicating some orbital contribution. However, this is still comparable with other known  $d^5$  systems ( $\text{Rh}^{4+}$ <sup>121, 122</sup>, and  $\text{Ir}^{4+}$ <sup>123</sup>. Kobayashi et al.<sup>95</sup> found  $1.82 \mu_B$  for  $\text{Ir}^{4+}$ , and James and Goodenough<sup>92</sup> reported  $1.83 \mu_B$  for  $\text{Ru}^{4+}$  ( $d^4$ ). The magnetic moments of alkali metal fluororhodates<sup>123</sup> lie normally in the range of 1.95 to  $2.01 \mu_B$ , and for the chloro-complexes<sup>123</sup> around  $1.7 \mu_B$ .

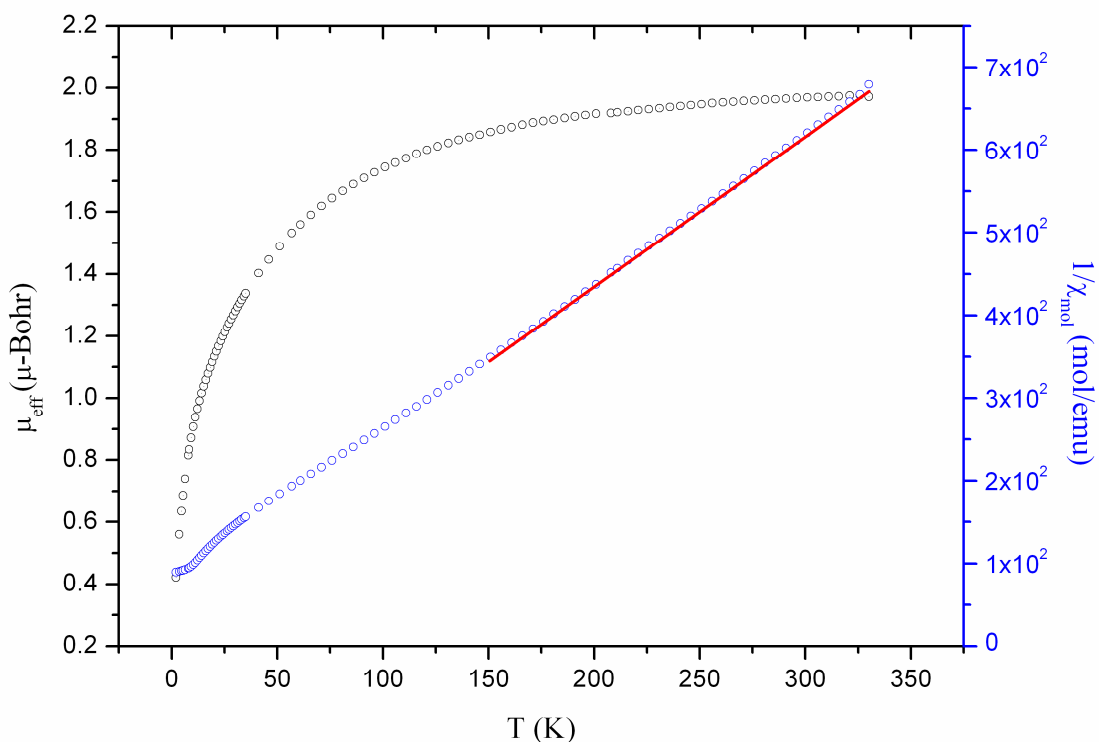


**Figure 4.1.15.** Inverse molar susceptibility and the effective magnetic moment as function of temperature for  $\text{Li}_2\text{RhO}_3$ .

## 4.1.2. System Ag – Co – O

Two modifications,  $3R^{85}$  and  $2H^{84}$ , of  $AgCoO_2$  are known, whereas the second one was published during ongoing research in that work.

### 4.1.2.1. Synthesis of $AgCoO_2$

Different approaches for the synthesis of this delafossite were applied. 1 M solution of  $AgNO_3$  (Roth, 99%) and  $Co(NO_3)_3 \cdot 5H_2O$  was mixed in 1:1 ratio, homogenized and precipitated with 5 M KOH solution in a teflon container. The reaction vessel was placed in a sand bath, heated with 20 K/min up to 473 K and held for 48 h before cooling down to room temperature. At the end of the reaction the powder was washed with distilled water and dried in a dryer at 393 K. The obtained black powder shows a high degree of crystallinity as it could be seen in Figure 4.1.16.

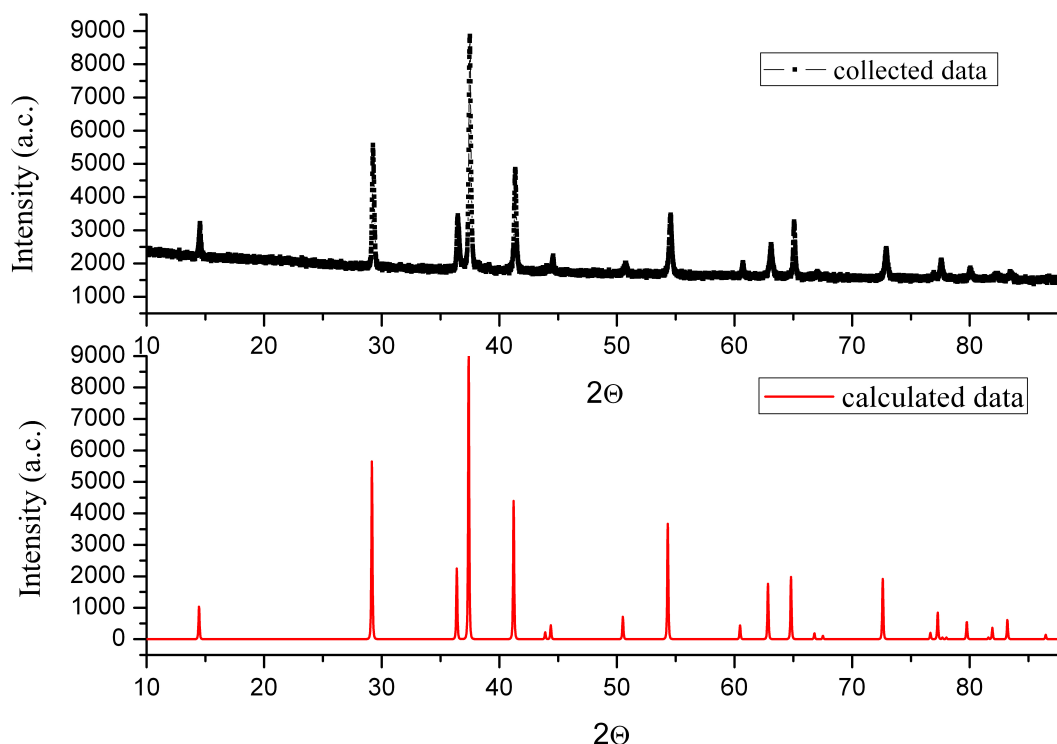
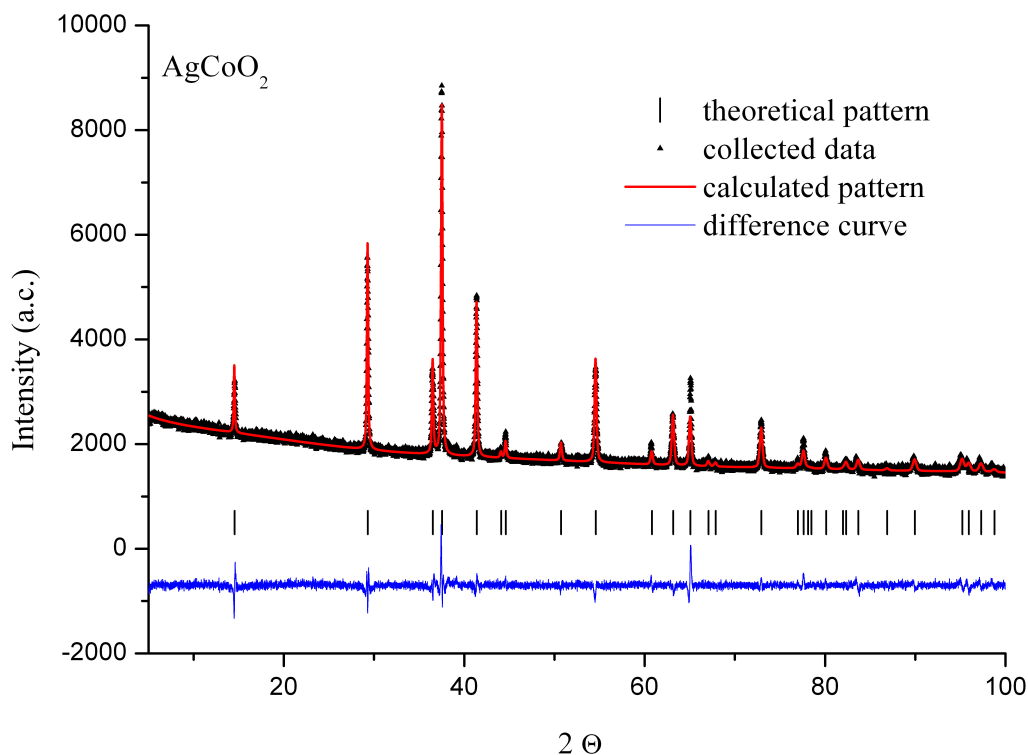


Figure 4.1.16. Powder pattern of measured and calculated  $3R$  -  $AgCoO_2$  ( $R\bar{3}m$ ).



#### 4.1.2.2. Structural characterization of AgCoO<sub>2</sub>

AgCoO<sub>2</sub> crystallizes in the 3R-delafoosite structure type. The structural solution was obtained by applying the Rietveld method. The structure parameters are summarized in Table 4.1.6 and Table 4.1.7 and the fit is shown in Figure 4.1.17. The refined cell parameters  $a = 2.8642(1) \text{ \AA}$  and  $c = 18.2641(7) \text{ \AA}$  match best with the reported from Stahlin and Oswald<sup>37</sup> as well as those from Shannon et al.<sup>38</sup> and Emos and Berger<sup>85</sup>. The Co<sup>3+</sup> cations are coordinated by 6 oxygen atoms (Co – O distance equal to  $1.908(2) \text{ \AA}$ ), forming trigonally distorted edge shared octahedra, which build two dimensional layers. The silver atoms are linearly coordinated by 2 oxygen atoms, parallel to the  $c$ -axes with bond lengths of  $2.091(4) \text{ \AA}$ . The Co – O distance as well as Ag – O distance are as expected<sup>40, 46, 106</sup>.



**Figure 4.1.17.** Observed (black), calculated (red) and difference (blue) tracks of X-ray powder diffraction for AgCoO<sub>2</sub>. Tick marks represent the calculated peak positions.

Table 4.1.6. Atomic positions of AgCoO<sub>2</sub>

Atom	Wyckoff Positions	<i>x</i>	<i>y</i>	<i>z</i>	Occ.
Ag	3 <i>a</i>	0	0	0	1
Co	3 <i>b</i>	0	0	0.5	1
O	6 <i>c</i>	0	0	0.1145(2)	1

Table 4.1.7. Crystallographic and refinement details for AgCoO<sub>2</sub> refined by the Rietveld method.

<b>Space Group</b>	$R\bar{3}m$
<i>a</i> / Å	2.8642(1)
<i>c</i> / Å	18.2641(7)
<i>V</i> / Å <sup>3</sup>	129.76(1)
<i>Z</i>	3
Calc. density (g cm <sup>-3</sup> )	7.63 (1)
<i>R</i> <sub>exp</sub> (%) <sup>*</sup>	2.34
<i>R</i> <sub>p</sub> (%) <sup>*</sup>	2.24
<i>R</i> <sub>wp</sub> (%) <sup>*</sup>	3.19
<i>gof</i> <sup>*</sup>	1.36
<i>R</i> ( <i>F</i> <sup>2</sup> ) (%) <sup>*</sup>	2.16
Scan time	20 h
No. of variables	24

### 4.1.2.3. Physical characterization of AgCoO<sub>2</sub>

#### *Thermal Stability*

The thermal stability was investigated using simultaneous differential thermal analysis (DTA) and thermogravimetry experiments (TG) in argon atmosphere. Up to 770 K the compound is stable afterwards it decomposes with formation of Ag<sub>2</sub>O and Co<sub>2</sub>O<sub>3</sub>. The mass lost of 4.26 % could be assigned to the decomposition of Ag<sub>2</sub>O (theoretically 4.02 w %). Above 1000 K two phase transition peaks one exo- and one endothermic can be recognized on the DTA curve. The exothermic signal matches with an additional weight loss of 2.31 %, which could be explained with reduction of Co<sub>2</sub>O<sub>3</sub> to Co<sub>3</sub>O<sub>4</sub> (theoretically 2.66 %). The origin of the endothermic peak is the melting point of elementary silver.

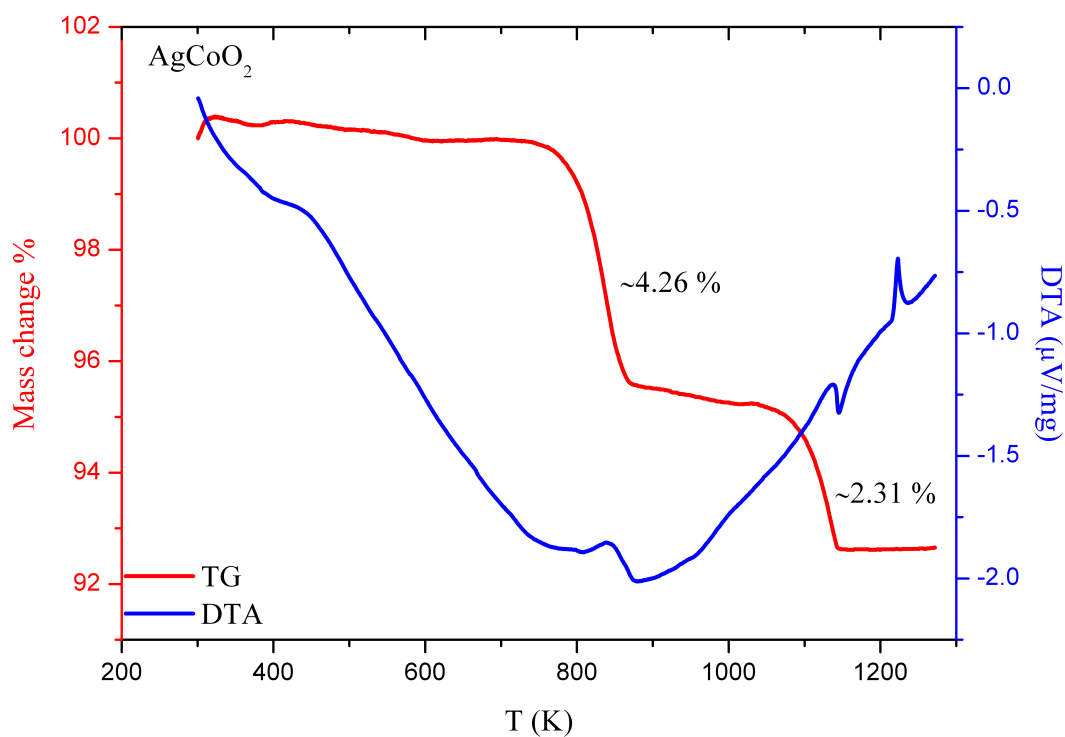


**Figure 4.1.18.** Thermal stability of AgCoO<sub>2</sub>.

### Electrical Conductivity

The specific resistivity of a powder sample was measured in the temperature range from 3 to 300 K. The powder was finely ground and pressed (0.69 GPa) in a pellet with 6 mm diameter and 1.2 mm thickness. The contacting wires were bonded with special silver glue. In the temperature range 3 to 150 K the specific resistivity of the sample reaches almost the sensitivity limits of the machine ( $10^8 \Omega$ ) afterwards it drops to  $4.47 \text{ k}\Omega\cdot\text{cm}$  at room temperature (conductivity of  $2.23\cdot 10^{-4} \text{ S}\cdot\text{cm}^{-1}$ ). The activation energy, calculated in the temperature range from 200 to 300 K, is equal to  $30.99 \text{ kJ}\cdot\text{mol}^{-1}$ .

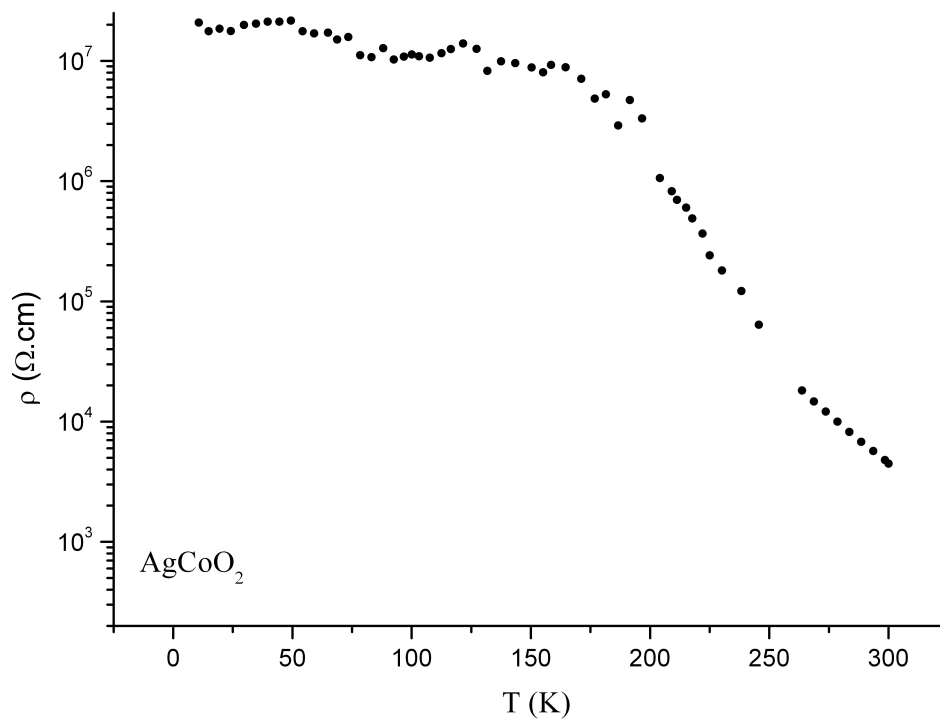


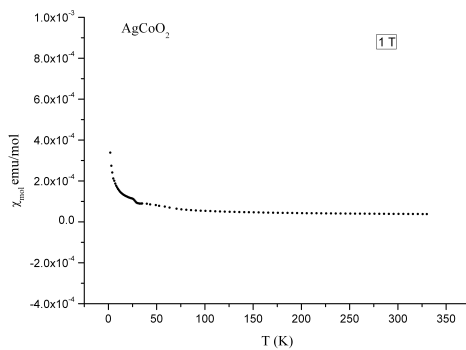
**Figure 4.1.19.** Temperature dependence of the specific resistivity of  $\text{AgCoO}_2$ .

### Magnetic Susceptibility

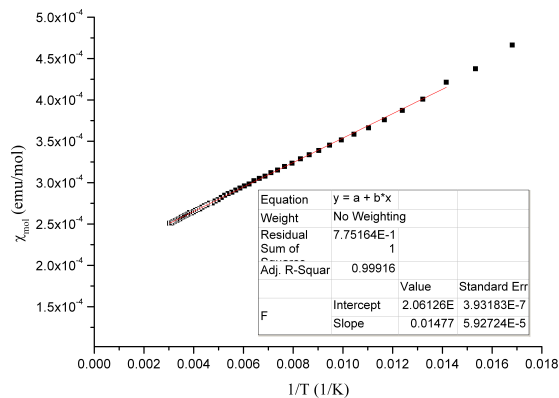
In  $\text{AgCoO}_2$ , the Co has a  $d^6$  configuration and in the octahedral ligand field is expected to be diamagnetic, if low-spin complex is realised or paramagnetic with  $\mu_{\text{eff}} = 4.9 \mu_{\text{B}}$  in high-spin complexes. The susceptibility shows temperature dependence, in the region from 3 to around

25 K. That magnetic behavior is well described by the sum  $\chi_0$  (mostly due to orbital contribution) and the Curie term (C/T) (see equation 4.1.7). Analogous curves are reported in the case of NaCoO<sub>2</sub> and AgCoO<sub>2</sub><sup>46</sup>. The paramagnetic part at very low temperature could be reason of the strong orbital contribution or consequence of the deformed geometry of the Co octahedra. The percentage of the Curie impurity as well as the temperature independent term was calculated for the three fields of 1, 3 and 7 Tesla. The temperature independent paramagnetism (TIP) was found to be  $2.641 \cdot 10^{-5} \text{ cm}^3 \cdot \text{mol}^{-1}$ , whereas the Curie impurities were estimated to 3.9 %, of S=1/2, species and 0.79 % of S=3/2 species, these numbers are in a good correlation with reported<sup>84, 124</sup>.

a)



$$\chi_{mol} = \frac{C_{imp}}{T} + \chi_0 \quad (4.1.7)$$



b)

**Figure 4.1.19.** a) The magnetisation as a function of temperature; b) The molar susceptibility as function of reverse temperature to determine the amount of the impurities of AgCoO<sub>2</sub>.

### 4.1.3. Systems Ag – Rh – O and Ag – Li – Rh – O

#### 4.1.3.1. Synthesis of $\text{AgRhO}_2$ and $\text{Ag}(\text{Li}_{1/3}\text{Rh}_{2/3})\text{O}_2$

##### $\text{AgRhO}_2$

For the synthesis of  $\text{AgRhO}_2$ ,  $\text{LiRhO}_2$  was treated with an excess of molten mixture of  $\text{AgNO}_3$  (Roth, 99%) /  $\text{KNO}_3$  (Merk 99.9%) in a ratio of 2:1. That reaction was performed in a sealed glass tube under Ar at 623 K for 350 hours. For the synthesis of  $\text{LiRhO}_2$  stoichiometric amounts of  $\text{Rh}_2\text{O}_3$  (Alfa Aesar, 99.9%) and  $\text{LiOH}$  (Alfa Aesar, anhydrous 99.9%) were mixed and heated in oxygen flow at 1123 K, held for 48 h and cooled by room temperature.

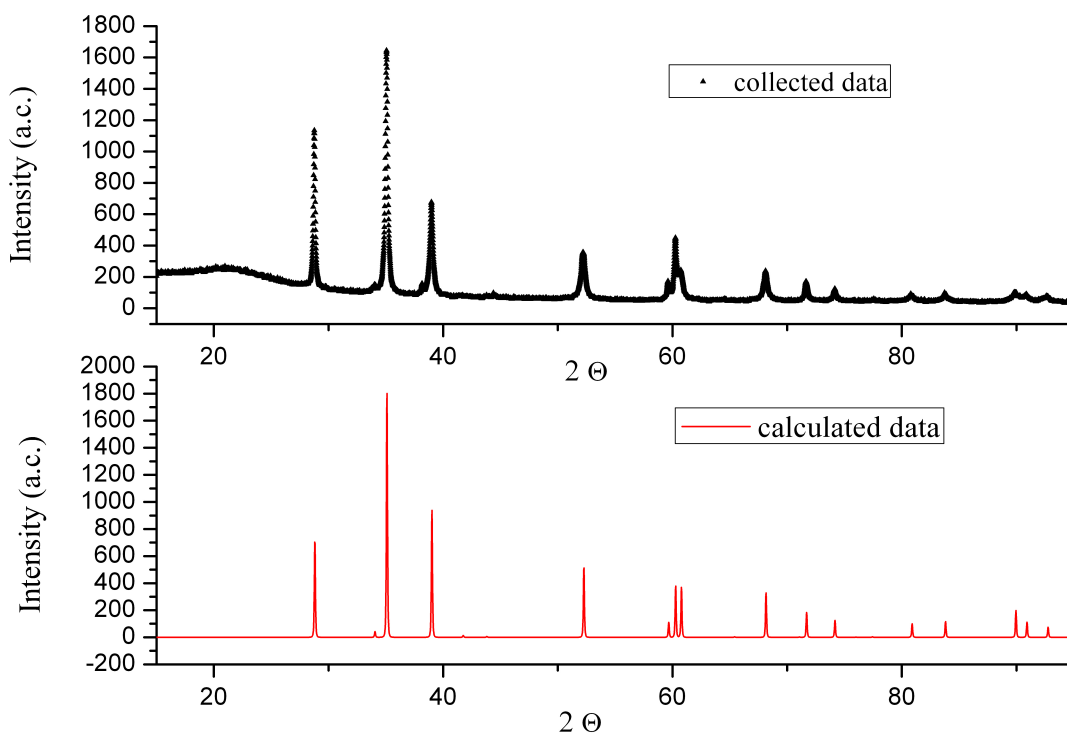


**Figure 4.1.20.** Powder pattern of measured and calculated  $\text{AgRhO}_2$  ( $R\bar{3}m$ ) The theoretical pattern are calculated on base of reported cell parameters of  $\text{AgRhO}_2$  from Shannon et. all<sup>38</sup>.

## **Ag(Li<sub>1/3</sub>Rh<sub>2/3</sub>)O<sub>2</sub>**

For the synthesis of AgLi<sub>1/3</sub>Rh<sub>2/3</sub>O<sub>2</sub>, Li<sub>2</sub>RhO<sub>3</sub> was treated with an excess of molten mixture of AgNO<sub>3</sub> (Roth, 99%) / KNO<sub>3</sub> (Merk 99.9%) in a ratio of 2:1. This reaction was performed in a sealed glass tube under Ar at 623 K for 350 hours. Li<sub>2</sub>RhO<sub>3</sub> was prepared by reacting stoichiometric mixtures of RhO<sub>2</sub> and LiOH (Alfa Aesar, anhydrous, 99.9 %). The mixture was carefully ground and heated in a corundum crucible at 1123 K in an oxygen flow for 48 h. RhO<sub>2</sub> was synthesized using high pressure oxygen autoclaves, starting from Rh(NO<sub>3</sub>)<sub>3</sub>·xH<sub>2</sub>O (ChemPur, 36% Rh), which was decomposed in air at 473 K. The obtained amorphous residue was treated at 50-70 MPa oxygen pressure and at a temperature of 723 K, for 60 h.

### **4.1.3.2. Structural characterization AgRhO<sub>2</sub> and Ag(Li<sub>1/3</sub>Rh<sub>2/3</sub>)O<sub>2</sub>**

#### **AgRhO<sub>2</sub>**

AgRhO<sub>2</sub> crystallizes in the 3R-delafoosite type of structure. Analogous to cobalt in AgCoO<sub>2</sub> the Rh<sup>3+</sup> cations are coordinated by 6 oxygen atoms (Rh – O distance equal to 2.076(2) Å), forming trigonally distorted edge shared octahedra. The silver atoms are linearly coordinated by 2 oxygen atoms. These dumbbells with Ag – O bond lengths of 2.0168(5) Å lie parallel to the *c*-axes. All bond lengths and distances are as expected. The refined cell parameters of *a* = 3.06882(5) Å and *c* = 18.59067(4) Å are in a good agreement with the reported one<sup>38</sup>. Summarized structural data are given in Table 4.1.6 and Table 4.1.7, and the Rietveld refinement is shown on Figure 4.1.21.

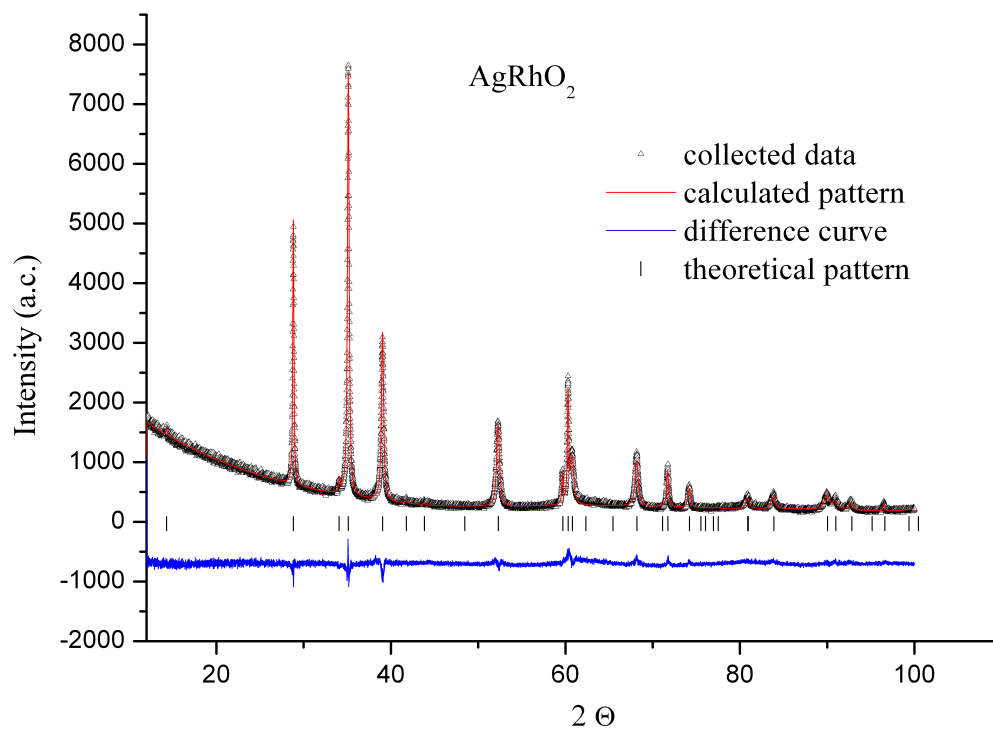


**Figure 4.1.21.** Observed (black), calculated (red) and difference (blue) tracks of X-ray powder diffraction for  $\text{AgRhO}_2$ . Tick marks represent the calculated peak positions.

Table 4.1.8. Atomic positions of  $\text{AgRhO}_2$

Atom	Wyckoff Positions	$x$	$y$	$z$	occ.
Ag	$3a$	0	0	0	1
Rh	$3b$	0	0	0.5	1
O	$6c$	0	0	0.1084(2)	1



Table 4.1.9. Crystallographic and refinement details for AgRhO<sub>2</sub> refined by the Rietveld method.

Space group	$R\bar{3}m$ (166)
$a / \text{\AA}$	3.06882(5)
$c / \text{\AA}$	18.59067 (4)
$V / \text{\AA}^3$	151.624(6)
$Z$	3
Calc. density (g cm <sup>-3</sup> )	7.9763(3)
$R_{\text{exp}}$ (%) <sup>*</sup>	4.35
$R_p$ (%) <sup>*</sup>	4.76
$R_{\text{wp}}$ (%) <sup>*</sup>	6.46
$gof$ <sup>*</sup>	1.48
$R(F^2)$ (%) <sup>*</sup>	3.36
Scan time	40 h
No. of variables	24

### Ag(Li<sub>1/3</sub>Rh<sub>2/3</sub>)O<sub>2</sub>

The new quaternary delafossites Ag(Li<sub>1/3</sub>Rh<sub>2/3</sub>)O<sub>2</sub> and Ag(Li<sub>1/3</sub>Ir<sub>2/3</sub>)O<sub>2</sub> display average structures which are analogues to the 3R delafossite polytype. Analysis of the real structures, based on X-ray powder- and electron diffraction data have revealed a specific kind of stacking faults to be present. The disorder can be conclusively rationalized by tracing the formation of the new quaternary delafossite from the respective rock salt type variants Li<sub>2</sub>MO<sub>3</sub> mechanistically. The most striking topological change along this process is related to the stacking sequence of the oxygen atoms in the respective structure families. While in a rock salt variant a stacking sequence corresponding to the cubic close packing, ---ABCA---, is realized, the 3 R - delafossites follow the pattern ---AABBCCAA---. Thus the transfer affords shifting

the oxygen layers, or OMO, respectively by either of the vectors of  $1/3\ 2/3\ 0$ ,  $1/3\ 1/3\ 0$  or  $1/3\ -2/3\ 0$ . Since these moves are energetically equivalent, they will occur with equal probability, and a defect structure with random stacking sequence results (space group  $P3_112/P3_212$ ) as described are below. Healing of the stacking faults may lead to a fully ordered ground state structure, passing partially ordered stages in space groups  $C2/m$  or  $C2/c$ .

#### *Structural solution using HRTEM and DIFFAX simulation*

The XRPD patterns of  $\text{AgLi}_{1/3}\text{Ir}_{2/3}\text{O}_2$  and  $\text{AgLi}_{1/3}\text{Rh}_{2/3}\text{O}_2$  as well of  $\text{AgRhO}_2$  (Figure 4.1.39, Figure 4.1.22 and Figure 4.1.21) are very similar, and can be interpreted in terms of a delafossite - type structure. Rietveld refinements were performed with a corresponding structure model, allowing for a common isotropic atomic displacement parameter for all atoms and allowing for anisotropic microstrain broadening<sup>125, 126</sup>, acknowledging in particular for  $\text{AgLi}_{1/3}\text{Ir}_{2/3}\text{O}_2$  and  $\text{AgLi}_{1/3}\text{Rh}_{2/3}\text{O}_2$  the relatively broad reflections with a large  $hk$  contribution (the  $00l$  reflections are quite narrow) and for  $\text{AgRhO}_2$  of such reflections with simultaneously large  $hk$  and  $l$  components ( $hk0$  and  $00l$  reflections are relatively narrow). For  $\text{AgLi}_{1/3}\text{Ir}_{2/3}\text{O}_2$  and  $\text{AgLi}_{1/3}\text{Rh}_{2/3}\text{O}_2$  a mixed occupation of the octahedral  $M$  metal sites by Rh and Li was additionally considered by refining the corresponding occupancies, keeping the sum of occupancies of both species to 1. The details of the measurements and the refinements are listed in Tables 4.1.7, 4.1.9, 4.1.13 and the refined fractional coordinates, occupancies; atomic displacement parameters are listed in Tables 4.1.8, 4.1.10, 4.1.12. Selected characteristic interatomic distances are listed in Table 4.1.14.

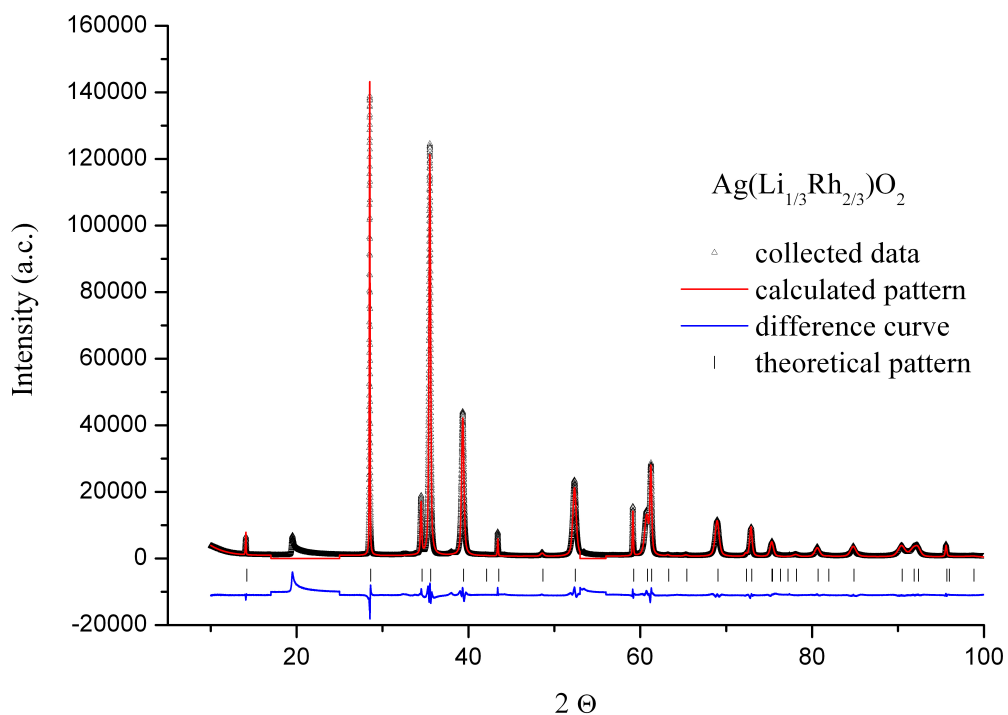


**Figure 4.1.22.** Observed (black), calculated (red) and difference (blue) tracks of X-ray powder diffraction for  $\text{Ag}(\text{Li}_{1/3}\text{Rh}_{2/3})\text{O}_2$ . Tick marks represent the calculated peak positions. The Rietveld refinement is performed in an average delafossite structure 3R.

Table 4.1.10. Atomic positions of  $\text{Ag}(\text{Li}_{1/3}\text{Rh}_{2/3})\text{O}_2$

Atom	Wyckoff Positions	$x$	$y$	$z$	Occ.
Ag	$3a$	0	0	0	1
Li	$3b$	0	0	0.5	0.2803(6)
Rh	$3b$	0	0	0.5	0.7197(6)
O	$6c$	0	0	0.10991(7)	1

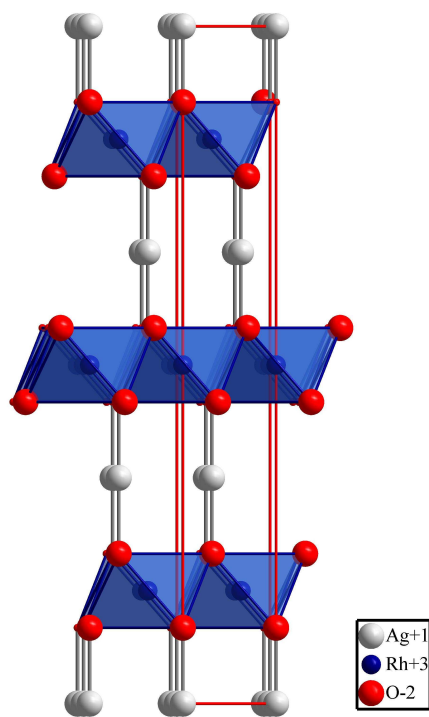
Table 4.1.11. Crystallographic and refinement details for  $\text{Ag}(\text{Li}_{1/3}\text{Rh}_{2/3})\text{O}_2$  refined by the Rietveld method.

Space group	$R\bar{3}m$ ( <b>166</b> )
$a / \text{\AA}$	3.02085(1)
$c / \text{\AA}$	18.70306(0)
$V / \text{\AA}^3$	147.808(1)
$Z$	3
Calc. density ( $\text{g cm}^{-3}$ )	7.275(1)
$R_{\text{exp}} (\%)^*$	2.00
$R_{\text{p}} (\%)^*$	5.72
$R_{\text{wp}} (\%)^*$	7.97
$\text{gof}^*$	3.97
$R(F^2) (\%)^*$	1.96
Scan time	40 h
No. of variables	28

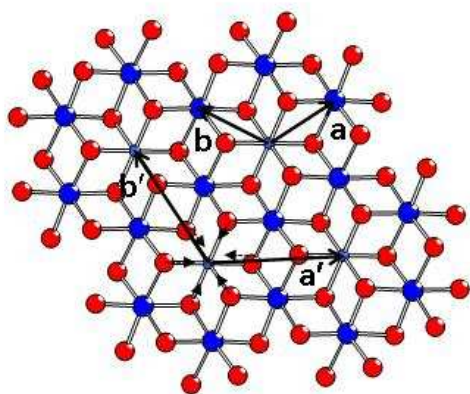
However, the patterns of  $\text{AgLi}_{1/3}\text{Ir}_{2/3}\text{O}_2$  and  $\text{AgLi}_{1/3}\text{Rh}_{2/3}\text{O}_2$  show some additional “features”, in particular a quite asymmetric “reflection” at a diffraction angle of about  $2\theta = 19.5^\circ$  (not present for  $\text{AgRhO}_2$ ), which cannot be explained by the applied “usual” delafossite-type structure models with lattice parameters  $a$  and  $c$ . Strikingly, two of such “reflections” can be indexed with the non-integer indices  $\frac{1}{3}\frac{1}{3}0$  ( $19.5^\circ$ ) and  $\frac{4}{3}\frac{1}{3}0$  ( $53.5^\circ$ ), which would suggest a hexagonal/trigonal superstructure with  $a' = b' = 3^{1/2}a$ . However, the shape of these reflections (well visible for the  $2\theta = 19.5^\circ$  “reflection”) with a steep drop of the intensity at the low-angle side (Figure 4.1.22) is typical for what is occasionally called *Warren peaks*<sup>127</sup>, frequently observed for layer-faulted structures. These Warren peaks originate from rods of diffuse scattering occurring in reciprocal space perpendicular to the faulting plane. If such a rod does not intersect the origin of the reciprocal space, the pertaining diffuse scattering will show a maximum in a powder-diffraction pattern at such a diffraction angle, which corresponds to a  $1/d$  value representing the minimum distance of the rod to the origin of the reciprocal space. This occurs even if the intensity on that rod in reciprocal space does not show a maximum at

that minimum-distance point. Starting from high reflection angles the intensity will rise until a specific cut-off angle is approached, at which the intensity contribution pertaining to that rod will drop to zero. The above-mentioned indexing of the Warren peaks suggests that the rods of diffuse scattering occur at  $hkl$  with  $h = (3n \pm 1)/3$ ,  $k = (3n \pm 1)/3$  (with integer  $n$ ,  $m$ ) and arbitrary  $l$  (given with respect to the original delafossite unit cell).

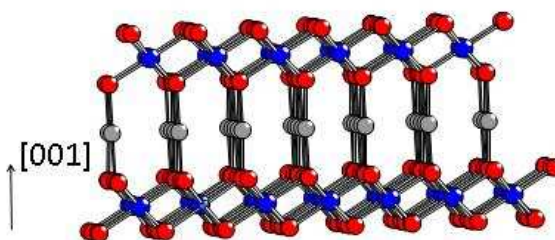
For the case of the present materials a faulted structure model, which would explain occurrence of these Warren peaks, can be obtained assuming that the  $2/3 M^{4+}$  ( $M = \text{Rh}, \text{Ir}$ ) and  $1/3 \text{Li}^+$  are occupying the octahedral sites. The most straightforward way to distribute these atoms within one layer  $[(\text{Ir,Rh})_2\text{LiO}_6]^{3-}$  is to follow a honeycomb-like ordering pattern, which leads to a two-dimensional  $a' = b' = 3^{1/2}a$  superstructure for the  $M$  atoms (Figure 4.1.23 b).



a)



b)



c)

**Figure 4.1.23.** a) Average delafossite structure 3R ( $R\bar{3}m$ ) view along [010], with  $M = \text{Rh}$  showing the  $\text{RhO}_6$  octahedra; b) one honeycomb-like ordered  $[\text{M}_2\text{LiO}_6]^{3-}$  layer ( $M = \text{Rh}, \text{Ir}$ ) together with the lattice basis vectors  $\mathbf{a}$ ,  $\mathbf{b}$ ,  $\mathbf{a}'$  and  $\mathbf{b}'$  (see text) as well as distortion in the oxygen partial structure indicated by dashed arrows as occurring around one Li atom c) stacking of two layers with Ag in between.

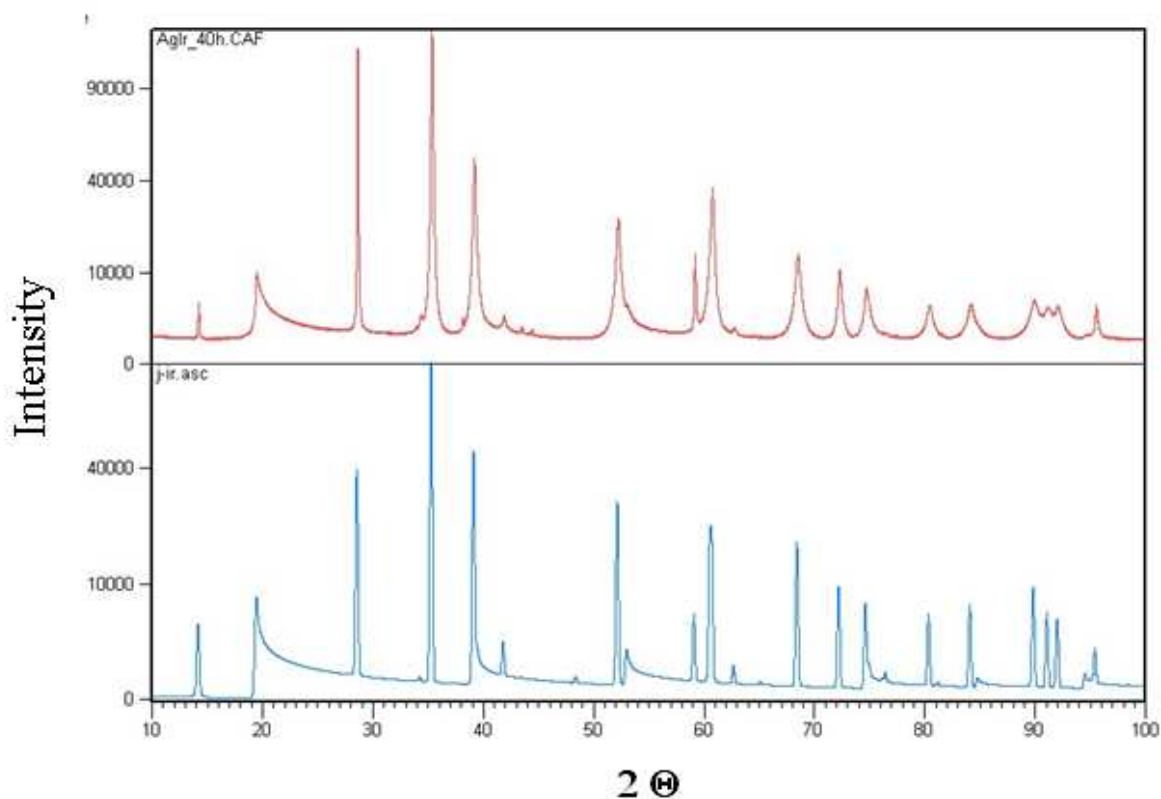


**Figure 4.1.24:** Comparison of the measured XRPD pattern of  $\text{Ag}(\text{Li}_{1/3}\text{Ir}_{2/3})\text{O}_2$  (top) with a pattern simulated using DIFFAX<sup>128</sup> assuming a random stacking sequence of two-dimensional honeycomb-like ordered  $[\text{M}_2\text{LiO}_6]^{3-}$  layers (M = Rh, Ir see Figure 4.1.23).

Since apparently no superstructure reflections can be discerned in the XRPD pattern, one may assume as a first approximation that these ordered  $[(\text{Ir,Rh})_2\text{LiO}_6]^{3-}$  layers are stacked within the framework of the delafossite structure in a completely random fashion. XRPD patterns corresponding to such random stacks were simulated using the DIFFAX software and show good agreement with the experimental patterns, in particular with respect to the Warren peaks<sup>128</sup> (Figure 4.1.24). For the structural model underlying the calculated diffractogram we have assumed that for a given  $[(\text{Ir,Rh})_2\text{LiO}_6]^{3-}$  the following layer of this type is shifted by either  $(\mathbf{a} + \mathbf{b})/3$ ,  $-\mathbf{a}/3$  or  $-\mathbf{b}/3$  with equal probability. Depending on the choice of the O atom arrangement the signs of these vectors may also be inverted. Ordered occurrence of these shifts would lead to three-dimensional superstructures. The simplest of these have the symmetries  $P3_112/P3_212$  (cyclic sequence of the three vectors),  $C2/m$  (occurrence of only one of the three vectors) and  $C2/c$  (alternate occurrence of two out of the three vectors). These superstructures,

however would give rise to superstructure reflections, well detectable in the XRPD patterns. Following such a scheme the superstructures possible for the presently discussed quaternary delafossites can be regarded as analogues of superstructures/stacking variants which occur, or can be constructed, for compounds like  $\text{Li}_2\text{SnO}_3$ ,  $\text{Li}_5\text{ReO}_6$ ,  $\text{V}_6\text{C}_5$  and  $\text{Pd}_6\text{B}$ <sup>90, 129-132</sup>

An approximate structure model employing a periodic sequence of the mentioned shift vectors ( $P3_112/P3_212$ ) was set up to calculate SAED patterns as well as HRTEM images. Indeed, the TEM investigations on  $\text{AgRhO}_2$ ,  $\text{AgLi}_{1/3}\text{Rh}_{2/3}\text{O}_2$  and  $\text{AgLi}_{1/3}\text{Ir}_{2/3}\text{O}_2$  confirm on single-crystal-type information the crystal structure models derived from XRPD. Nanoprobe EDX indicates the presence of Li atoms inside the  $[(\text{Ir,Rh})_2\text{LiO}_6]^{3-}$  octahedral layers. The ratio Ag : (Ir, Rh) was found significantly larger than 1 for the quaternary materials. In the case of  $\text{AgLi}_{1/3}\text{Rh}_{2/3}\text{O}_2$  the average of five point analyses performed on distinct crystallites gives Ag : Rh = 1.37(3), while for  $\text{AgRhO}_2$  the ratio was determined to 0.95(2) (three measurements). Both values are slightly smaller than the expected ones, 1.5 and 1.0, respectively based on the nominal compositions.

The metrics of the single crystalline fragments of  $\text{AgRhO}_2$  were examined for their consistence with calculated data via extended tilting series. The tilt angles between [211], [241], [541], [841], [8-21] were determined to be 24.9°, 24.6°, 17°, 33° in good agreement with the calculated values of 25.4°, 24.2°, 17.4° and 33°. Moreover, all d-values agree with the calculated ones within experimental errors. In the following, the metrics of  $\text{AgRhO}_2$  are used for the indexing of the  $\text{AgLi}_{1/3}\text{Rh}_{2/3}\text{O}_2$  diffraction pattern since these structures are highly related.



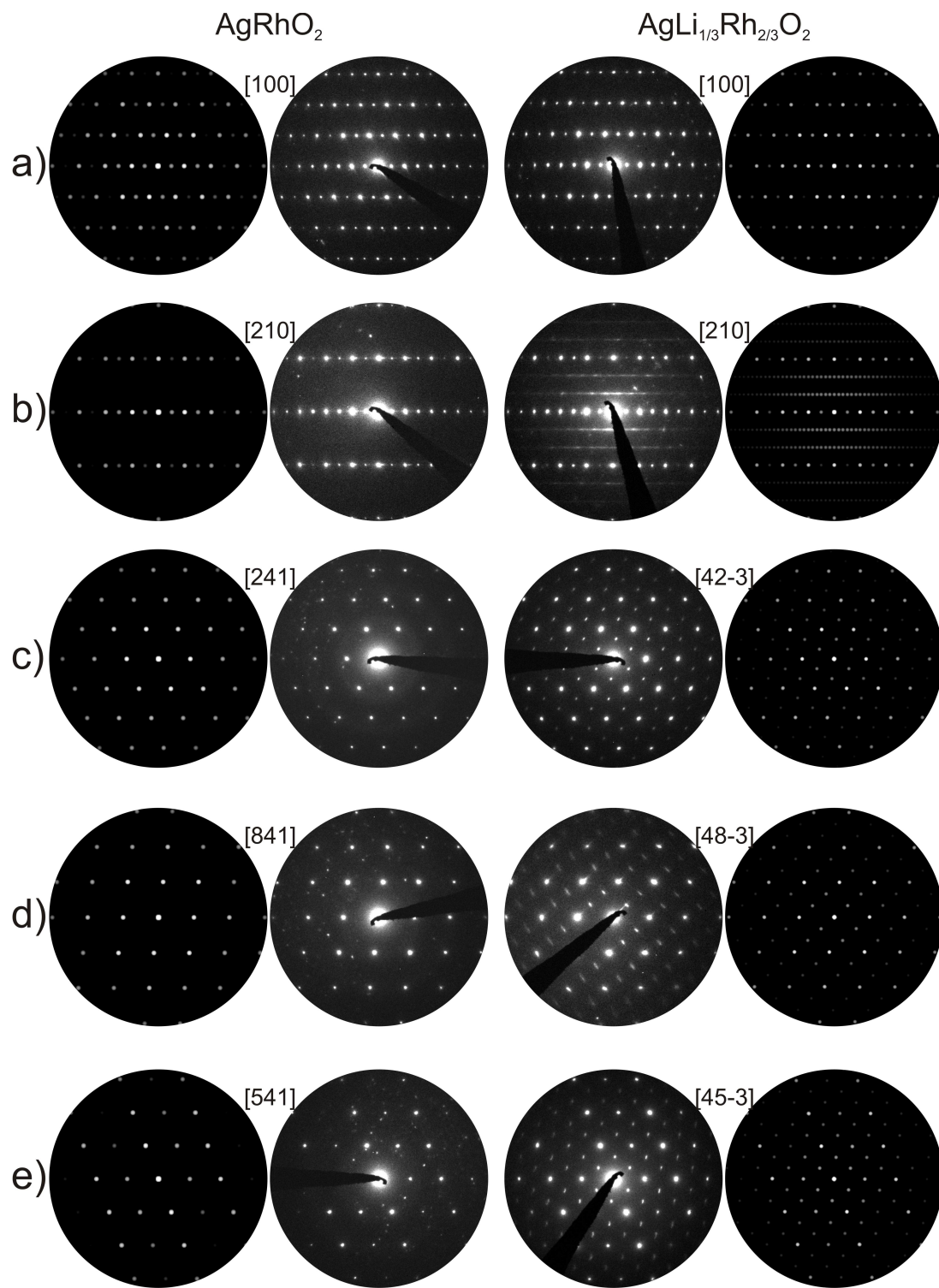


**Figure 4.1.25:** PED patterns for  $\text{AgRhO}_2$  (column 2) and  $\text{AgLi}_{1/3}\text{Rh}_{2/3}\text{O}_2$  (column 3) with simulated PED patterns (columns 1 and 4, respectively; zone axis specified in the figure) on the basis of the delafossite structure ( $\text{AgRhO}_2$ ) and the approximant supercell structure ( $\text{AgLi}_{1/3}\text{Rh}_{2/3}\text{O}_2$ ).

Figure 4.1.25 displays a comparison of the PED patterns of  $\text{AgRhO}_2$  (left column) and  $\text{AgLi}_{1/3}\text{Rh}_{2/3}\text{O}_2$  (right column). The attached simulated patterns for  $\text{AgRhO}_2$  based on its “normal” delafossite-type structure convincingly match the experimental data, thus confirming the trigonal structure model on single crystals. In the case of  $\text{AgLi}_{1/3}\text{Rh}_{2/3}\text{O}_2$  the fundamental reflections remain unchanged, however, additional intensities occur in the PED patterns, cf. additional spots (zone axes: [42-3], [48-3], [45-3], (Figure 4.1.25c, d, e) and the diffuse streaks for the zone axis pattern along [210].<sup>1</sup> Indeed these features are well predicted by the approximant superstructure model.

Note, that the assumed two-dimensional ordering of  $\text{AgLi}_{1/3}\text{Rh}_{2/3}\text{O}_2$  is not seen in *all* structure projections, as exemplified by the diffraction pattern of  $\text{AgLi}_{1/3}\text{Rh}_{2/3}\text{O}_2$ , which resembles the pattern of pure  $\text{AgRhO}_2$  along [100], cf. Figure 4.1.25a right vs. left. This contrasts to all zone axes where the honeycomb ordering is clearly seen in the structure projection, and where additional spots are present in the diffraction patterns. According to the real structure model, these spots are intersections of diffuse rods and the Ewald sphere, and not superstructure reflections, e. g. [241], [841] and [541] (Figure 4.1.25c, d, e).

Consequently, the intersections exhibit significant extension in the reciprocal space above and below the zero order Laue zone (ZOLZ). To image these contributions, PED is the method of choice<sup>133</sup>, as demonstrated by the comparison of SAED and PED patterns depicted in Figure 4.1.25. The diffuse rods are in-plane for the zone axis [210], thus SAED and PED patterns both show extended diffuse streaks on the positions  $\pm x(-1/3 \ 2/3 \ l)$  with  $x \neq 3n$  (with  $n$  being an integer; cf. Figure 4.1.26a). When tilting the sample perpendicular to  $\mathbf{c}^*$  by ca.  $19^\circ$  (zone axis [20 10 1], Figure 4.1.26b) the observable diffuse intensity is minimized and spots appear at the positions of intersections for SAED. In the PED patterns, the intersections appear elongated by the diffuse contributions above and below the ZOLZ, and the extension of the diffuse streaks scales with the precession angle. Thus PED enables to identify structural disordering even for the cases where disordering is not detected by techniques like SAED and HRTEM which are interrelated with the projection of the structure.

---

<sup>1</sup> All these phenomena were also observed with the stationary electron beam of the SAED technique.

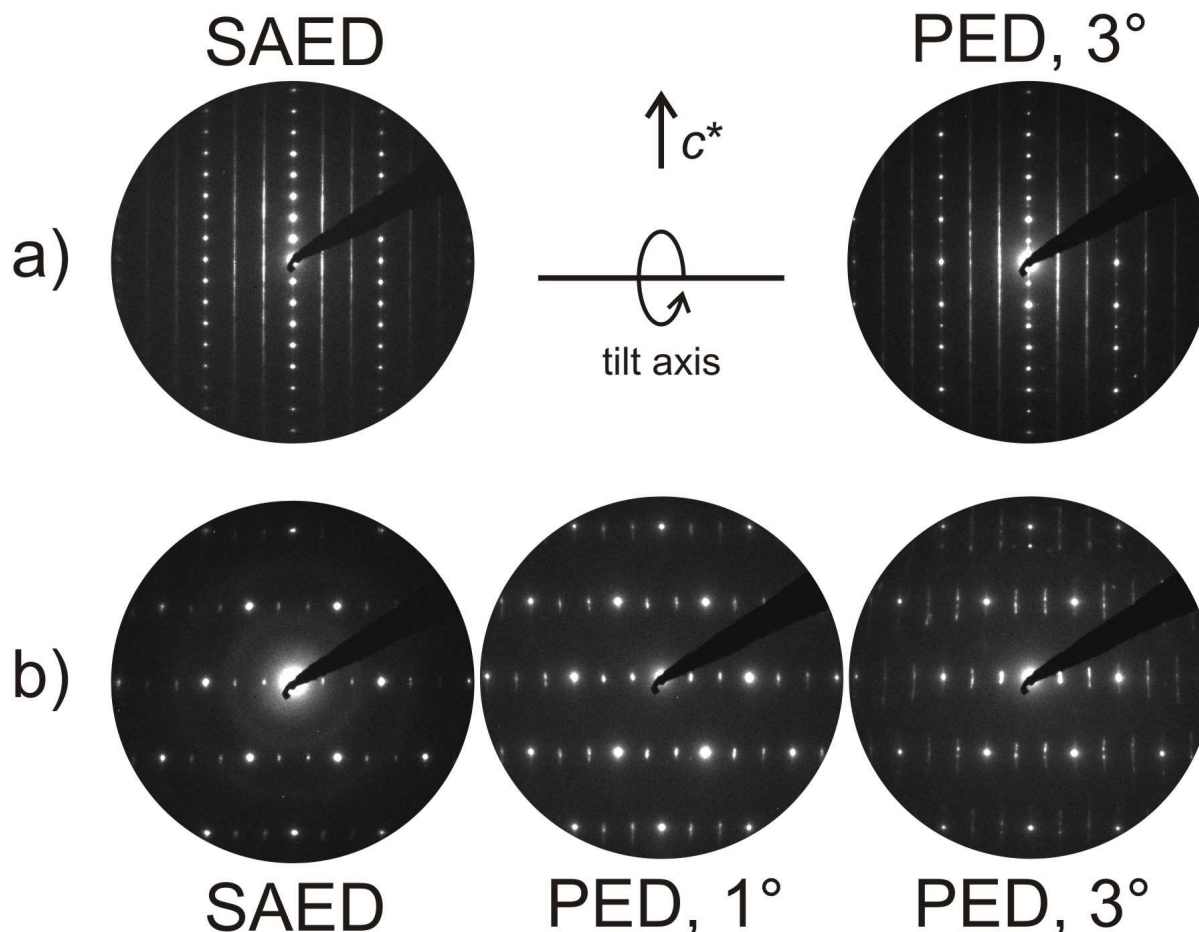


**Figure 4.1.26** a) SAED (left) and PED pattern (precession angle  $3^\circ$ ), zone axis  $[210]$ ; b) SAED (left) and PED patterns (center and right) after tilting the sample perpendicular to  $c^*$ . For the PED patterns, a precession angle of  $1^\circ$  (center) and  $3^\circ$  (right) was adjusted.

For the zone axis  $[210]$ , HRTEM was applied to prove the real-space structure model based on two dimensional ordering, cf. Figure 4.1.27b. In the case of the ordered crystals of  $\text{AgRhO}_2$ , the HRTEM micrographs convincingly match simulated images based on the trigonal structure model (Figure 4.1.27a). For  $\text{AgLi}_{1/3}\text{Rh}_{2/3}\text{O}_2$  (and analogously for  $\text{AgLi}_{1/3}\text{Ir}_{2/3}\text{O}_2$ ) the shifts of adjacent octahedral sheets are clearly visible, cf. horizontal lines with dark ( $\Delta f = -25$  nm, (Figure 4.1.27b), top right) and white spots ( $\Delta f = -90$  nm, Figure 4.1.27b), bottom right). A comparison of simulated micrographs and the projected potential indicates that these spots correlate with the honeycomb ordering of Li and Rh atoms inside the octahedral sheets. For  $\Delta f = -25$  nm, the imaging conditions of Scherzer focus are approximated, hence, the black spots correlate with the pairs of Rh atoms inside the ordered  $[\text{Rh}_2\text{LiO}_6]^{3-}$  sheets. The distinct

positions of the sheets are highlighted by the marks inside the projection of the approximant supercell structure (Figure 4.1.27c) and the corresponding marks inside the simulated micrographs (Figure 4.1.27b).

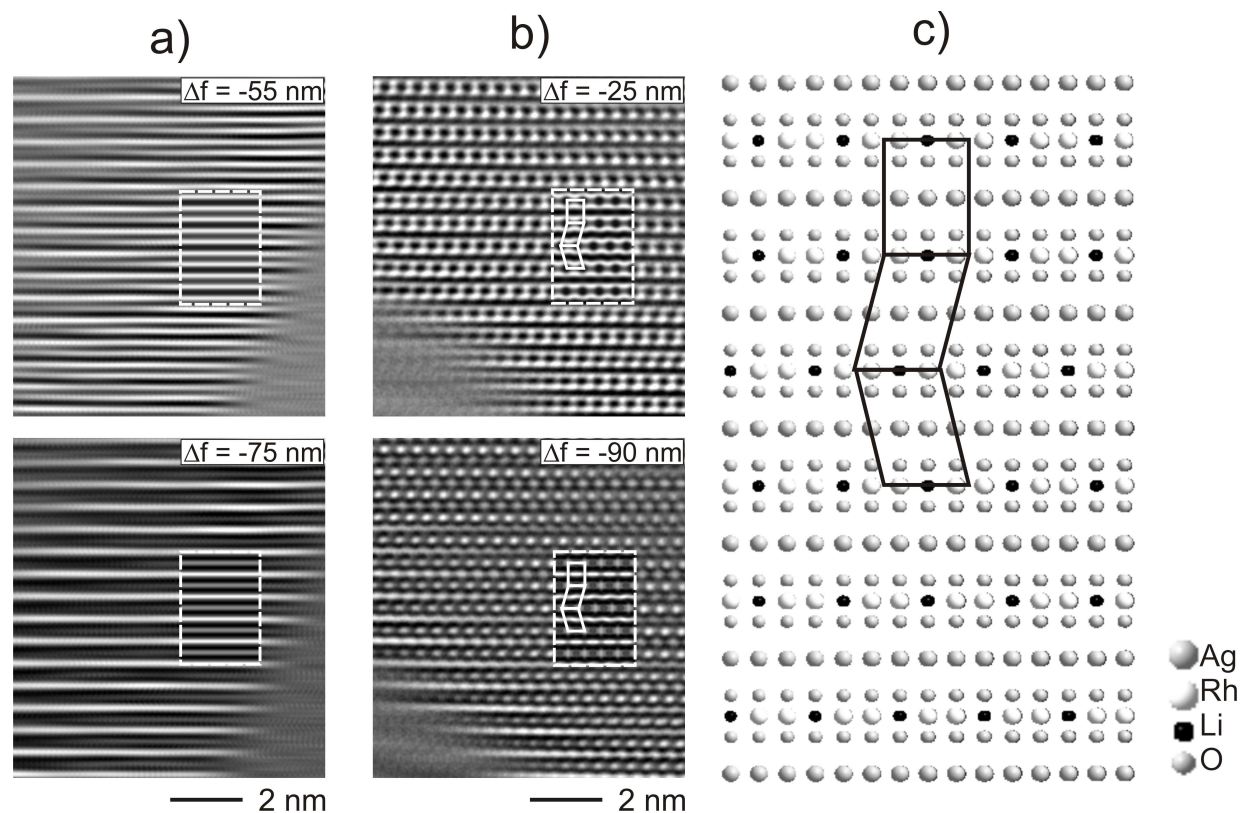


**Figure 4.1.27** HRTEM micrographs recorded on AgRhO<sub>2</sub> **a)** zone axis [210]) with inserted simulation, assumed thickness: 2.7 nm) and AgLi<sub>1/3</sub>Rh<sub>2/3</sub>O<sub>2</sub> **b)** assumed thickness: 4.8 nm). **c)** Projection of the supercell structure.

### 4.1.3.3. Physical characterization of $\text{AgRhO}_2$ and $\text{Ag}(\text{Li}_{1/3}\text{Rh}_{2/3})\text{O}_2$

#### $\text{AgRhO}_2$

##### *Thermal Stability*

The thermal stability was examined by the DTA - TG in inert atmosphere up to 1300 K. Above 1173 K the  $\text{AgRhO}_2$  starts to decompose to  $\text{Ag}_2\text{O}$  and  $\text{Rh}_2\text{O}_3$  with loss of oxygen. This mass loss of 6% is due to the decomposition of  $\text{Ag}_2\text{O}$ .

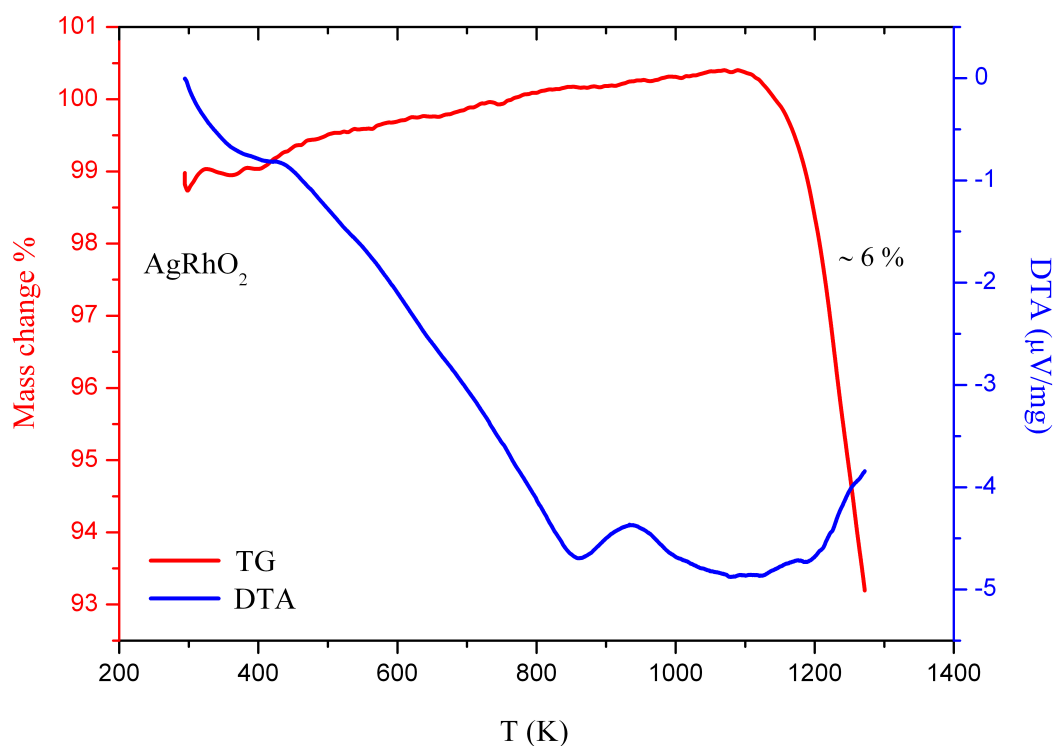


**Figure 4.1.28.** Thermal stability of  $\text{AgRhO}_2$ .

## Electrical Conductivity

$\text{AgRhO}_2$  is semiconducting, where the specific resistivity was measured in the temperature interval from 2 to 300 K. At lower temperatures the resistivity is rather high, close to the sensitivity limits of the machine as in the case of  $\text{AgCoO}_2$ . In the temperature window from 3 to 120 K it remains  $10^8 \Omega\cdot\text{cm}$ , afterwards drops with three orders of magnitude. The conductivity at room temperatures is found to be  $7.4\cdot 10^{-6} \Omega^{-1}\cdot\text{cm}^{-1}$ . The derived activation energy is  $17.59 \text{ kJ}\cdot\text{mol}^{-1}$ .

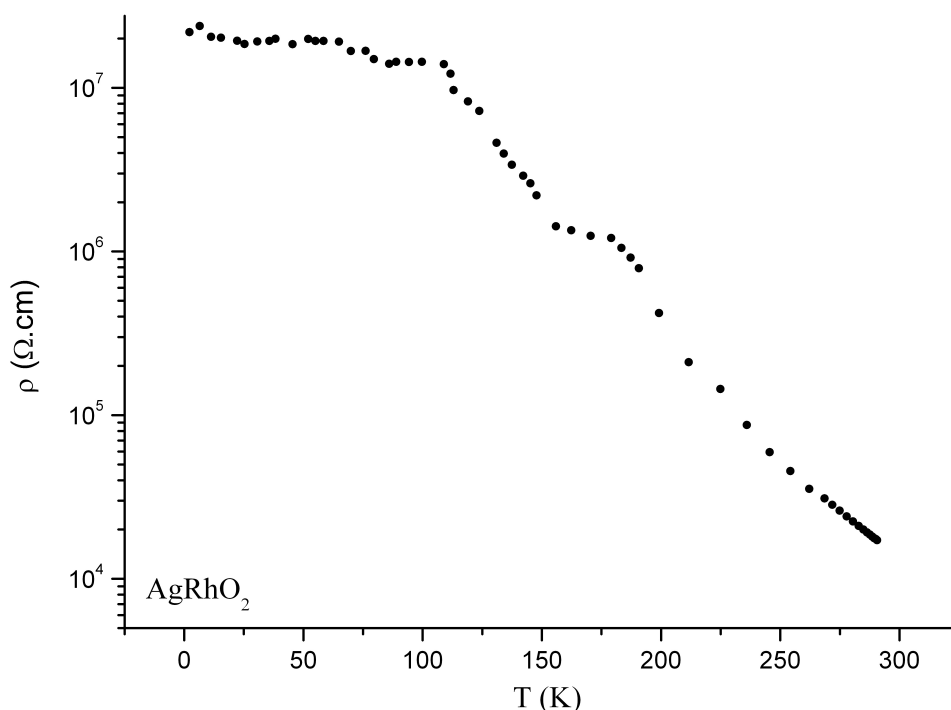


**Figure 4.1.29.** Temperature dependence of the specific resistivity of  $\text{AgRhO}_2$ .

## Seebeck coefficient

Figure 4.1.30 shows the temperature dependence of the thermoelectric power. The positive sign of the Seebeck coefficient proved the type of carriers in that compound is predominant holes and  $\text{AgRhO}_2$  being a p-type semiconductor. The room temperature value is  $120 \mu\text{V}\cdot\text{K}^{-1}$

and it increases with increasing of temperature up to  $171 \mu\text{V}\cdot\text{K}^{-1}$  at 440 K. The thermoelectric power factor ( $\tau_p$ ) for room temperature is  $1.07\cdot 10^{-4} \text{ W}\cdot\text{m}^{-1}\cdot\text{K}^{-2}$  ( $\alpha = -20 \mu\text{V}\cdot\text{K}^{-1}$   $\sigma = 3.99\cdot 10^{-3} \Omega^{-1}\cdot\text{cm}^{-1}$ )

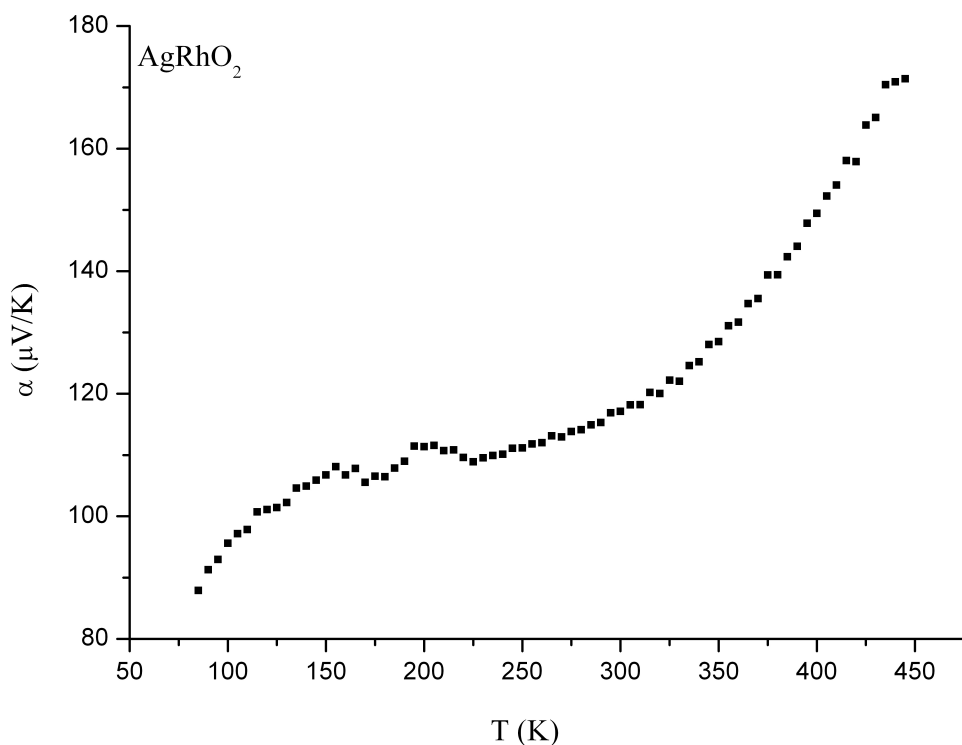
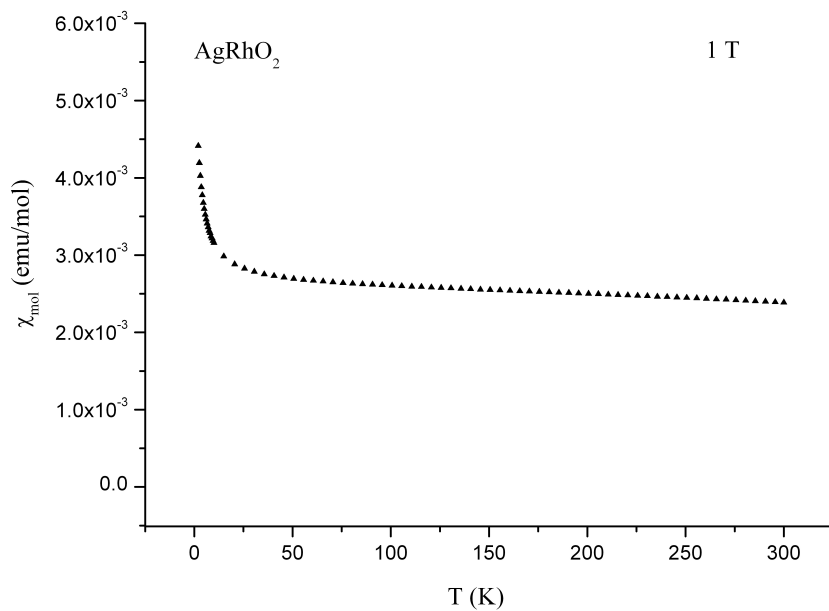


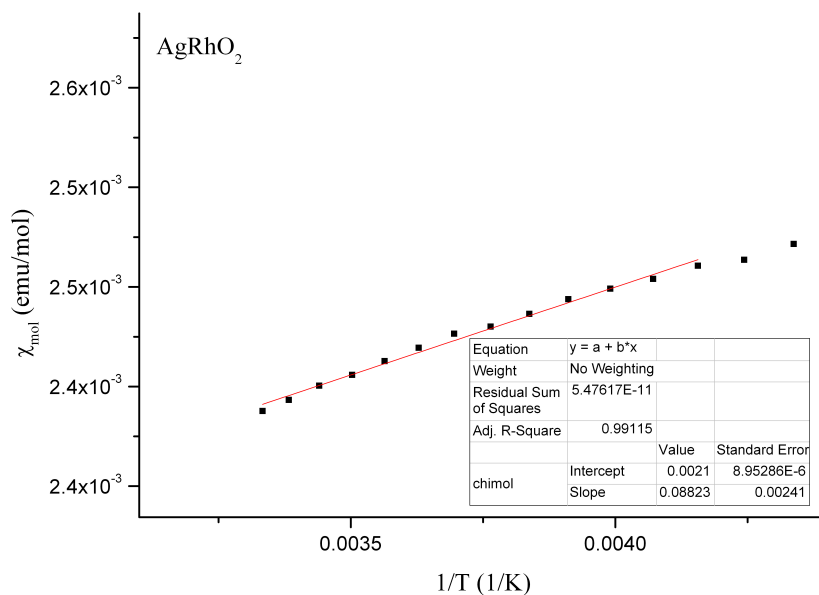
**Figure 4.1.30.** Temperature dependence of Seebeck coefficient of  $\text{AgRhO}_2$ .

### *Magnetic Susceptibility*

$\text{AgRhO}_2$  shows almost constant magnetic susceptibility in a quite wide temperature range (TIP), with a slight Curie tailing, analogous to  $\text{NaCoO}_2$  and  $\text{AgCoO}_2$ <sup>46</sup>. A reason of that paramagnetism could be the strong orbital interaction (Van Vleck paramagnetism) or the slightly distortion in the rhodium octahedral. The percentage of the Curie impurity as well as the temperature independent term was calculated for three applied magnetic fields of 1, 3 and 7 Tesla. The temperature independent paramagnetism (TIP) was found to be  $3.91\cdot 10^{-5} \text{ cm}^3\cdot\text{mol}^{-1}$ , whereas the Curie impurities were estimated to 2 %, of  $S=1/2$ , species.



a)



b)

**Figure 4.1.31. a)** The magnetisation as a function of temperature; **b)** The molar susceptibility as function of reverse temperature for determination of the impurities.





*Thermal Stability*

The thermal stability was examined up to 1200 K in an argon atmosphere, with normal heating rate of 10 K/min. This compound shows thermal stability up to 950 K. The decomposition is accompanied with mass loss of ~ 4 %, corresponding to decomposition of Ag<sub>2</sub>O.

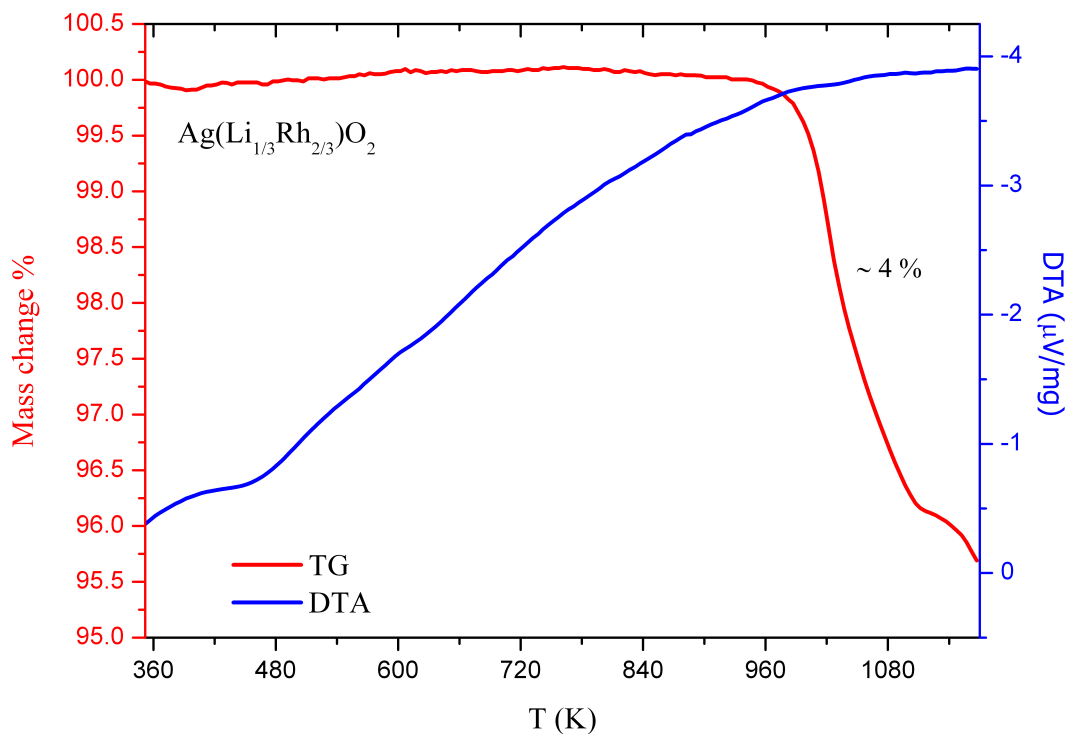


**Figure 4.1.32.** Thermal stability of Ag(Li<sub>1/3</sub>Rh<sub>2/3</sub>)O<sub>2</sub>.

### Electrical Conductivity

The resistivity was recorded in the temperature range from 3 to 300 K, the highest value of the specific resistivity is  $10^4$  ( $\Omega\cdot\text{cm}$ ), which is far from the sensitivity limits of the machine. The compound is semiconducting, with an activation energy of  $4.97 \text{ kJ}\cdot\text{mol}^{-1}$ . The conductivity at 300 K is  $9.0 \text{ }\Omega^{-1}\cdot\text{cm}^{-1}$

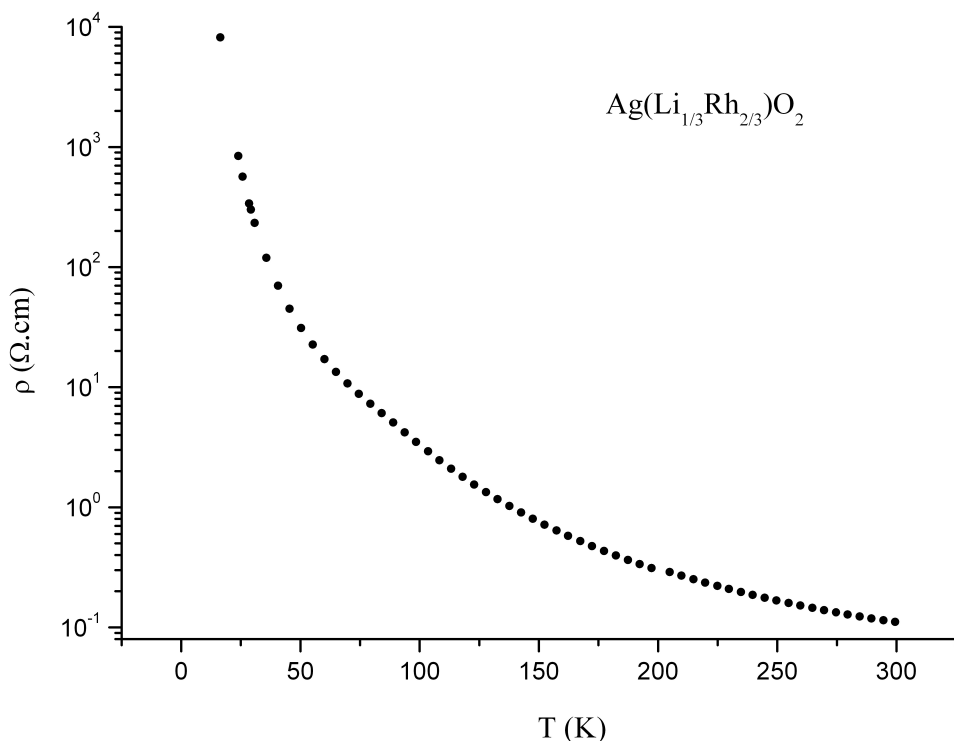


**Figure 4.1.33.** Temperature dependence of the specific resistivity of  $\text{AgLi}_{1/3}\text{Rh}_{2/3}\text{O}_2$ .

### Seebeck coefficient

The curve characterizing the thermoelectric power of that material shows more complicated behavior. At lower temperature the Seebeck coefficient has a negative sign corresponding to the conductivity caused by the electrons. At temperatures higher than 150 K it increases linear with the temperature, changing its sign. That indicates different conduction mechanism, which could be explained with  $d^{10} - d^{10}$  interactions<sup>72</sup>. The conductivity mechanism changes from n-

to p-type around that temperature. That is an indication for different influences. At low temperature range the conductivity is mostly due to  $\text{Rh}^{4+}$  electrons and with increasing the temperature the influence of the  $\text{Ag}^+$  ( $d^{10}$ ) becomes higher. That could be referred to the structure and respectively the bond lengths  $\text{Ag} - \text{Ag}$  of  $3.02085 \text{ \AA}$  being slightly bigger than that in metallic silver ( $2.89 \text{ \AA}$ ). This explains the lower electron mobility at higher temperatures, changing the type of carriers to holes.

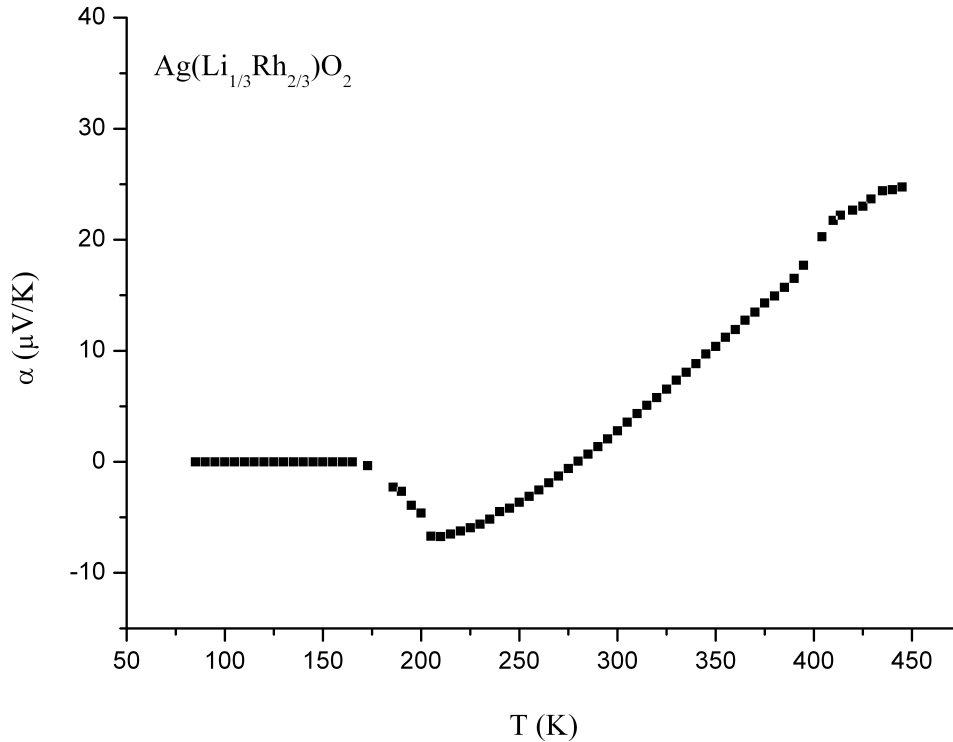


**Figure 4.1.34.** Temperature dependence of Seebeck coefficient of  $\text{AgLi}_{1/3}\text{Rh}_{2/3}\text{O}_2$ .

### *Magnetic Susceptibility*

The magnetic response was recorded in the temperature interval from 3 to 360 K. From 3 to 90 K there is an antiferromagnetic ordering with a  $T_N = 95 \text{ K}$ .  $\text{AgLi}_{1/3}\text{Rh}_{2/3}\text{O}_2$ , is paramagnetic obeying the Curie-Weiss law in the temperature range of 150 to 360K. From a respective evaluation, an effective magnetic moment of  $1.70 \mu_B$  for Rh was calculated. This value is in a

good correspondence with the spin – only value of  $1.73 \mu_B$  for low spin of  $4d^5$  and  $5d^5$  configurations.

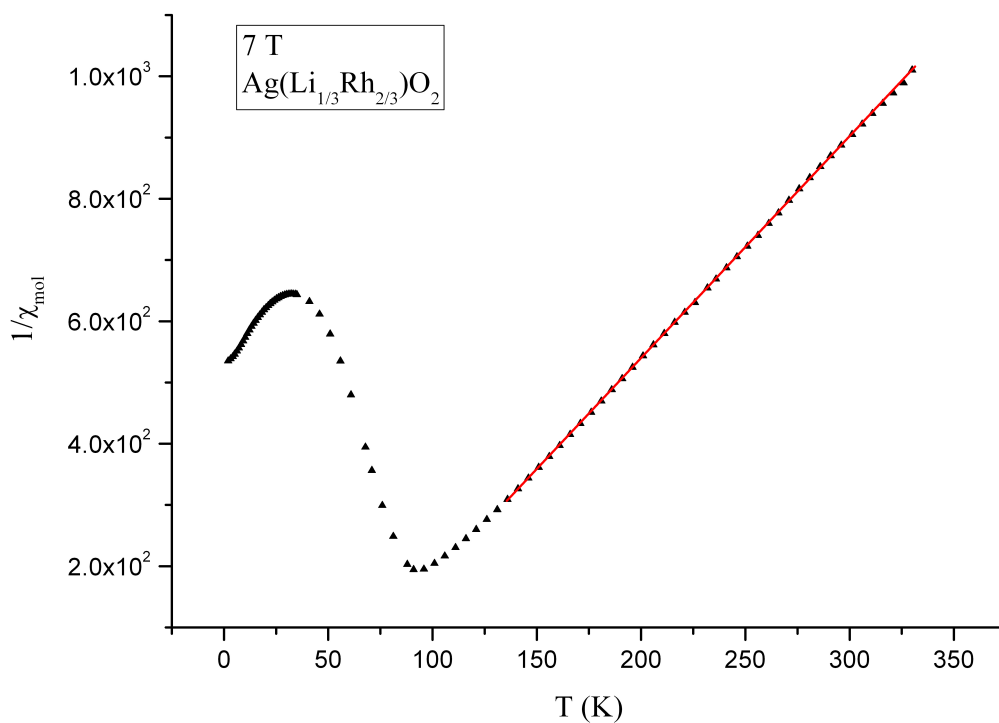


**Figure 4.1.35.** Inverse molar susceptibility as function of temperature for  $\text{AgLi}_{1/3}\text{Rh}_{2/3}\text{O}_2$ .

#### 4.1.4. Systems Ag – Ir – O and Ag – Li – Ir – O

As already discussed,  $\text{AgIrO}_2$  could not be synthesised yet, although the valence state of 3+ is known to be one of the most common for iridium. Number of different experiments was done. On one hand all-solid-state reactions applying high oxygen pressure have failed, because of the intricate control of the oxygen pressure required: at a too low oxygen pressure silver oxide gets reduced to elemental silver, while at higher pressure phases containing  $\text{Ir}^{4+}$  result. On the other hand, analogues synthesis to this of  $\text{AgRhO}_2$  starting from  $\text{LiRhO}_2$ , and further treatment with  $\text{AgNO}_3/\text{KNO}_3$ , could not be used. The problems with the synthesis of  $\text{LiIrO}_2$  were the same like in the direct approach – stability of the starting oxides. In fact there is no crystal structure of the binary oxide  $\text{Ir}_2\text{O}_3$  characterized yet.

First Claus<sup>134</sup> reported difficulties with the synthesis in pure form and recommended dry-synthesis approach (solid state reaction), followed up with research on the iridium oxygen system<sup>135, 136</sup> from Wöhler and Witzmann leading to the same conclusions. Through the wet approach (solvent mediated reaction) the sample is contaminated with impurities, whereas by the dry approach  $\text{Ir}_2\text{O}_3$  disproportionate to metal Ir and  $\text{IrO}_2$ .

An alternative approach to synthesize  $\text{AgIrO}_2$  was an electrochemical intercalation of silver in  $\text{IrO}_2$  accompanied with reduction of  $\text{Ir}^{4+}$  to  $\text{Ir}^{3+}$ . The experiment assembly is shown in Figure 4.1.37.

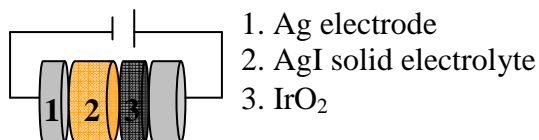
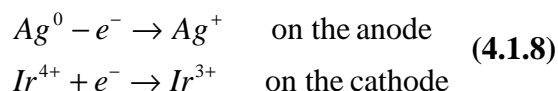


**Figure 4.1.36.** Assemblies of electrochemical cell for intercalation of silver in  $\text{IrO}_2$  in a solid state.

Two different starting systems - amorphous and crystalline  $\text{IrO}_2$  were used for the experiments. The dissolving of the silver anode indicated the expected reaction to proceed; however, two different products were obtained, depending on the starting material, whether a crystalline or amorphous oxide was used. The highly ordered crystalline system did not accommodate silver ions at any current density and a silver layer on the oxide surface was observed. The intercalation of silver was only possible into the amorphous  $\text{IrO}_2$ . The obtained sample was amorphous as well, and showed a Ag:Ir ratio of 1:1, determined by EDX analysis (Table 1

Appendix). The half reactions of the electrochemical intercalation process are given in equation (4.1.8).



For the structural description powder/single crystal X-ray data are necessary, for that purpose different approaches to get the compound crystalline were applied. The amorphous sample was filled in quartz capillary, heated up to desired temperature and the diffractogram was recorded. Figure 4.1.38 shows a series of powder diffractograms. Unfortunately all attempts were unsuccessful, resulting with mixture of two phases – elementary silver and iridium oxide. Possible reason for that could be that reaction (1) does not occur on that way and a compound  $\text{AgIrO}_2$  does not exist even amorphous. As far as the silver intercalation happens in an open system, instead of  $\text{Ag}^+\text{Ir}^{3+}\text{O}_2$ , amorphous  $\text{Ag}^0\text{Ir}^{4+}\text{O}_2$  might be built, which during the crystallization decomposes in Ag and  $\text{IrO}_2$ .

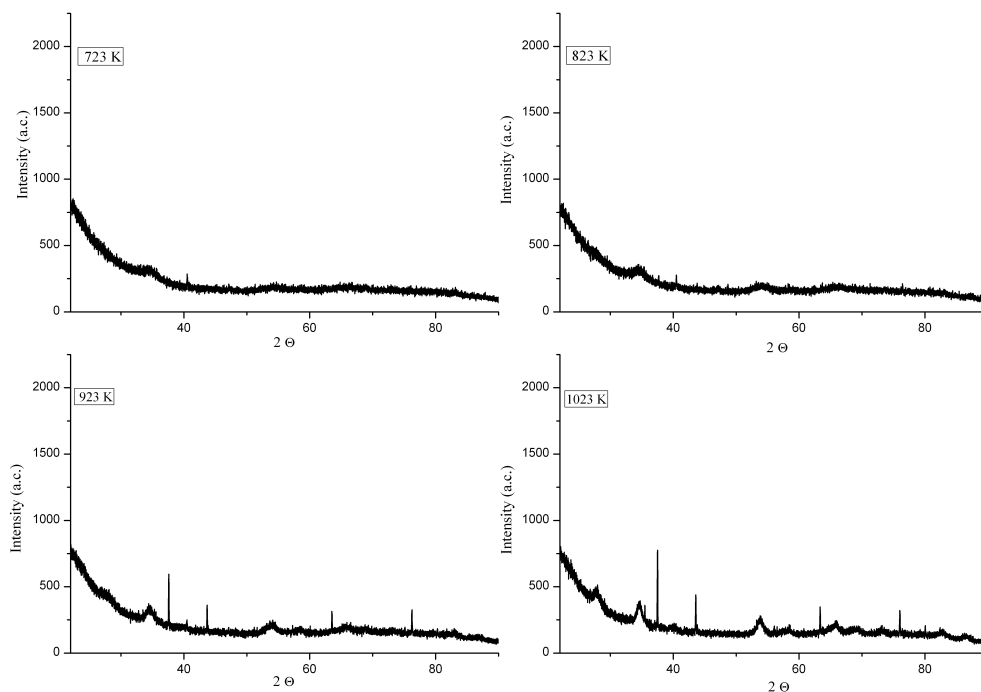


**Figure 4.1.37.** Powder pattern of intercalated silver in  $\text{IrO}_2$ . The narrow reflections at 923 K and 1023 K belong to elementary silver, the broad reflections to  $\text{IrO}_2$ , respectively.

The delafossite structure comprising silver and iridium was realized through the quaternary  $\text{Ag}(\text{Li}_{1/3}\text{Ir}_{2/3})\text{O}_2$ .

#### **4.1.4.1. Synthesis of $\text{Ag}(\text{Li}_{1/3}\text{Ir}_{2/3})\text{O}_2$**

For the synthesis of  $\text{AgLi}_{1/3}\text{Ir}_{2/3}\text{O}_2$ ,  $\text{Li}_2\text{IrO}_3$  was treated with an excess of molten mixture of  $\text{AgNO}_3$  (Roth, 99%) /  $\text{KNO}_3$  (Merk 99.9%) in a ratio of 2:1. That reaction was performed in a sealed glass tube under Ar, with heating rate of 10 K/min up to 623 K, hold for 350 hours, and cooled by room temperature. The obtained sample was washed with distilled water several times in order the non reacted nitrates to be removed.  $\text{Li}_2\text{IrO}_3$  was prepared by reacting stoichiometric mixtures of  $\text{IrO}_2$  (Alfa Aesar, 99.9 %) and  $\text{LiOH}$  (Alfa Aesar, anhydrous, 99.9 %). The mixture was carefully ground and heated in corundum crucible, placed in quartz tube. The mixture was heated with 8 K/min up to 1123 K in an oxygen flow and held for 48 h at that temperature, followed by cooling.

#### **4.1.4.2. Structural characterization of $\text{Ag}(\text{Li}_{1/3}\text{Ir}_{2/3})\text{O}_2$**

$\text{Ag}(\text{Li}_{1/3}\text{Ir}_{2/3})\text{O}_2$  is isostructural with  $\text{Ag}(\text{Li}_{1/3}\text{Rh}_{2/3})\text{O}_2$  and was firstly synthesized looking for the possibilities to obtain a delafossite arrangement. As it can be seen from the Figure 4.1.39 the similarity of measured and calculated pattern is rather good, except for two additional reflections. The theoretical pattern of  $\text{AgIrO}_2$  is calculated based on 3R delafossite type with the cell parameters for  $\text{AgRhO}_2$ . The detailed structural description is provided in the section 4.1.3.2. Structural characterization of  $\text{Ag}(\text{Li}_{1/3}\text{Rh}_{2/3})\text{O}_2$ . The cell parameters of  $a = 3.04779(4)$  Å and  $c = 18.73348(4)$  Å are slightly bigger than those of the rhodium analogue compound.

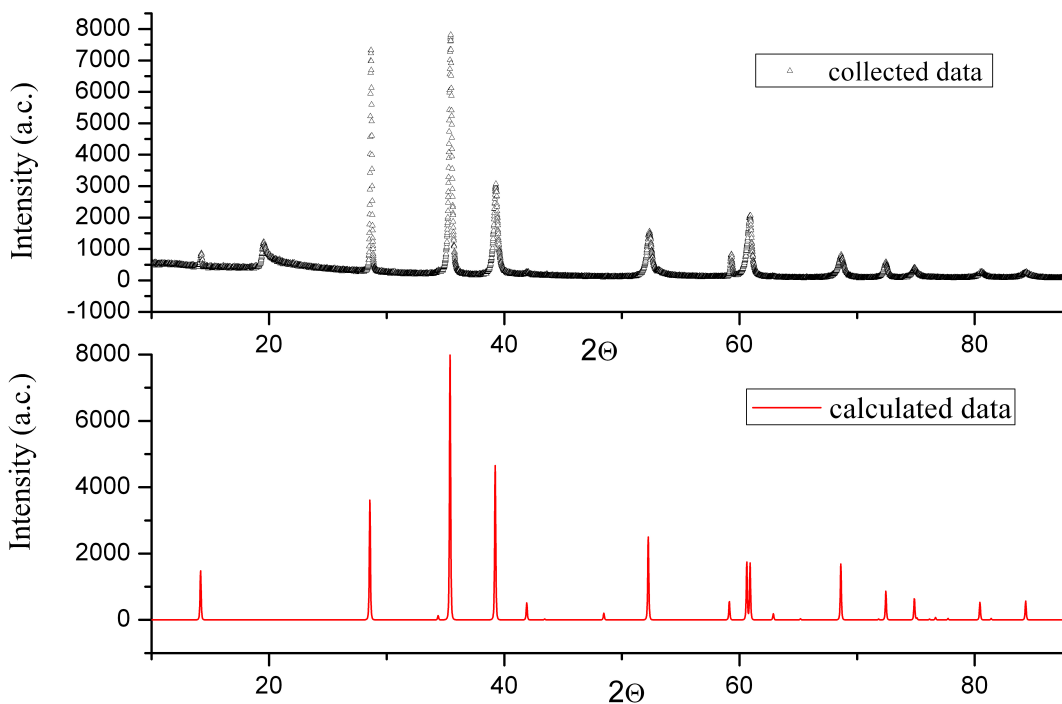


**Figure 4.1.38.** Powder pattern of measured  $\text{Ag}(\text{Li}_{1/3}\text{Ir}_{2/3})\text{O}_2$  ( $R\bar{3}m$ ) and calculated  $\text{AgIrO}_2$  ( $R\bar{3}m$ ), based on crystal data of  $\text{AgRhO}_2$  with the cell parameters obtained after LeBail fit of  $\text{Ag}(\text{Li}_{1/3}\text{Ir}_{2/3})\text{O}_2$ .

Rietveld refinement in an average delafossite structure can be seen on Figure 4.1.39, structural parameters, refined fractional coordinates; occupancies are listed in Table 4.1.12 and Table 4.1.13.



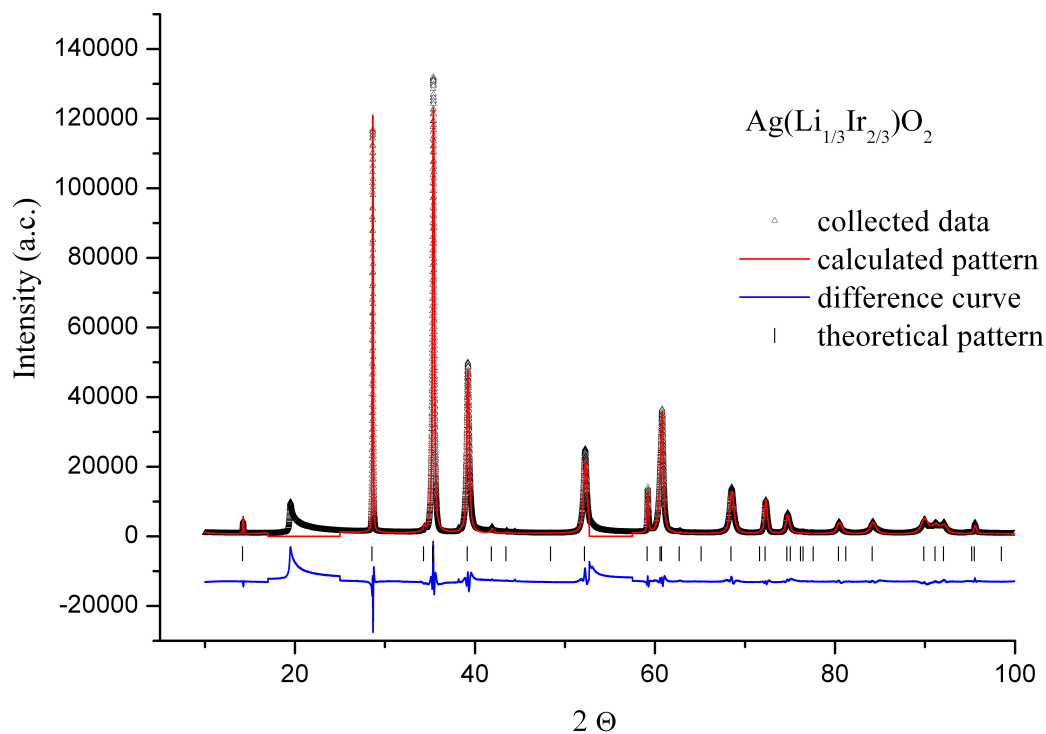


**Figure 4.1.39.** Observed (black), calculated (red) and difference (blue) tracks of X-ray powder diffraction for  $\text{Ag}(\text{Li}_{1/3}\text{Ir}_{2/3})\text{O}_2$ . Tick marks represent the calculated peak positions.

Table 4.1.12. Atomic positions of  $\text{Ag}(\text{Li}_{1/3}\text{Ir}_{2/3})\text{O}_2$

Atom	Wyckoff Positions	$x$	$y$	$z$	Occ.
Ag	$3a$	0	0	0	1
Li	$3b$	0	0	0.5	0.3528(8)
Ir	$3b$	0	0	0.5	0.6472(8)
O	$6c$	0	0	0.1047(1)	1

Table 4.1.13. Crystallographic and refinement details for  $\text{Ag}(\text{Li}_{1/3}\text{Ir}_{2/3})\text{O}_2$  refined by the Rietveld method.

Molecular formula	$\text{Ag}(\text{Li}_{0.3528}\text{Ir}_{0.6472})\text{O}_2$
Formula weight (in g/mol)	266.75
Space group	$R\bar{3}m$ ( <b>166</b> )
$a / \text{Å}$	3.04779(4)
$c / \text{Å}$	18.73348 (4)
$V / \text{Å}^3$	150.702(4)
$Z$	3
Calc. density ( $\text{g cm}^{-3}$ )	8.817(4)
Temperature (K)	293
Wavelength ( $\text{Å}$ )	1.5406
$R_{\text{exp}} (\%)^*$	1.87
$R_p (\%)^*$	7.99
$R_{\text{wp}} (\%)^*$	10.87
$\text{gof}^*$	5.80
$R(F^2) (\%)^*$	3.54
Starting angle ( $^\circ 2\theta$ )	10
Final angle ( $^\circ 2\theta$ )	100
Step width ( $^\circ 2\theta$ )	0.01
Scan time	40 h
No. of variables	29

Table 4.1.14. Bond Length in the  $\text{AgCoO}_2$ ,  $\text{AgRhO}_2$ ,  $\text{Ag}(\text{Li}_{1/3}\text{Rh}_{2/3})\text{O}_2$  and  $\text{Ag}(\text{Li}_{1/3}\text{Ir}_{2/3})\text{O}_2$ .

Bond length (Å) Bond type	$\text{AgCoO}_2$	$\text{AgRhO}_2$	$\text{Ag}(\text{Li}_{1/3}\text{Rh}_{2/3})\text{O}_2$	$\text{Ag}(\text{Li}_{1/3}\text{Ir}_{2/3})\text{O}_2$
Ag – Ag	2.86419	3.06882	3.02085	3.04781
Ag – O	2.09211	2.0167(45)	2.0557(12)	1.9631(23)
Co – O	1.90767			
Rh – O		2.0759(23)	2.04170(62)	
Ir – O				2.1071(12)
Li – O			2.04170(62)	2.1071(12)

Bond lengths, characteristic for those compounds are summarized in Table 4.1.14, to lighten the comparison in between.

#### 4.1.4.3. Physical characterization of $\text{Ag}(\text{Li}_{1/3}\text{Ir}_{2/3})\text{O}_2$

##### *Thermal Stability*

The thermal stability was examined up to 1200 K in an argon atmosphere, with normal heating rate of 10 K/min. This compound shows thermal stability up to 800 K. The decomposition is accompanied with mass loss of  $\sim 2.5\%$ , corresponding to decomposition of  $\text{Ag}_2\text{O}$ .

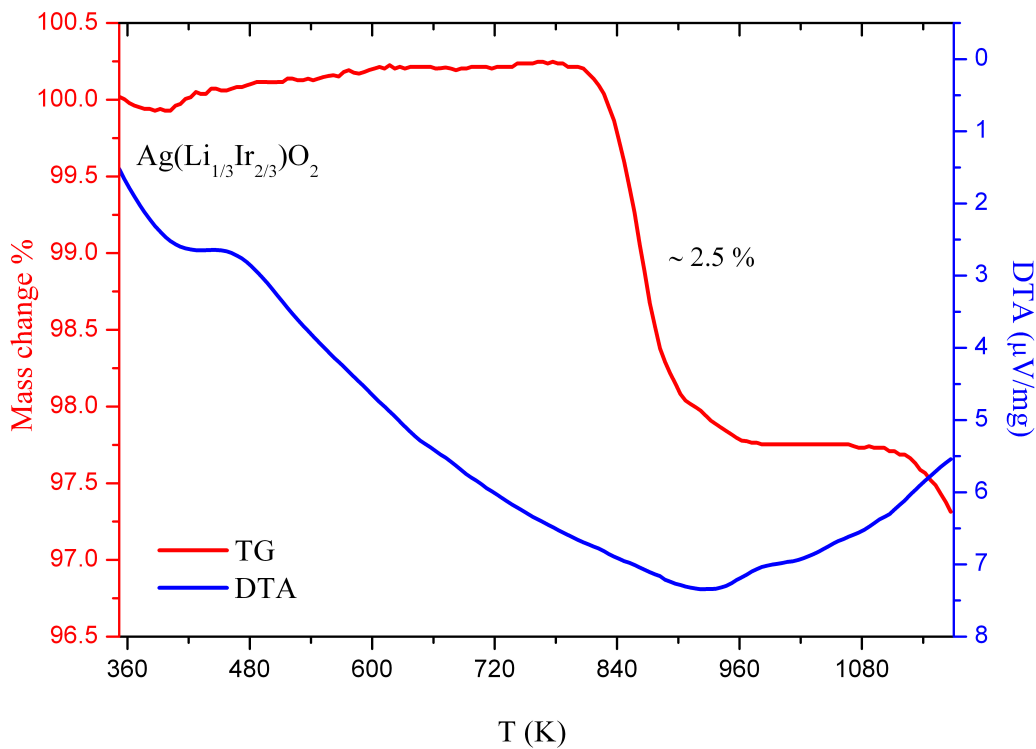


**Figure 4.1.40.** Thermal stability of  $\text{Ag}(\text{Li}_{1/3}\text{Ir}_{2/3})\text{O}_2$ .

### Electrical Conductivity

The resistivity was recorded in the temperature range from 3 to 300 K, the highest value of the specific resistivity is  $10^8$  ( $\Omega\cdot\text{cm}$ ), which corresponds to the sensitivity limits of the equipment. The compound is semiconducting, with activation energy of  $11.42 \text{ kJ}\cdot\text{mol}^{-1}$   $\text{AgLi}_{1/3}\text{Ir}_{2/3}\text{O}_2$ . The conductivity at 300 K is  $1.7\cdot 10^{-2} \text{ }\Omega^{-1}\cdot\text{cm}^{-1}$

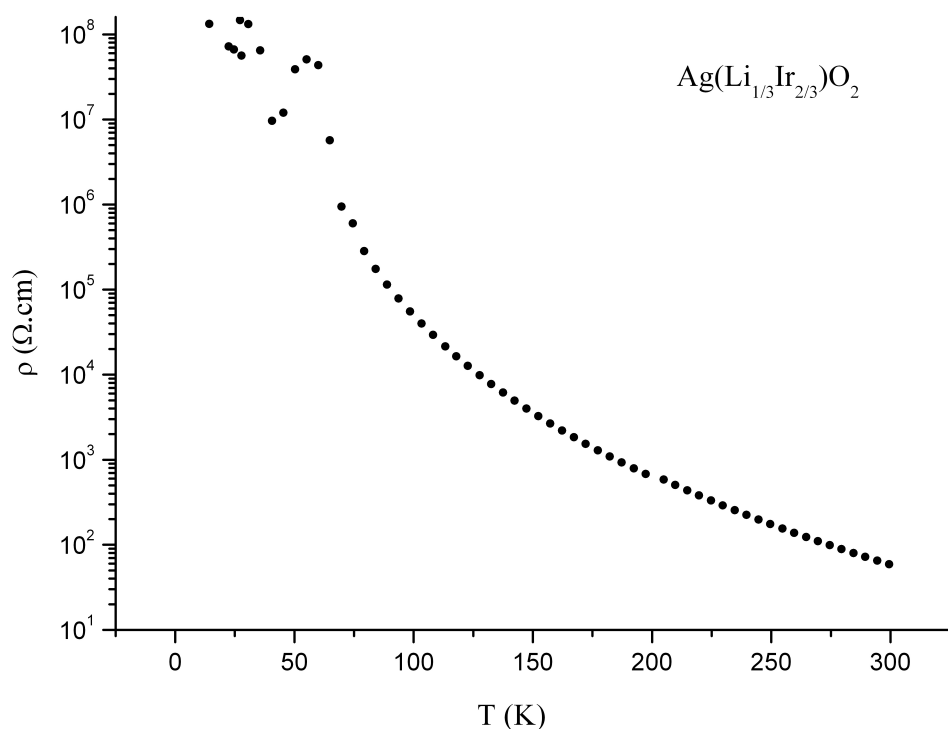


**Figure 4.1.41.** Temperature dependence of the specific resistivity of  $\text{AgLi}_{1/3}\text{Ir}_{2/3}\text{O}_2$ .

### Seebeck coefficient

The thermoelectric power is negative up to 100 K corresponding to n-type semiconductor. That behavior could be explained analogously to the  $\text{AgLi}_{1/3}\text{Rh}_{2/3}\text{O}_2$  case, where the electrons are provided instead from Rh from the Ir ( $d^5$ ). The curve shows a plateau from 100 to

approximately 150 K followed by linear slope. The Seebeck coefficient has a maximal value of  $93 \mu\text{V}\cdot\text{K}^{-1}$ .

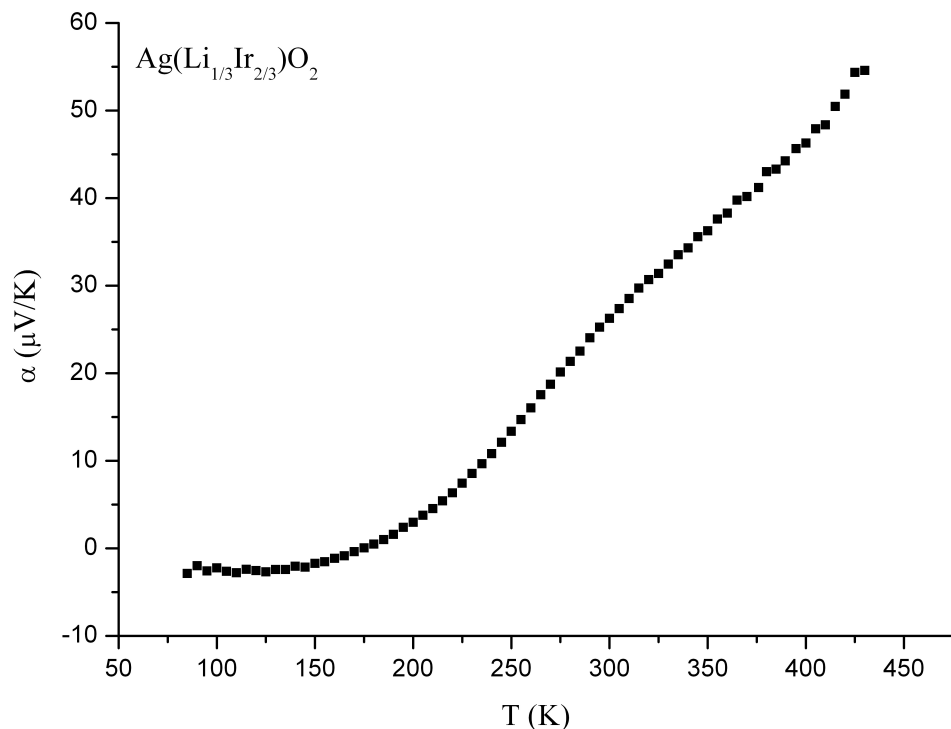


**Figure 4.1.42.** Temperature dependence of Seebeck coefficient of  $\text{AgLi}_{1/3}\text{Ir}_{2/3}\text{O}_2$ .

### *Magnetic Susceptibility*

The magnetic response was recorded in the temperature interval from 3 to 360 K. In that sample an antiferromagnetic ordering occurs in much lower temperature compare to rhodium analogue,  $T_N = 13$  K.  $\text{AgLi}_{1/3}\text{Ir}_{2/3}\text{O}_2$  is paramagnetic obeying the Curie-Weiss law in the temperature range of 150 to 360K. From respective evaluation, effective magnetic moment of  $1.77 \mu_B$  for Ir was calculated. This numbers are in a good correspondence with the spin – only value of  $1.73 \mu_B$  for low spin of  $4d^5$  and  $5d^5$  configurations.

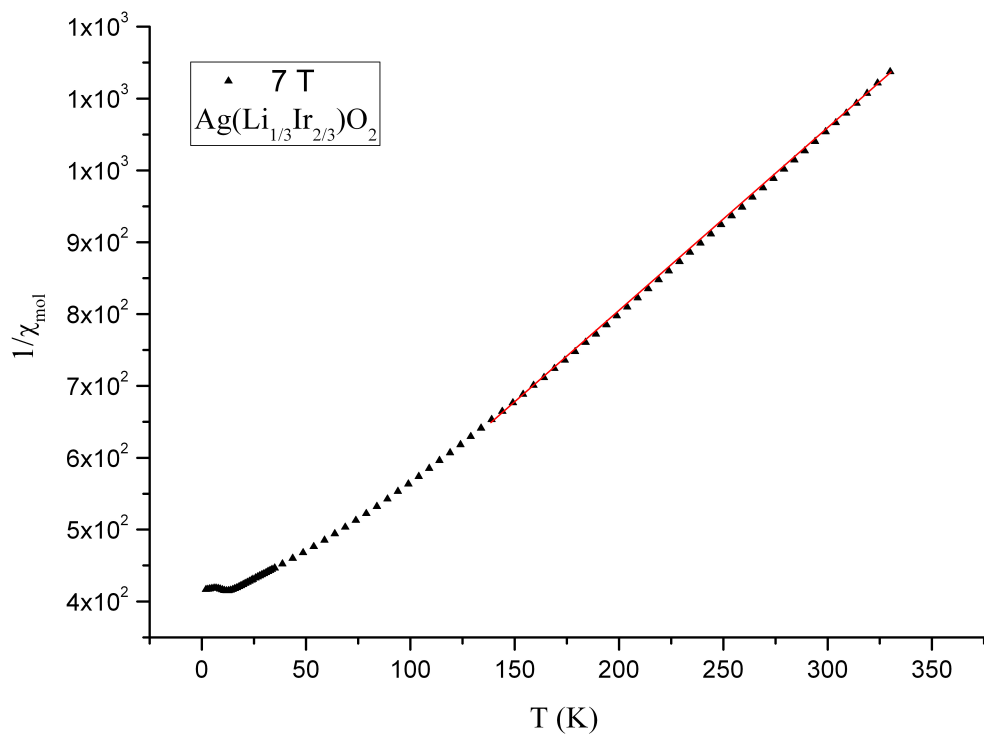


**Figure 4.1.43.** Inverse molar susceptibility as function of temperature for  $\text{AgLi}_{1/3}\text{Ir}_{2/3}\text{O}_2$ .

#### 4.1.5. Concluding remarks

New ternary and quaternary transition metal oxides were synthesized in the scope of this PhD work.  $\text{Li}_2\text{RhO}_3$ ,  $\text{AgRhO}_2$ ,  $\text{Ag}(\text{Li}_{1/3}\text{Rh}_{2/3})\text{O}_2$  and  $\text{Ag}(\text{Li}_{1/3}\text{Ir}_{2/3})\text{O}_2$  are layered compounds, whose structures can be derived from the rock salt type. The lithium rhodate crystallizes in monoclinic space group  $C2/m$ , whereas the silver comprising transition metal oxides in space group  $R\bar{3}m$ . Different physical properties were examined in order to fully characterize the new oxides. The thermal behavior was investigated, and a stability range was defined, phase transitions of the new compounds at higher temperatures were not observed. The electric conductivity of all samples was measured in temperature range from 3 to 300 K, whereas the ionic conductivity was investigated only in case of  $\text{Li}_2\text{RhO}_3$  in the temperature range from 300 to 500 K. The resistivity of all samples decreases with the increasing of temperature, corresponding to semiconductive behavior. It was possible to designate the conductivity type on base of thermoelectric power measurements, however further investigations at lower temperatures might be helpful to get a deeper insight into the conductivity mechanism.

Magnetic behavior enquiries, combined with the results of the conductivity measurements showed consistent agreement with the theory. In the case of  $\text{RhO}_2$  it has been proven that the distorted rutile structure favors the localization of the  $d_{xy}$  – orbital and determines the cation – cation interactions. This explains the high effective magnetic moment and the metal conductivity via three-dimensional cation-anion-cation interaction. The metallic behavior changes to semiconductive in case of the  $\text{Li}_2\text{RhO}_3$  and  $\text{Ag}(\text{Li}_{1/3}\text{Rh}_{2/3})\text{O}_2$ , proving the electron deficiency in the conduction band. In contrast to  $\text{RhO}_2$ , both compounds exhibit edge – sharing  $\text{RhO}_6$  octahedra, forming two dimensional layers. These octahedra are alternately filled either with  $\text{Li}^+$  or  $\text{Ag}^+$ . The structural reduction from three dimensional to two dimensional already indicates a disturbance of the cation-anion-cation interaction compared to that in  $\text{RhO}_2$ . In  $\text{Li}_2\text{RhO}_3$  and  $\text{Ag}(\text{Li}_{1/3}\text{Rh}_{2/3})\text{O}_2$ , the  $t_{2g}$  orbitals of rhodium are occupied by five electrons, four paired and one unpaired, leading to the effective magnetic moment close to the ideal value of  $1.73 \mu_B$  for  $S = 1/2$ . The mobility of the electrons is reduced compared to  $\text{RhO}_2$  as has been proven by conductivity measurements. The magnetic behavior and the conductivity measurements of  $\text{Ag}(\text{Li}_{1/3}\text{Ir}_{2/3})\text{O}_2$  are conclusive with those of  $\text{Ag}(\text{Li}_{1/3}\text{Rh}_{2/3})\text{O}_2$ .

In  $\text{AgCoO}_2$  and the corresponding  $\text{AgRhO}_2$ , TIP (temperature independent paramagnetism) in correspondence with reported data for similar compounds has been observed.



#### 4.2. Cesium doped barium bismuthate – literature overview and motivation

BaBiO<sub>3</sub> belongs to the perovskite structural family. The eponymous mineral CaTiO<sub>3</sub> is named after the Russian politician and mineralogist Lev Alexejevitsch Perovski. Perovskite is a mineral with the chemical formula CaTiO<sub>3</sub>, where the Ca and O – atoms build the cubic closed packing, the Ca – atoms are located in the middle of the cubic cell with a coordination number of 12. The natural compound is slightly distorted and the ideal structure is found for SrTiO<sub>3</sub>. For compounds with general formula ABC<sub>3</sub>, a factor  $t$ , which defines the stability range, given by the equation 4.2.1 can be used, where  $r$  is the ionic radii:

$$t = \frac{r(A) + r(B)}{\sqrt{2}[r(C) + r(B)]} \quad (4.2.1)$$

In case of the ideal cubic structure  $t = 1$ . For  $0.89 < t < 1$  the structure is stable, at values between  $0.8 < t < 0.89$  it shows slightly distortion, and below 0.8 another structural type is resulting. As far as the perovskite can not be specified as pure ionic compounds this tolerance factor is only a guiding value. The different derivatives of the perovskite structure type can be classified in a concise manner using the group-subgroup relations<sup>137</sup>. To the first family tree belong perovskite structures with tilted coordination octahedra, Jahn-Teller distortion or atoms shifted from the octahedral centers. A second family of subgroups, where the perovskite sites split into different independent sites, results from structures with atom substitutions. In addition substitution and distortions can be combined in adequate subgroups.

After the first synthesis of BaBiO<sub>3</sub> in 1963 by R. Scholder et al.<sup>138</sup> the oxidation state of Bi cations has been a matter of continuous interest. The elements from the 5th main group have the following electron configuration [Xe]4f<sup>14</sup>5d<sup>10</sup>6s<sup>2</sup>6p<sup>3</sup> and therefore they should form compounds with 3+ and 5+ oxidation states, which they actually do, simulating the 4+ state. The controversy had become even more challenging after discovery of the superconductivity in the system BaBiO<sub>3</sub> - BaPbO<sub>3</sub><sup>139</sup>. Some authors believed<sup>139, 140</sup> and tried to provide proofs that the compound contains Bi<sup>4+</sup>, others<sup>141, 142</sup> have assumed that the mixed – valent situation Ba<sub>2</sub>Bi<sup>3+</sup>Bi<sup>5+</sup>O<sub>6</sub> is more appropriate, because in the monoclinic crystal structure, stable at room temperature, two distinct Bi sites, characterized by Bi – O distances of 2.12 and 2.28 Å are found<sup>142</sup>. It is not worth to argue about the Bi valency count only on the X-ray diffraction or Mössbauer spectroscopy, because of the insufficient oxygen position accuracy. In fact, BaBiO<sub>3</sub> is the first example of an A<sub>2</sub>B $\overset{\cdot}{B}$ B $\overset{\cdot}{B}$ O<sub>6</sub> – type perovskite in which the ordered  $B$ -site ions are the same element. There is also a phase transition from the stable monoclinic room temperature

form into a rhombohedral form at 405 K and finally to cubic at 750-800 K<sup>143</sup> and the relation between them can be seen on Figure 4.2.1.

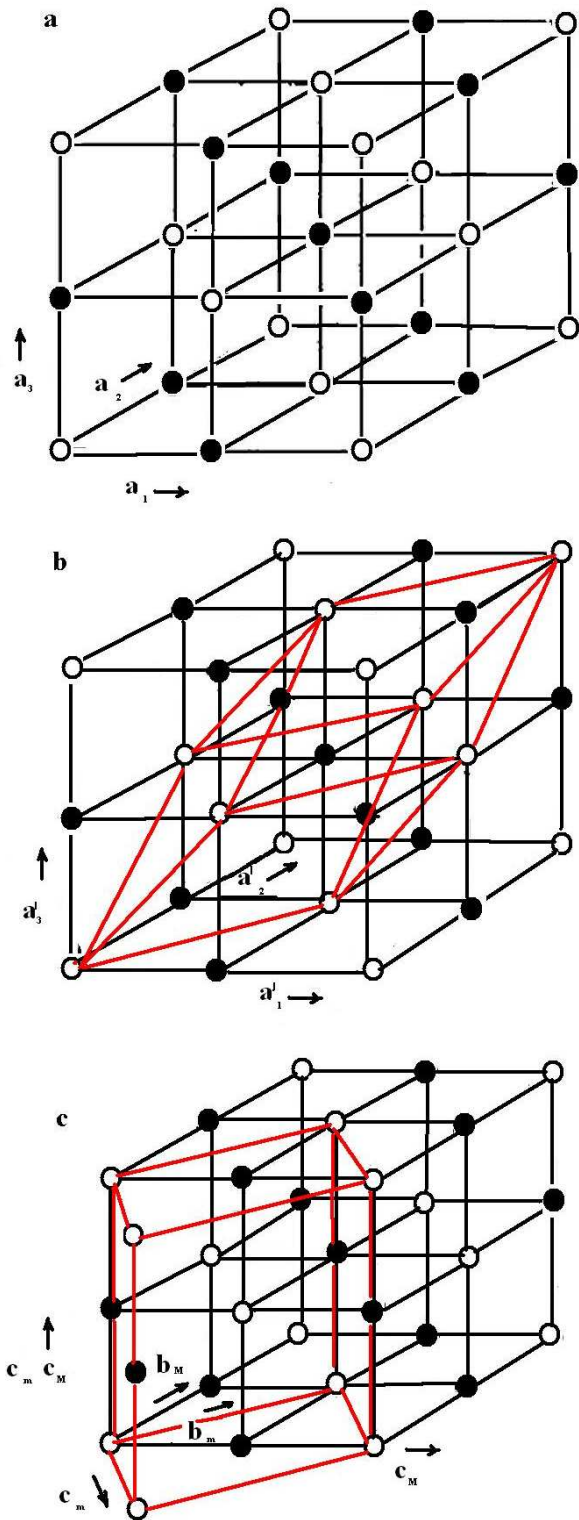


**Figure.4.2.1**

Relationship between the doubled ( $2a_0$ ) face – centered cells and the simpler cell described in the text. Closed and open circles are  $B$  and  $B'$  atoms in (a)  $Fm3m$ , Simple perovskite cell with edge  $a_0$  is shown in red outline. (b)  $R-3$  (facecentered) Primitive  $R-3$  ( $a_r \approx a_0\sqrt{2}$ ,  $a_2 \approx 60^\circ$ ) is shown in red outline, (c)  $F2/m$ . Body-centered  $I2/m$  cell ( $a_m \approx b_m \approx a_0\sqrt{2}$ ,  $c_m = 2a_0$ ,  $\beta \approx 90^\circ$ ) is shown in red outline.

More than 40 years after the first synthesis of  $\text{BaBiO}_3$  the questions of oxidation state of Bi and the structure are satisfactory clarified: Bi exists in mixed 3+ and 5+ state which leads to unexpected and remarkable physical properties when doped with K, Rb or Pb. The sum formula is given by  $\text{Ba}_{1-x}\text{A}_x\text{BiO}_3$  and  $\text{BaPb}_{1-x}\text{Bi}_x\text{O}_3$ , where A is alkali metal in particular K or Rb. The structural distortion with or without transition, may generate properties ranging from semiconducting to superconducting behavior<sup>138, 144-148</sup>.

If one tries to summarize the important experimental studies about  $\text{BaBiO}_3$ ,  $\text{Ba}_{1-x}\text{K}_x\text{BiO}_3$  and  $\text{BaPb}_{1-x}\text{Bi}_x\text{O}_3$  the following conclusions can be stated:

- $\text{BaBiO}_3$  is an insulator
- The alloys exhibit a metal-semiconductor transition as the concentration of the dopant (Pb,K) is varied<sup>138, 144</sup>.
- At all dopant concentrations these systems are diamagnetic<sup>144, 149, 150</sup>; the semiconducting phases are not Mott insulators.
- In their semiconducting phases they exhibit two energy gaps<sup>144, 151, 152</sup>.
- The semiconducting phases of the  $\text{BaPb}_{1-x}\text{Bi}_x\text{O}_3$  are examples for charge-density-wave ordering<sup>142, 144, 153-155</sup>.
- The alloys undergo various structural transitions as function of x (the concentration of dopant) and the temperature  $T$ <sup>142, 154, 156, 157</sup>.
- Both  $\text{Ba}_{1-x}\text{K}_x\text{BiO}_3$  and  $\text{BaPb}_{1-x}\text{Bi}_x\text{O}_3$  are type-II superconductors with 3-5 times higher  $T_c$  than those for the other three-dimensional oxide with similar density of state at the Fermi level<sup>144, 158-161</sup>.

As already mentioned, the barium bismuthate structure can be obtained from slight distortions of an underlying cubic perovskite structure. The corners of the cubic unit cell are occupied by Bi (Pb), O atoms are face centred and the biggest Ba (K) atoms are in a body centered arrangement. The Bi atoms are octahedrally coordinated by O atoms. Slight rotation and breathing-mode distortions of these octahedra lead to a variety of noncubic structures. In the case of pure  $\text{BaBiO}_3$  two distinct distances are found, explained with contraction in the oxygen octahedra around one of the Bi sublattices and expansion in the octahedra of those around the other one. Tilts of the oxygen octahedra lower further the symmetry of the  $\text{BaBiO}_3$  structure, therefore the rich phase variety of the doped bismuthates is not a surprise. The phase diagrams of  $\text{Ba}_{1-x}\text{K}_x\text{BiO}_3$  and  $\text{BaPb}_{1-x}\text{Bi}_x\text{O}_3$  are shown on Figure 4.2.2.

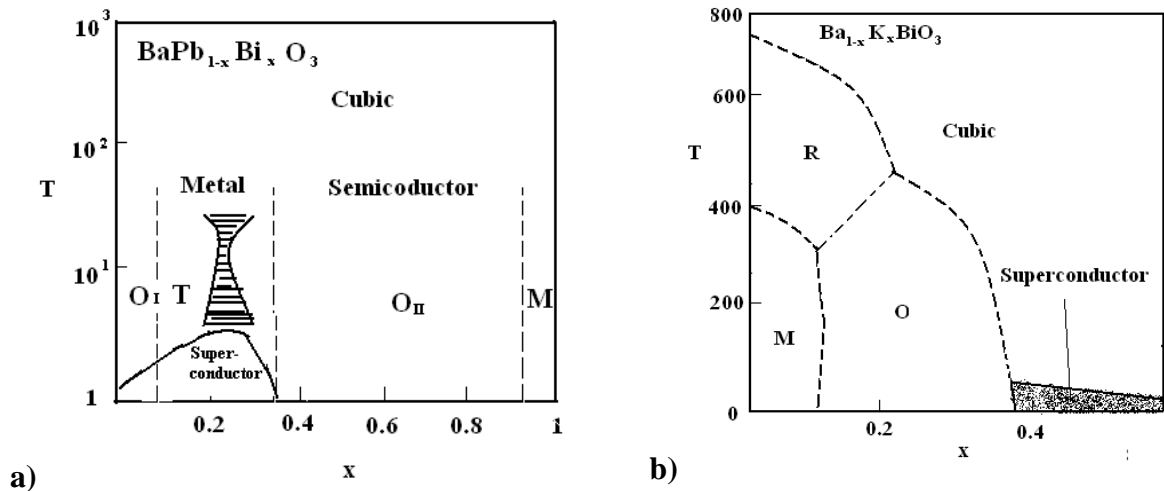


**Figure 4.2.2.** Schematic phase diagram of **a)**  $\text{BaPb}_{1-x}\text{Bi}_x\text{O}_3$ <sup>162</sup> and **b)**  $\text{Ba}_{1-x}\text{K}_x\text{BiO}_3$ <sup>163, 164</sup>.

In case of  $\text{BaPb}_{1-x}\text{Bi}_x\text{O}_3$ <sup>162</sup> (Figure 4.2.2a) the orthorhombic ( $\text{O}_I$ ) and tetragonal (T) phase show metallic behavior at higher temperature and superconductivity at low temperatures and a doping rate up to  $x = 0.2$ . The orthorhombic ( $\text{O}_{II}$ ) and monoclinic (M) phases are semiconducting, the nature of metal – semiconductor transition is not clear, but here it is shown as first – order transition indicating a region of two – phase coexistence. All the four phases undergo high – temperature structural transition to the cubic phase. In previous studies of Pb-doped compounds<sup>138</sup> it was suggested that superconductivity could only occur in the tetragonal phase. However, subsequent work shows that it could be obtained in specimens with orthorhombic symmetry<sup>144</sup>, too. In case of Ba site doping  $\text{Ba}_{1-x}\text{K}_x\text{BiO}_3$ <sup>163, 164</sup> (Figure 4.2.2b) the entire cubic phase is metallic and the low temperature region (hatched) is a superconducting phase. The monoclinic (M), rhombohedral (R) and orthorhombic (O) regions are semiconducting. In K-doped compounds the superconductivity has been observed only in the cubic phase<sup>154, 156, 165</sup>. From the available experimental data it is not clear whether the superconducting and semiconducting phases coexist along any phase boundary, if so, what the order of the transition along this boundary is<sup>144</sup>. However, the maximum value of the superconducting  $T_c$  seems to occur at the nearly the same x-value as the metal – semiconductor transition. The relation between the doping rate x and the cell parameter in the tree systems  $\text{Ba}_{1-x}\text{K}_x\text{BiO}_3$ <sup>166</sup>,  $\text{Ba}_{1-x}\text{Rb}_x\text{BiO}_3$ <sup>167</sup> and  $\text{BaPb}_{1-x}\text{Bi}_x\text{O}_3$ <sup>138</sup> are shown on a Figure 4.2.3. As it is expected the cell parameters  $a$  decreases linear with the increasing of the dopant concentration – K, Rb or Pb. In the case of Rb the authors<sup>167</sup> do not report dependence in between the transition temperature  $T_c$  and the doping rate while in the K and Pb doped systems

systematic<sup>138, 166</sup>. Increasing the dopant in some extends led to increasing the critical temperature and before and afterword became normal semiconducting materials.

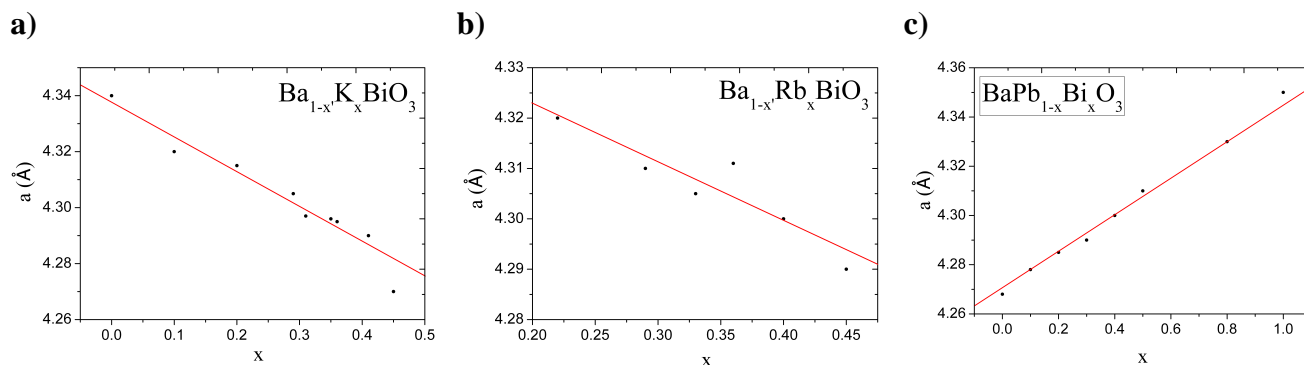
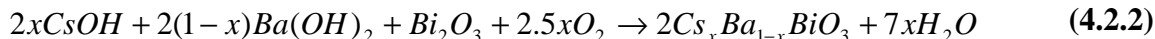


**Figure 4.2.3.** Diagram of the relation between doping rate and the cell parameters in the systems: **a)**  $\text{Ba}_{1-x}\text{K}_x\text{BiO}_3$ <sup>166</sup>, **b)**  $\text{Ba}_{1-x}\text{Rb}_x\text{BiO}_3$ <sup>167</sup> and **c)**  $\text{BaPb}_{1-x}\text{Bi}_x\text{O}_3$ <sup>138</sup>.

There are different reasons, why part of this thesis is devoted to investigations on  $\text{BaBiO}_3$  system. Different types of carrier – doped compounds based on it have been reported, e.g. example for hole – doped compound is  $\text{Ba}_{1-x}\text{K}_x\text{BiO}_3$ <sup>158</sup> showing superconductive behavior or for electron – doped  $\text{Ba}_{1-x}\text{Bi}_x\text{BiO}_3$ <sup>168</sup> being an insulator. Numbers of papers concerning the physical properties, mainly the superconductivity of  $\text{Ba}_{1-x}\text{K}_x\text{BiO}_3$  system are available. The aim of that work was a new hole – doped compound to be synthesis through the partial substitution of  $\text{Cs}^+$  for  $\text{Ba}^{2+}$  in the  $\text{BaBiO}_3$ . The stability and the phase diagram of  $\text{Cs}_x\text{Ba}_{1-x}\text{BiO}_3$  as well as the dependence of the structural and electronic properties as function of the doping level were also planned.

#### 4.2.1. Synthesis of Cs doped BaBiO<sub>3</sub>.

Reaction equation for synthesizes of Cs<sub>x</sub>Ba<sub>1-x</sub>BiO<sub>3</sub>:



The precise calculated molar ratio of the starting mixture was 1.6242 g Ba(OH)<sub>2</sub>·8H<sub>2</sub>O (Alfa Aeser 98 %) 1.153 g CsOH·H<sub>2</sub>O (Aldrich 99 %) in 100 % excess and 2 g Bi<sub>2</sub>O<sub>3</sub> (Alfa Aeser 99 %). Two-electrode electrolysis was used for the synthesis. This method is based on the application of constant current of potential on the electrodes. 20 g of CsOH·H<sub>2</sub>O was used instead of the calculated amount executing the role of liquid media, which enables the ion transport. The stoichiometric amount of the starting materials was intimately mixed and homogenized in a mortar, placed in a corundum crucible, which was finally inserted in a glass/quartz tube according to the temperature. The system was heated to a default temperature, stirred with a magnet stirrer and hold for 2h at this reaction conditions allowing the flux to equilibrate. The cyclic voltammogram (CV) tests were carried out by electrochemical station (VMP multipotentiostat) at 0.2 mV·s<sup>-1</sup> between 0 and 0.8 V. The CV have been obtained in CsOH – Ba(OH)<sub>2</sub> – Bi<sub>2</sub>O<sub>3</sub> solution shown in Figure 4.2.4. The first peak occurs around 0.52 V vs. OCV is most probably oxidation of Bi<sup>3+</sup>/Bi<sup>5+</sup>, whereas the origin of the second one is not clearly defend but could be oxygen elimination. After 3 cycles the potentiostatic regime was mostly chosen, because of the less potential changes compared to the current fluctuation. Additionally constant current syntheses were also performed to study the difference. Technical details and selected reaction conditions are listed in Table 4.2.1.

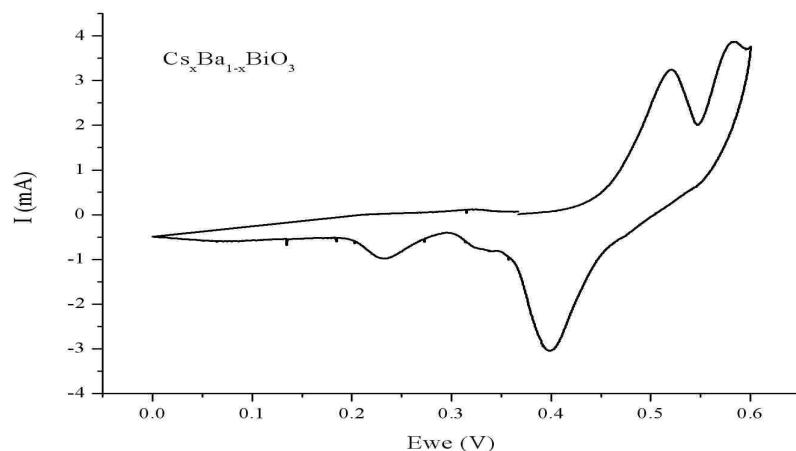


**Figure 4.2.4.** The CV of CsOH·H<sub>2</sub>O, Ba(OH)<sub>2</sub>·8H<sub>2</sub>O and Bi<sub>2</sub>O<sub>3</sub> flux at 543 K.

Table 4.2.1: Variable parameters of the synthesis process.

<b>Constant</b>	
<b>I, mA</b>	Galvanostatic 2-4
<b>or U, V</b>	Potentiostatic 0.4- 0.8
<b>Temperature, K</b>	493-773
<b>Reaction time, h</b>	24-96
<b>Starting mixture</b>	The ratio Cs:Ba:Bi

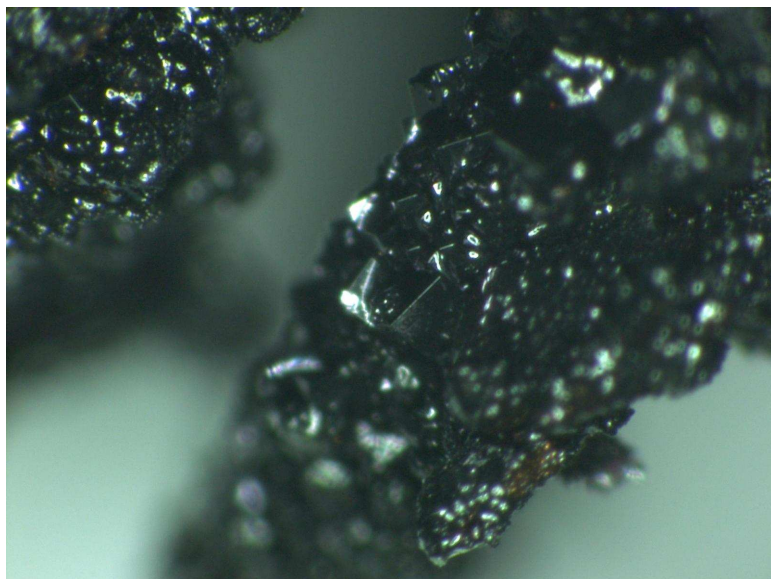


**Figure 4.2.5.** Crystals of  $\text{Cs}_x\text{Ba}_{1-x}\text{BiO}_3$  grown by electrolysis.

After a defined reaction time, the electrodes were removed from the flux. The anode was washed with water to remove any residual flux and dried at  $100^\circ\text{C}$ . The obtained product forms black cubic crystals and is stable towards air and water (Figure 4.2.5). As shown in Table 1 the synthesis conditions were varied to get higher doping rates of Cs, and find a possible superconducting behavior. More than 200 different experiments were carried out, were only one parameter was changed from the previous experiment studying its influence. Another problem which is caused by the system was the quantitative analysis of the product composition therefore a number of analytical techniques - EDX, AAS, ICP-OE were used, adding a small error in the analysis. In Table 4.2.2 some of the results are presented. The highest observed doping composition is  $\text{Cs}_{0.27}\text{Ba}_{0.76}\text{BiO}_3$ . In case of sample Pr16 and Pr38 two cubic phases with slightly different unit cells were refined by Rietveld method.

Table 4.2.2. Quantitative analysis (AAS and ICP), cell parameters and reaction conditions of selected experiments.

Sample	Ratio Cs:Ba	Cell Parameter (Å)	Reaction conditions: T (K), I/U=const, reaction time
Pr16	0.22:0.98*	4.2920(1) (4.3320(1))	513 K, 0.8 V, 48 h
Pr17	0.22:0.79	4.3436(1)	543 K, 0.6 V, 48 h
Pr26	0.18:0.82	4.3439(7)	543 K, 0.6 V, 48 h
Pr27	0.21:0.80	4.3417(5)	548 K, 0.6 V, 48 h
Pr28	0.25:0.76	4.3404(6)	553 K, 0.6 V, 48 h
Pr31	0.27:0.76	4.3427(3)	543 K, 0.6 V, 48 h
Pr36	0.23:0.81	4.3453(3)	543 K, 2 mA, 48 h
Pr38	0.15:0.93*	4.2829(9) (4.3453(3))	543 K, 2 mA, 48 h
Pr41	0.19:0.82	4.3447(4)	773 K, 0.8 V, 48 h
Pr42	0.14:0.85	4.3454(4)	773 K, 0.8 V, 48 h

\* Two reaction products in the same sample

After finding the optimal ratio of starting materials (20 g CsOH·H<sub>2</sub>O, 2g Ba(OH)<sub>2</sub>·8H<sub>2</sub>O, and 1.6 g Bi<sub>2</sub>O<sub>3</sub>), the influence of the temperature and duration was studied. It was found that the duration of the electrolysis does not change dramatically the doping rate, whereas the temperature change shows a significant effect. The Cs rate in the BaBiO<sub>3</sub> decreases with increase in the temperature. Therefore there were some experiments in which after the melting of the reacting mixture, the temperature was decreased. They were unfortunately not successful at temperature lower than 473 K, because the mixture starts to solidify.



#### 4.2.2. Structural characterization of Cs doped BaBiO<sub>3</sub>

The crystals were carefully scratched from the electrode and placed in a Petri dish. They are air and moisture stable and therefore the mounting on the capillary was made under the light microscope outside the dry box. The measurement was performed with graphite-monochromated MoK $\alpha$  radiation ( $\lambda=0.71073$  Å) on a Smart APEX I Diffractometer. The crystallographic parameters are presented in Table 4.2.3 and 4.2.4.

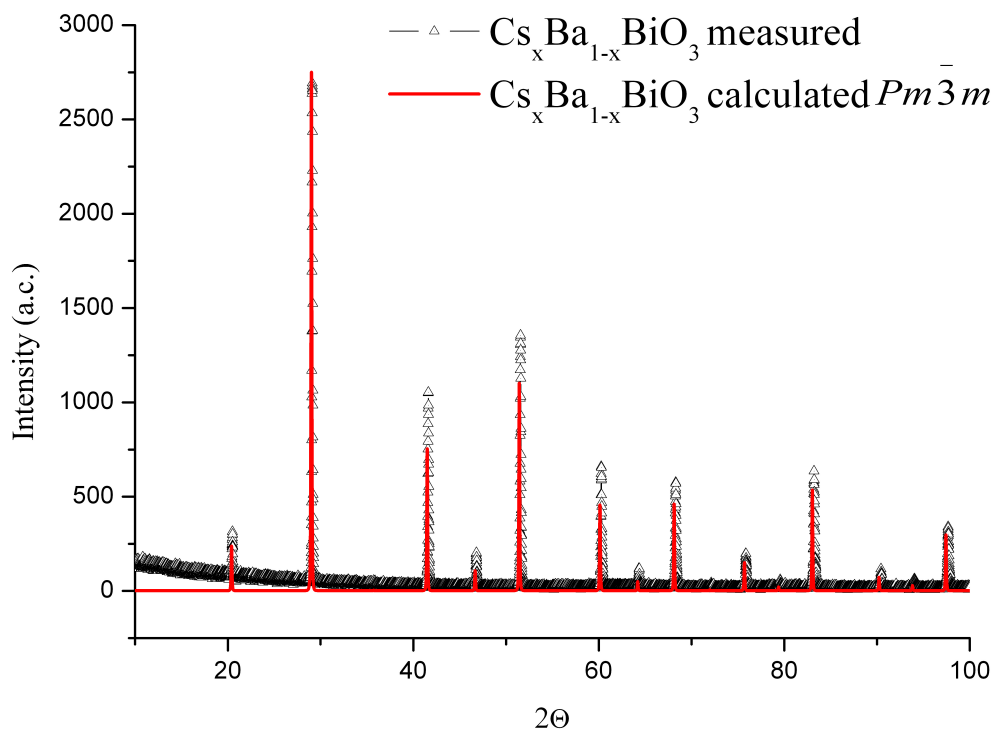
Table 4.2.3. Crystal data and structure refinement of Cs<sub>0.25</sub>Ba<sub>0.75</sub>BiO<sub>3</sub>.

Empirical formula	Cs <sub>0.25</sub> Ba <sub>0.75</sub> BiO <sub>3</sub>
Formula weight	393.21
Temperature, K	273(2)
Wavelength, Å	0.71073
Crystal system	cubic
Space group	$Pm\bar{3}m$ (221)
Unit cell dimensions, Å	$a = 4.3490(5)$
Volume, Å <sup>3</sup>	82.256(16)
Z	1
Density (calculated), mg/m <sup>3</sup>	7.938
Absorption coefficient, mm <sup>-1</sup>	64.895
$F(000)$	163
Theta range for data collection	4.69 to 29.80°.
Index ranges	-6<= $h$ <=6, -6<= $k$ <=6, -6<= $l$ <=6
Reflections collected	1002
Independent reflections	42 [ $R(\text{int}) = 0.0468$ ]
Completeness to theta = 29.80°	100.0 %
Refinement method	Full-matrix least-squares on $F^2$
Data / restraints / parameters	42 / 1 / 8
Goodness-of-fit on $F^2$	1.259
Final $R$ indices [ $I > 2\sigma(I)$ ]	$R1 = 0.0138$ , $wR2 = 0.0304$
$R$ indices (all data)	$R1 = 0.0138$ , $wR2 = 0.0304$
Extinction coefficient	0.189(15)
Largest diff. peak and hole, e.Å <sup>-3</sup>	1.128 and -1.234

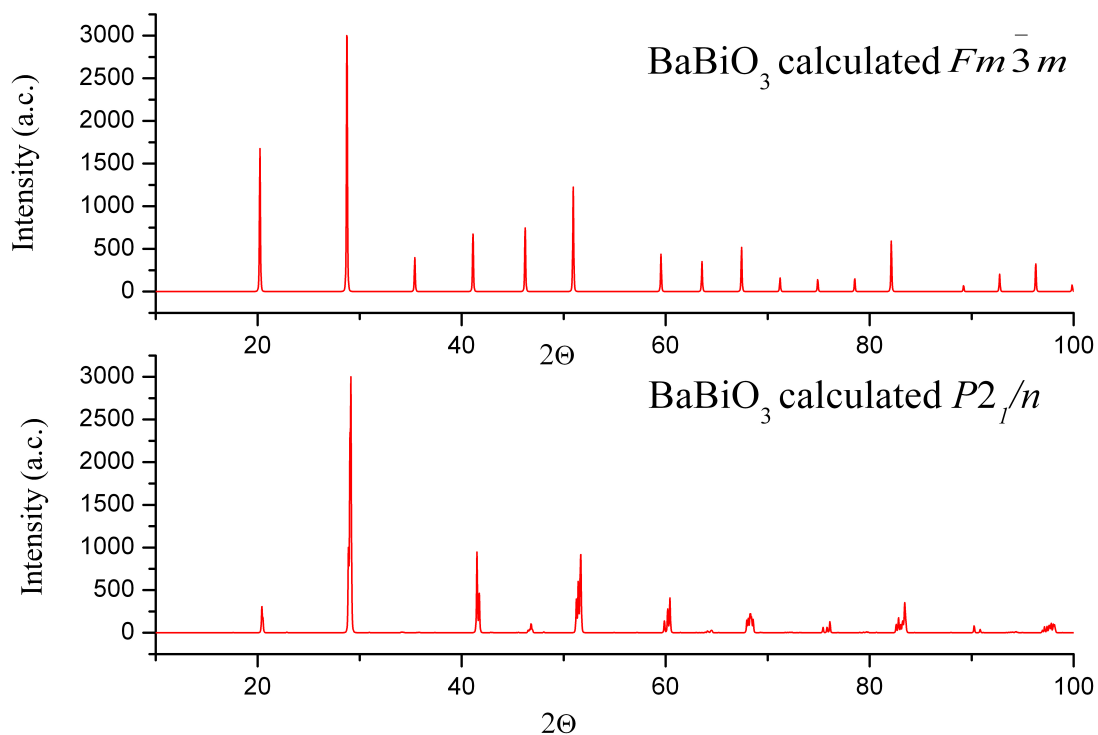
Table 4.2.4: Atomic coordinates and anisotropic displacement factors of  $\text{Cs}_{0.25}\text{Ba}_{0.75}\text{BiO}_3$ , the occupancy of Ba and Cs is refined coupling their sum of 1.

Atom	Wyckoff Position	Occ.	x	y	z	$U_{11}$	$U_{22}$	$U_{33}$
Bi (1)	1a	1	0	0	0	0.0014(3)	0.0014(3)	0.0014(3)
Ba (1)	1b	0.75	1/2	1/2	1/2	0.0062(3)	0.0062(3)	0.0062(3)
Cs (1)	1b	0.25	1/2	1/2	1/2	0.0062(3)	0.0062(3)	0.0062(3)
O(1)	3d	1	1/2	0	0	0.0129(7)	0.0497(3)	0.0497(3)

The structure was solved using the software package SHELXTL by direct methods; all heavy atoms were found during solving process. The positions of the oxygen atoms were found during the refinement, using least-squares method. The compound is isostructural with Rb and K doped bariumbismuthates and crystallizes in the cubic space group  $Pm-3m$  (no. 221) with  $z = 1$  and  $a = 4.3490(5) \text{ \AA}$ , building a perovskite like type of structure. The bismuth atoms are occupying the origin instead of the Ti atoms in the mineral Perovskite; Ba and Cs are located on the same crystallographic site, namely the center of the elementary cell and the oxygen atoms are situated on the half of the cell edges. The result shows that the symmetry of the Cs doped compound is reduced compared to the typical symmetry for  $\text{BaBiO}_3$  with  $Fm-3m$  (no. 225),  $Z = 8$  and  $a = 8.7759(2) \text{ \AA}$ . The explanation therefore is that in the undoped bariumbismuthates the mixed - valent Bi-atoms ( $\text{Bi}^{3+}$  and  $\text{Bi}^{5+}$ ) are ordered, building a cubic face centered bravais lattice. In the case of  $\text{Cs}_{0.25}\text{Ba}_{0.75}\text{BiO}_3$ , the ratio between  $\text{Bi}^{3+}$  and  $\text{Bi}^{5+}$  is no longer equal, due to the electron deficiency caused by the exchange of  $\text{Ba}^{2+}$  against  $\text{Cs}^+$ , the amount of  $\text{Bi}^{5+}$  is increasing. This takes place on a statistical manner and leads to the reduction of the lattice constant, the bravais lattice becomes primitive. This is an expected phenomena compared to the well known superconductive K doped  $\text{BaBiO}_3$ . The powder diffractograms of doped ( $Pm-3m$ ) and undoped ( $Fm-3m$ )  $\text{BaBiO}_3$  are quite different<sup>143</sup>, as it could be seen on Figure 4.2.6.



a)



b)

**Figure 4.2.6.** a) Calculated and measured powder pattern of  $\text{Cs}_{0.27}\text{Ba}_{0.73}\text{BiO}_3$ , b) Calculated pattern of undoped  $\text{BaBiO}_3$ , high temperature cubic phase ( $Fm\bar{3}m$ ) and the stable monoclinic ( $P2_1/n$ ) room temperature phase<sup>143</sup>.

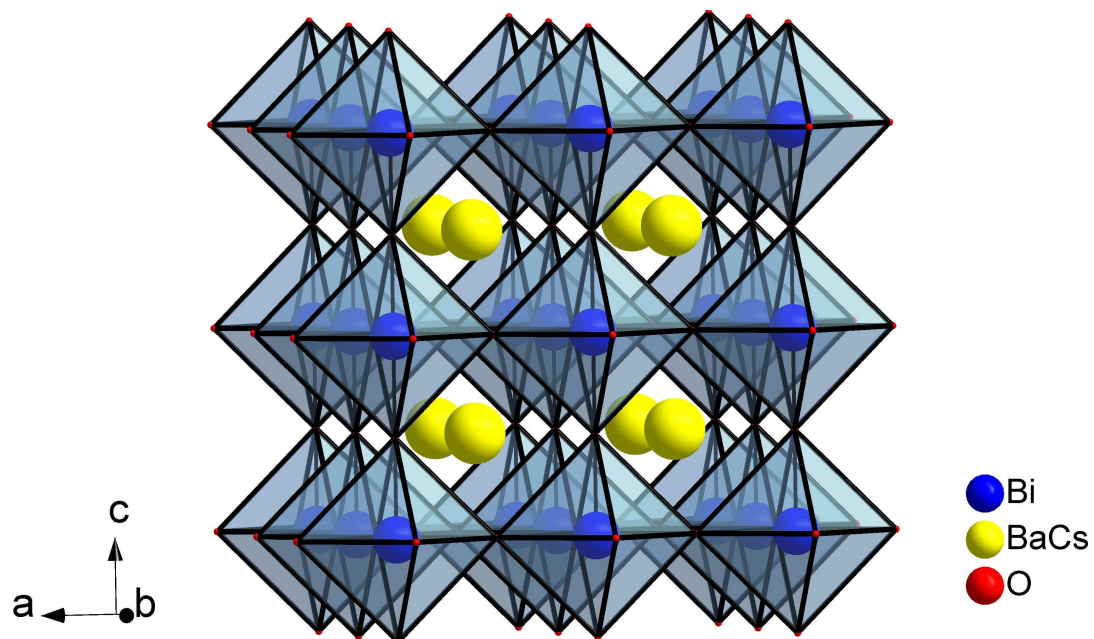
In the  $\text{Cs}_{0.25}\text{Ba}_{0.75}\text{BiO}_3$  the Ba/Cs and O atoms form a cubic closed packing, with octahedral coordinated Bi-atoms and bond angles Bi – O – Bi equal to  $180^\circ$  (Figure 4.2.7 a). The Ba-atoms are surrounded by 12 oxygen atoms forming an ideal cuboctahedron (Figure 4.2.7 b). To distinguish  $\text{Cs}^+$  and  $\text{Ba}^{2+}$  by X-Ray techniques is not possible because of the same electron configuration ( $[\text{Xe}]6s^0$ ) resulting by the neighboring position in the periodic system of elements. To get a stable refinement the anisotropic displacement factors for  $\text{Cs}^+$  and  $\text{Ba}^{2+}$  were linked and the occupancy of the same crystallographic positions was set equal to one. The structural refinement and the obtained parameters are presented in Table 4.2.3 and Table 4.2.4. The bond length in  $\text{BaBiO}_3$  and in the doped compounds  $\text{K}_{0.4}\text{Ba}_{0.6}\text{BiO}_3$  and  $\text{Cs}_{0.27}\text{Ba}_{0.76}\text{BiO}_3$  are in the same range (Table 4.2.5).

Table 4.2.5. Bond length comparison of  $\text{BaBiO}_3$  and  $\text{K}_{0.4}\text{Ba}_{0.6}\text{BiO}_3$ /  $\text{Cs}_{0.27}\text{Ba}_{0.76}\text{BiO}_3$ .

Compound	Bond	Bond length (Å)
$\text{BaBiO}_3$	Bi1 - O	2.2282/2.2886*
	Bi2 - O	2.1581/2.0956*
	Ba - O	3.1018/3.1016*
$\text{K}_{0.4}\text{Ba}_{0.6}\text{BiO}_3$	Bi - O	2.1217
	Ba - O	3.000
	K - O	3.000
$\text{Cs}_{0.27}\text{Ba}_{0.76}\text{BiO}_3$	Bi - O	2.1745
	Ba - O	3.075
	Cs - O	3.075

\* Different records in the database

a)



b)

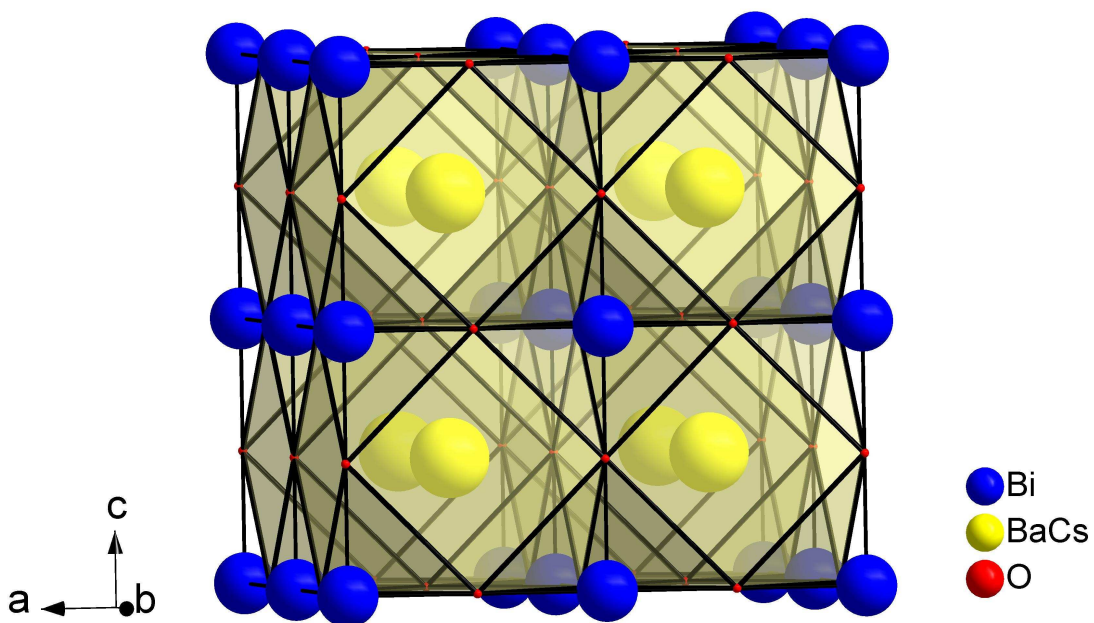


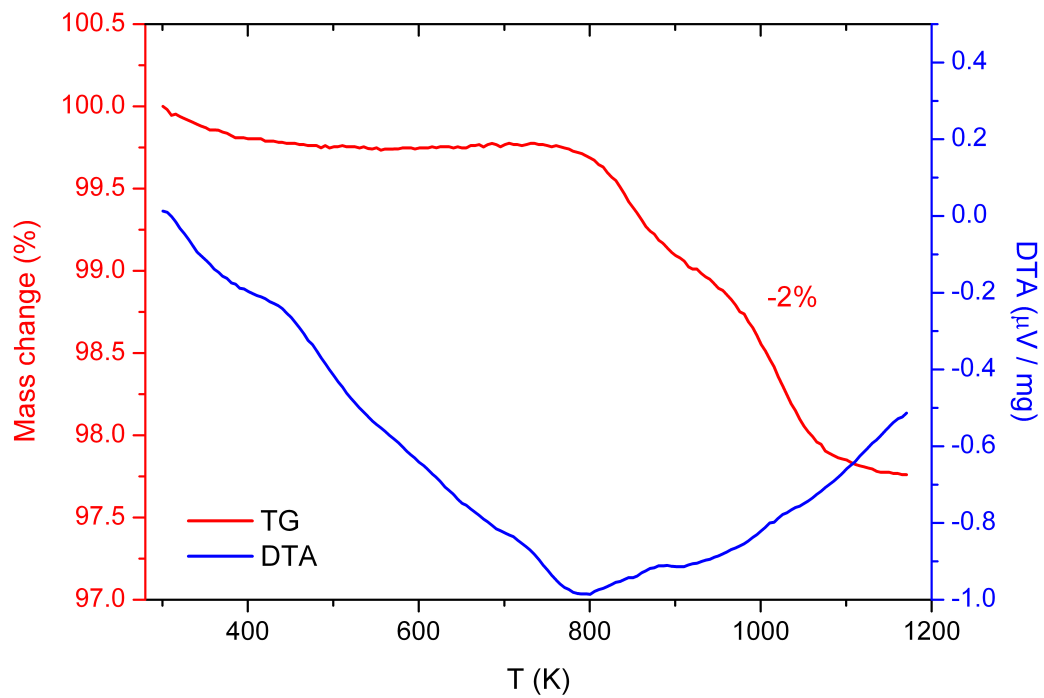
**Figure 4.2.7.** Crystal structure of  $\text{Cs}_{0.25}\text{Ba}_{0.75}\text{BiO}_3$ . a) Octahedral coordinated Bi; b) Cuboctahedral coordination of Ba and Cs.

### 4.2.3. Physical characterization of Cs doped BaBiO<sub>3</sub>

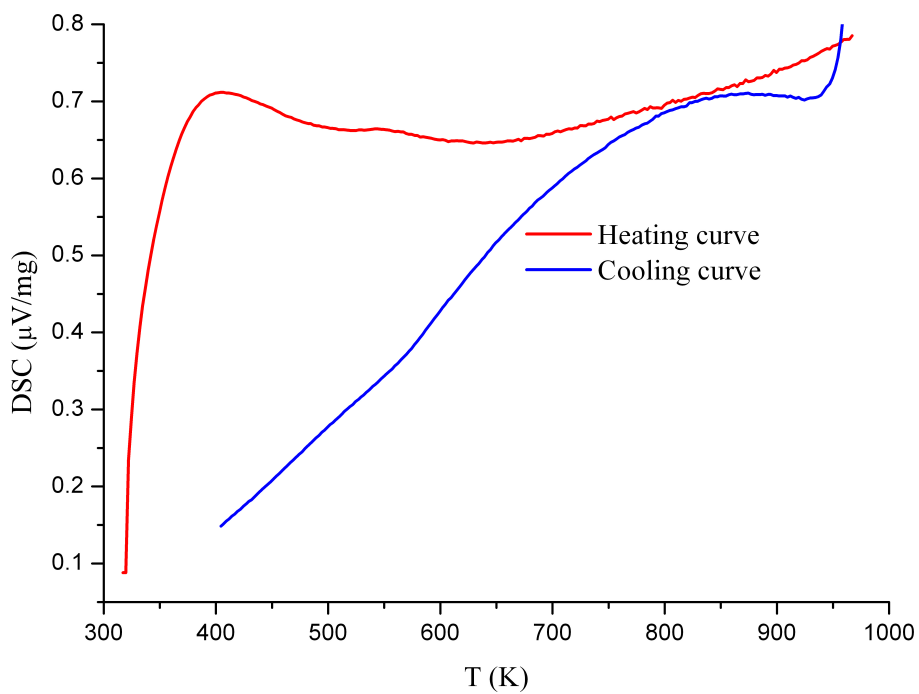
#### *Thermal stability*

The thermal stability of the compound was investigated using DTA/TG and DSC measurements. In DTA/TG experiments 20 mg of the sample were placed in a Al<sub>2</sub>O<sub>3</sub> crucible and heated up with 5 K/min under dynamic argon atmosphere from 298 to 1173 K. It was found that the sample is stable up to 770 K. After that temperature the sample loses slightly oxygen (~2 wt%) (Figure 4.2.8 a).

The DSC measurement was performed in the temperature range from 298 to 973 K with a heating rate of 20 K/min and 20 min holding time at the final temperature. The crucible material used was Al<sub>2</sub>O<sub>3</sub>. Up to 770 K no phase transition could be observed (Figure 4.2.8.b). Although the DSC curve did not show any transitions, a comparison between powder patterns of the sample at room temperature and after heating showed a shift in peak positions (Figure 4.2.9). The shift direction to smaller  $2\theta$  values is an indication of lattice constant increase. The cell parameters were determined by LeBail fit, the resulting values are  $a = 4.3394(1)$  Å for the room temperature sample and  $a = 4.36595(22)$  Å for the heated sample. The increase of the lattice constant is caused by reduction of Bi<sup>5+</sup> to Bi<sup>3+</sup> in accordance with oxygen loss of approximately 2 wt% detected by TG – DTA. If a formal charge of Bi in Cs<sub>0.27</sub>Ba<sub>0.73</sub>BiO<sub>3</sub> is calculated it is +4.17 (0.415 Bi<sup>3+</sup> and 0.585 Bi<sup>5+</sup>), which decreases in the sample after heating to +3.17 (0.915 Bi<sup>3+</sup> and 0.085 Bi<sup>5+</sup>). As far as this process does not occur at a defined temperature but in a hole region, without significant energy change there is no sharp peak in the DSC curve.



a)



b)

**Figure 4.2.8.** a ) DTA/TG measurement of  $\text{Cs}_{0.27}\text{Ba}_{0.73}\text{BiO}_3$ , b) DSC measurement of  $\text{Cs}_{0.27}\text{Ba}_{0.73}\text{BiO}_3$ .

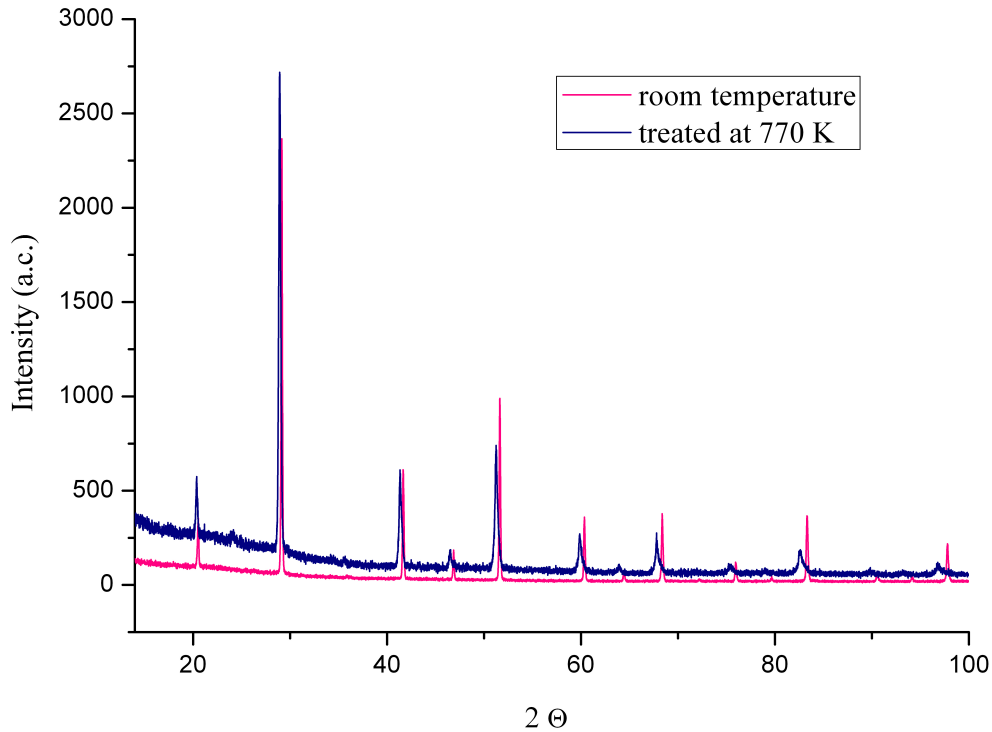


**Figure 4.2.9.** Powder pattern of  $\text{Cs}_{0.27}\text{Ba}_{0.73}\text{BiO}_3$  at room temperature and after heated up to 770 K

### *Electrical Conductivity*

The electronic conductivity was measured on powder sample, in the temperature range from 7 to 300 K, using the four point method. The resistivity of the material up to 80 K is on the sensitivity limits of the set up, decreasing after that from  $4.8 \cdot 10^7$  to  $1.6 \cdot 10^3$  ( $\Omega \cdot \text{cm}$ ). At the same time the conductivity increases with the temperature, indicating a typical semiconductor behavior (Figure 4.2.10). The conductivity at ambient temperature is  $5.54 \cdot 10^{-4} \Omega^{-1} \cdot \text{cm}^{-1}$ . An expression for the conductivity is:

$$\sigma = nZ_e\mu, \quad (4.2.3)$$

$\sigma$  is the conductivity,  $n$ - number of charge carriers per unit volume,  $Z_e$  their charge and  $\mu$  is their mobility (measured velocity in the electric field). The measured curve shows an intrinsic semiconductor behavior. Typical for these solids is that conduction can only occur if electrons are promoted to the conduction band. The current in the semiconductors will depend of  $n$ , which is the number of electrons free to transport charge. The number of  $e^-$  able to transport



charge is given by the number promoted to the conduction band plus the number of  $e^-$  in the valence band that have been freed to move by this promotion. The number of  $e^-$  varies with the temperature in an exponential manner so that small differences in band gap lead to large difference in the number of electrons promoted and hence the number of current carriers.

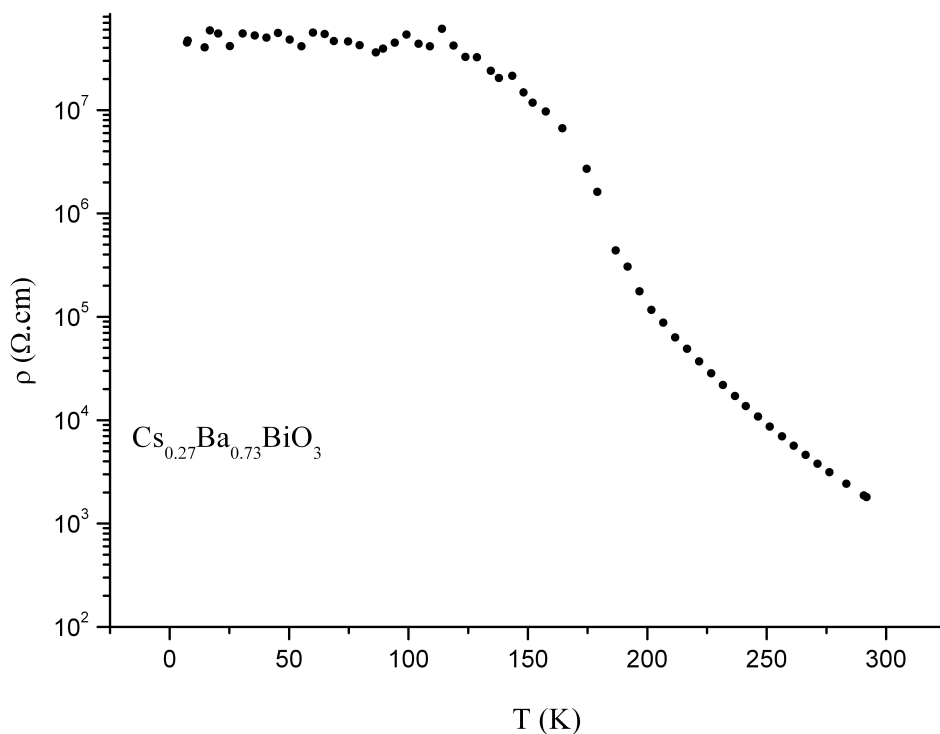


**Figure 4.2.10.** Temperature dependence of mean resistivity and conductivity of  $\text{Cs}_{0.27}\text{Ba}_{0.73}\text{BiO}_3$ .

### *Magnetic Susceptibility*

The response of the  $\text{Cs}_x\text{Ba}_{1-x}\text{BiO}_3$  on different magnetic fields and at different temperatures was studied. The sample was placed in a gelatin capsule and treated in a temperature range from 3 to 300 K with fields of 0.001 - 7 T.  $\text{Cs}_{0.27}\text{Ba}_{0.73}\text{BiO}_3$  shows diamagnetic behavior. Like in the pure  $\text{BaBiO}_3$ ,  $\text{Cs}_x\text{Ba}_{1-x}\text{BiO}_3$  exhibits  $\text{Bi}^{3+}$  and  $\text{Bi}^{5+}$  with electronic configurations  $[\text{Xe}] 4f^{14}5d^{10}6s^2$  and  $[\text{Xe}] 4f^{14}5d^{10}$  (close shell systems) respectively. Diamagnetism is regarded as a weak effect and is a form of magnetism that is only exhibited by a substance in the presence of an externally applied magnetic field. The diamagnetic compounds ‘dilute’ the line of applied magnetic flux and the superconductors can exclude them completely. The mol magnetic susceptibility at 1 T of the target compounds it shown in Figure 4.2.11.

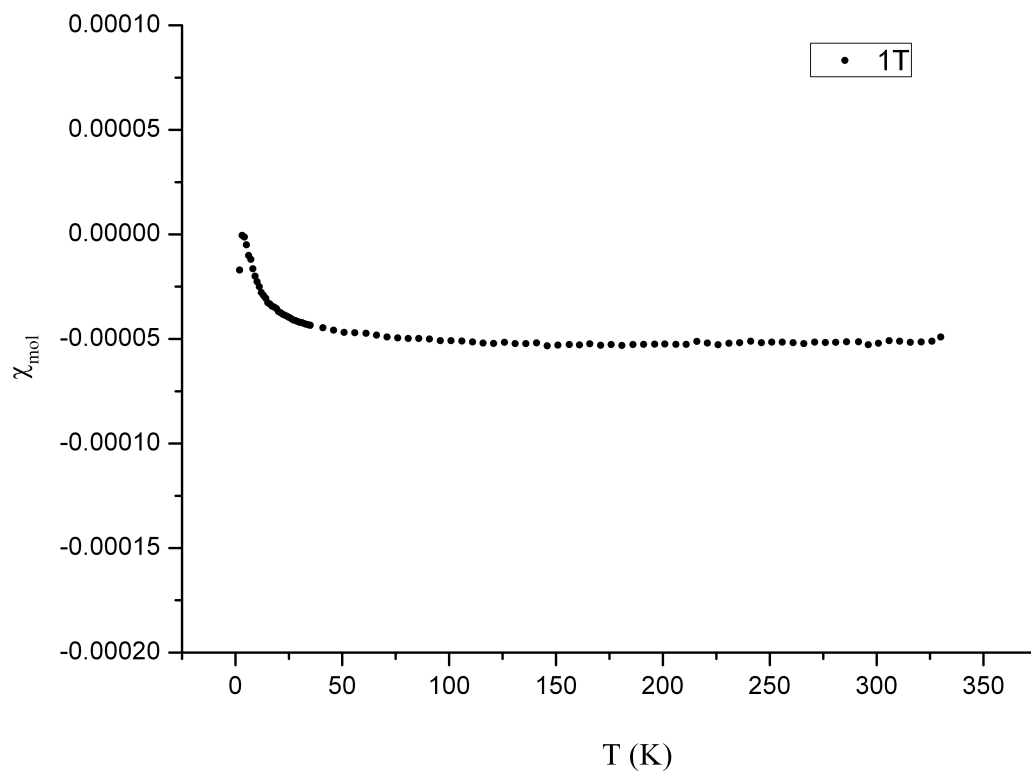


**Figure 4.2.11.** Magnetic susceptibility of  $\text{Cs}_x\text{Ba}_{1-x}\text{BiO}_3$ .

### 4.1.3. Concluding remarks

The influence of different synthesis parameters on the Cs doping was studied. It has been found that carrying out the experiments at potentiostatic mode induces more constant conditions, no jumps or shifts in the CV – curves, compare to the galvanostatic mode. Carrying out the experiments under described conditions, as well as changing the molar ratio between the reactants (+/- 10 %), did not have an impact on the doping level. It was found that the temperature influence is significant, whereas the increases of the temperature decrease the level of doping. The problem of introducing Cs in the BaBiO<sub>3</sub> and varying the oxidation state Bi was more difficult to control. The valence state of the Bi in Cs<sub>x</sub>Ba<sub>1-x</sub>BiO<sub>3</sub> depends not only on the doping level of Cs (x) but also from the oxygen content. The phase purity in the synthesized compound causes another difficulty. Under different applied conditions (see Table 4.2.2 ) two phases could be obtained in the reaction product differing in the lattice constant a, caused by different Cs amounts in the phases. This indicates that there could be a gap in the solid solution of Cs<sub>x</sub>Ba<sub>1-x</sub>BiO<sub>3</sub>, or the doping of Cs and the crystal growth could not be fully controlled by the applied conditions.

The highest achieved doping level of Cs in BaBiO<sub>3</sub> was 0.27, higher than reported from the Japanese group<sup>169</sup> (0.22). No superconducting behavior could be observed and the electronic conductivity remains semiconducting.

## 5. References:

1. Boyd, G. E.; Schubert, J.; Adamson, A. W., The Exchange Adsorption Of Ions From Aqueous Solutions By Organic Zeolites.1. Ion-Exchange Equilibria. *Journal Of The American Chemical Society* **1947**, 69, (11), 2818-2829.
2. Schlogl, R.; Helfferich, F., Comment On The Significance Of Diffusion Potentials In Ion Exchange Kinetics. *Journal Of Chemical Physics* **1957**, 26, (1), 5-7.
3. Reichenberg, D., Properties Of Ion-Exchange Resins In Relation To Their Structure.3. Kinetics Of Exchange. *Journal Of The American Chemical Society* **1953**, 75, (3), 589-597.
4. Shin, Y. J.; Doumerc, J. P.; Dordor, P.; Delmas, C.; Pouchard, M.; Hagenmuller, P., Influence Of The Preparation Method And Doping On The Magnetic And Electrical-Properties Of Ag<sub>2</sub>O. *Journal Of Solid State Chemistry* **1993**, 107, (2), 303-313.
5. Otabe, T.; Ueda, K.; Kudoh, A.; Hosono, H.; Kawazoe, H., n-type electrical conduction in transparent thin films of delafossite-type AgInO<sub>2</sub>. *Applied Physics Letters* **1998**, 72, (9), 1036-1038.
6. Kleppa, O. J.; Clarke, R. B.; Hersh, L. S., Studies Of Fused Salts.3. Heats Of Mixing In Silver Nitrate-Alkali Nitrate Mixtures. *Journal Of Chemical Physics* **1961**, 35, (1), 175-&.
7. Otto, E. M., Equilibrium Pressures Of Oxygen Over Ag<sub>2</sub>O-Ag At Various Temperatures. *Journal Of The Electrochemical Society* **1966**, 113, (7), 643-&.
8. R.C.Weast, Handbook of chemistry and Physics. **1983-84**.
9. Rabenau, A., The Role Of Hydrothermal Synthesis In Preparative Chemistry. *Angewandte Chemie-International Edition In English* **1985**, 24, (12), 1026-1040.
10. Todheide, K., Wassrige Losungen Bei Hohen Drucken Und Temperaturen. *Berichte Der Bunsen-Gesellschaft Fur Physikalische Chemie* **1966**, 70, (9-10), 1022-&.
11. Todheide, K., Hydrothermal Solutions. *Berichte Der Bunsen-Gesellschaft-Physical Chemistry Chemical Physics* **1982**, 86, (11), 1005-1016.
12. Kozlov, V. K.; Kuznetsov, V. N.; Khodakovsky, I. L., Experimental-Study Of Thermodynamic Properties Of Ag<sub>2</sub>O And Hydroxocomplexes Of Silver(I) In Aqueous-Solutions Under High-Temperatures. *Geokhimiya* **1983**, (2), 215-227.
13. Franck, E. U., Uberkritisches Wasser Als Elektrolytisches Losungsmittel. *Angewandte Chemie-International Edition* **1961**, 73, (10), 309-&.
14. Bruker AXS. *Madison, WI, SAINT, Version 7.60A* **2008**.
15. *Stoe & Cie, Darmstadt. X-RED: Data reduction for STADI4 and IPDS V 1.22*. 2001.

16. G.Scheldrick, SADBS - Bruker AXS area detector scaling and absorption, Version 2008/1. **2009**.
17. Stoe&Cie, Darmstadt, Germany. X-SHAPE. **1998**.
18. J.Suchet, *Electrical Conduction in Solid Materials in International Series of Monographs in the Science of the Solid State*. Oxford: Pergamon Press: 1975.
19. Pauw, D., Philips Res.Rep. **1958**, 13, 1.
20. Wert, A., *Physics of Solids*. McGraw-Hill: New York, 1964.
21. S.Charndra, *Supersonic Solids - Principles and Application*. Amsterdam, 1981.
22. F. Kremer, A. Schonhals.W. Luck. Broadband Dielectric Spectroscopy. **2002**.
23. Sidorovich, A. M., Dielectric Spectrum Of Water. *Ukrainskii Fizicheskii Zhurnal* **1984**, 29, (8), 1175-1181.
24. Hippel, A. R., *Dielectrics and Waves*. N. Y.: John Willey & Sons, 1954.
25. Volkov A. A., Prokhorov A. S., Broadband Dielectric Spectroscopy of Solids. – Radiophysics and Quantum Electronics. **2003**, 46, (8), 657-665.
26. Novocontrol; GmbH, WinData Version 4.5. **1995-2003**.
27. Kohler, U., PhD Dissertation  
University Hannover. **1987**.
28. Novocontrol; GmbH, WinFit Version 2.9. **1996**.
29. DiSalvo, F. J., Thermoelectric cooling and power generation. *Science* **1999**, 285, (5428), 703-706.
30. Venkatasubramanian, R.; Siivola, E.; Colpitts, T.; O'Quinn, B., Thin-film thermoelectric devices with high room-temperature figures of merit. *Nature* **2001**, 413, (6856), 597-602.
31. Harman, T. C.; Walsh, M. P.; Laforge, B. E.; Turner, G. W., Nanostructured thermoelectric materials. *Journal Of Electronic Materials* **2005**, 34, (5), L19-L22.
32. Rockwood, A. L., Relationship Of Thermoelectricity To Electronic Entropy. *Physical Review A* **1984**, 30, (5), 2843-2844.
33. S.S.Friedel, Paris, 1873; Vol. 77, p 211.
34. Pabst, A., Notes On The Structure Of Delafossite. *American Mineralogist* **1946**, 31, (11-1), 539-546.
35. Shannon, R. D.; Prewitt, C. T., Effective Ionic Radii In Oxides And Fluorides. *Acta Crystallographica Section B-Structural Crystallography And Crystal Chemistry* **1969**, B 25, 925-&.

36. Shannon, R. D., Revised Effective Ionic-Radii And Systematic Studies Of Interatomic Distances In Halides And Chalcogenides. *Acta Crystallographica Section A* **1976**, 32, (SEP1), 751-767.
37. Stahlin, W.; Oswald, H. R., Preparation And Characterization Of Silver Cobalt Oxide AgCoO<sub>2</sub>. *Zeitschrift Fur Anorganische Und Allgemeine Chemie* **1969**, 367, (3-4), 206-&.
38. Shannon, R. D.; Rogers, D. B.; Prewitt, C. T., Chemistry Of Noble Metal Oxides.1. Syntheses And Properties Of Abo<sub>2</sub> Delafossite Compounds. *Inorganic Chemistry* **1971**, 10, (4), 713-&.
39. S.Ramsdell, L., *Am Mineral* **1947**, 32-64.
40. Sorgel, T.; Jansen, M., A new hexagonal modification of AgNiO<sub>2</sub>. *Zeitschrift Fur Anorganische Und Allgemeine Chemie* **2005**, 631, (15), 2970-2972.
41. Kohler, B. U.; Jansen, M., Synthesis And Structural Data Of Delafossites CuAlO<sub>2</sub>, CuGaO<sub>2</sub>, CuScO<sub>2</sub>, CuYO<sub>2</sub>. *Zeitschrift Fur Anorganische Und Allgemeine Chemie* **1986**, 543, (12), 73-80.
42. Effenberger, H., Structure Of Hexagonal Copper(I) Ferrite. *Acta Crystallographica Section C-Crystal Structure Communications* **1991**, 47, 2644-2646.
43. Prewitt, C. T.; Shannon, R. D.; Rogers, D. B., Chemistry Of Noble Metal Oxides.2. Crystal Structures Of PtCoO<sub>2</sub>, PdCoO<sub>2</sub>, CuFeO<sub>2</sub>, And AgFeO<sub>2</sub>. *Inorganic Chemistry* **1971**, 10, (4), 719-&.
44. McQueen, T.; Huang, Q.; Lynn, J. W.; Berger, R. F.; Klimczuk, T.; Ueland, B. G.; Schiffer, P.; Cava, R. J., Magnetic structure and properties of the S=5/2 triangular antiferromagnet alpha-NaFeO<sub>2</sub>. *Physical Review B* **2007**, 76, (2).
45. Orman, H. J.; Wiseman, P. J., Cobalt(III) Lithium-Oxide, CoLiO<sub>2</sub> - Structure Refinement By Powder Neutron-Diffraction. *Acta Crystallographica Section C-Crystal Structure Communications* **1984**, 40, (JAN), 12-14.
46. Jansen, M.; Hoppe, R., Notice On Oxocobaltates Of Sodium. *Zeitschrift Fur Anorganische Und Allgemeine Chemie* **1974**, 408, (2), 104-106.
47. Hobbie, K.; Hoppe, R., On The Structure Of Na<sub>2</sub>CoO<sub>2</sub>. *Zeitschrift Fur Anorganische Und Allgemeine Chemie* **1988**, 565, (10), 106-110.
48. Laubach, S.; Laubach, S.; Schmidt, P. C.; Enslin, D.; Schmid, S.; Jaegermann, W.; Thissen, A.; Nikolowski, K.; Ehrenberg, H., Changes in the crystal and electronic structure of LiCoO<sub>2</sub> and LiNiO<sub>2</sub> upon Li intercalation and de-intercalation. *Physical Chemistry Chemical Physics* **2009**, 11, (17), 3278-3289.

49. Marezio, M., Crystal Structure Of LiGaO<sub>2</sub>. *Acta Crystallographica* **1965**, 18, 481-&.
50. Muller, H. P.; Hoppe, R., The Crystal-Structure Of KGaO<sub>2</sub> And NaGaO<sub>2</sub>(Ii). *Zeitschrift Fur Anorganische Und Allgemeine Chemie* **1992**, 611, (5), 73-80.
51. Hoppe, R.; Sabrowsk.H, Oxoscandate Der Alkalimetalle - KScO<sub>2</sub> Und RbScO<sub>2</sub>. *Zeitschrift Fur Anorganische Und Allgemeine Chemie* **1965**, 339, (3-4), 144-&.
52. Hoppe, R.; Sabrowsk.H, Alkali Metal Scandates Yttrates Indates And Thallates. *Zeitschrift Fur Anorganische Und Allgemeine Chemie* **1968**, 357, (4-6), 202-&.
53. Hoppe, R.; Rohrborn, H. J., Oxydationsprodukte Intermetallischer Phasen.1. Untersuchungen Am NaTiO<sub>2</sub>. *Zeitschrift Fur Anorganische Und Allgemeine Chemie* **1964**, 327, (3-4), 199-206.
54. Hoppe, R.; Werding, G., Oxothallate Der Alkalimetalle. *Zeitschrift Fur Anorganische Und Allgemeine Chemie* **1961**, 307, (3-4), 174-186.
55. Hoppe, R.; Panek, P., Alpha LiTiO<sub>2</sub>. *Zeitschrift Fur Anorganische Und Allgemeine Chemie* **1971**, 384, (2), 97-&.
56. Nagarajan, R.; Duan, N.; Jayaraj, M. K.; Li, J.; Vanaja, K. A.; Yokochi, A.; Draeseke, A.; Tate, J.; Sleight, A. W., p-Type conductivity in the delafossite structure. *International Journal Of Inorganic Materials* **2001**, 3, (3), 265-270.
57. Duan, N.; Nagarajan, R.; Li, J.; Yokochi, A.; Achuthan, A.; Uma, S.; Jayaraj, M. K.; Sleight, A. W., Delafossites for electronic applications. *Abstracts Of Papers Of The American Chemical Society* **2001**, 221, 605-INOR.
58. Shin, Y. J.; Doumerc, J. P.; Dordor, P.; Pouchard, M.; Hagenmuller, P., Preparation And Physical-Properties Of The Delafossite-Type Solid-Solutions AgCo<sub>1-x</sub>Ni<sub>x</sub>O<sub>2</sub> (0-Less-Than-Or-Equal-To-X-Less-Than-Or-Equal-To-0.5). *Journal Of Solid State Chemistry* **1993**, 107, (1), 194-200.
59. Nagarajan, R.; Uma, S.; Jayaraj, M. K.; Tate, J.; Sleight, A. W., New CuM<sub>2/3</sub>Sb<sub>1/3</sub>O<sub>2</sub> and AgM<sub>2/3</sub>Sb<sub>1/3</sub>O<sub>2</sub> compounds with the delafossite structure. *Solid State Sciences* **2002**, 4, (6), 787-792.
60. Doumerc, J. P.; Ammar, A.; Wichainchai, A.; Pouchard, M.; Hagenmuller, P., Some New Compounds With Delafossite Structure. *Journal Of Physics And Chemistry Of Solids* **1987**, 48, (1), 37-43.
61. Tate, J.; Jayaraj, M. K.; Draeseke, A. D.; Ulbrich, T.; Sleight, A. W.; Vanaja, K. A.; Nagarajan, R.; Wager, J. F.; Hoffman, R. L., p-Type oxides for use in transparent diodes. *Thin Solid Films* **2002**, 411, (1), 119-124.

62. Munoz-Rojas, D.; Subias, G.; Oro-Sole, J.; Fraxedas, J.; Martinez, B.; Casas-Cabanas, M.; Canales-Vazquez, J.; Gonzalez-Calbet, J.; Garcia-Gonzalez, E.; Walton, R. I.; Casan-Pastor, N., Ag<sub>2</sub>CuMnO<sub>4</sub>: A new silver copper oxide with delafossite structure. *Journal Of Solid State Chemistry* **2006**, 179, (12), 3883-3892.
63. Hosogi, Y.; Kato, H.; Kudo, A., Visible light response of AgLi<sub>1/3</sub>M<sub>2/3</sub>O<sub>2</sub> (M = Ti and Sn) synthesized from layered Li<sub>2</sub>MO<sub>3</sub> using molten AgNO<sub>3</sub>. *Journal Of Materials Chemistry* **2008**, 18, (6), 647-653.
64. Kawazoe, H.; Yasukawa, M.; Hyodo, H.; Kurita, M.; Yanagi, H.; Hosono, H., P-type electrical conduction in transparent thin films of CuAlO<sub>2</sub>. *Nature* **1997**, 389, (6654), 939-942.
65. Ginley, D. S.; Bright, C., Transparent conducting oxides. *Mrs Bulletin* **2000**, 25, (8), 15-18.
66. Rogers, D. B.; Shannon, R. D.; Prewitt, C. T.; Gillson, J. L., Chemistry Of Noble Metal Oxides.3. Electrical Transport Properties And Crystal Chemistry Of ABO<sub>2</sub> Compounds With Delafossite Structure. *Inorganic Chemistry* **1971**, 10, (4), 723-&.
67. Tanaka, M.; Hasegawa, M.; Higuchi, T.; Tsukamoto, T.; Tezuka, Y.; Shin, S.; Takei, H., Origin of the metallic conductivity in PdCoO<sub>2</sub> with delafossite structure. *Physica B* **1998**, 245, (2), 157-163.
68. Carcia, P. F.; Shannon, R. D.; Bierstedt, P. E.; Flippen, R. B., O<sub>2</sub> Electrocatalysis On Thin-Film Metallic Oxide Electrodes With The Delafossite Structure. *Journal Of The Electrochemical Society* **1980**, 127, (9), 1974-1978.
69. Monnier, J. R.; Hanrahan, M. J.; Apai, G., A Study Of The Catalytically Active Copper Species In The Synthesis Of Methanol Over Cu-Cr Oxide. *Journal Of Catalysis* **1985**, 92, (1), 119-126.
70. Christopher, J.; Swamy, C. S., Catalytic Activity And Xps Investigation Of Dalofossite Oxides, CuMO<sub>2</sub> (M = Al, Cr Or Fe). *Journal Of Materials Science* **1992**, 27, (5), 1353-1356.
71. Domen, K.; Ikeda, S.; Takata, T.; Tanaka, A.; Hara, M.; Kondo, J. N., Mechano-catalytic overall water-splitting into hydrogen and oxygen on some metal oxides. *Applied Energy* **2000**, 67, (1-2), 159-179.
72. Jansen, M., Homoatomic d10 - d10 Interactions - Their Effects On Structure And Chemical And Physical-Properties. *Angewandte Chemie-International Edition In English* **1987**, 26, (11), 1098-1110.



73. Sauvage, F.; Munoz-Rojas, D.; Poeppelmeier, K. R.; Casan-Pastor, N., Transport properties and lithium insertion study in the p-type semi-conductors  $\text{AgCuO}_2$  and  $\text{AgCu}_{0.5}\text{Mn}_{0.5}\text{O}_2$ . *Journal Of Solid State Chemistry* **2009**, 182, (2), 374-380.
74. Sukeshini, A. M.; Kobayashi, H.; Tabuchi, M.; Kageyama, H., Lithium intercalation of delafossite, cuprous iron oxide. *Intercalation Compounds For Battery Materials, Proceedings* **2000**, 99, (24), 104-111.
75. Doumerc, J. P.; Parent, C.; Zhang, J. C.; Leflem, G.; Ammar, A., Luminescence Of The  $\text{Cu}^+$  Ion In  $\text{CuLaO}_2$ . *Journal Of The Less-Common Metals* **1989**, 148, (1-2), 333-337.
76. Jacob, A.; Parent, C.; Boutinaud, P.; LeFlem, G.; Doumerc, J. P.; Ammar, A.; Elazhari, M.; Elaati, M., Luminescent properties of delafossite-type oxides  $\text{LaCuO}_2$  and  $\text{YCuO}_2$ . *Solid State Communications* **1997**, 103, (9), 529-532.
77. Katsui, A.; Takahashi, Y.; Matsushita, H., Strong yellow-green luminescence in delafossite-type  $\text{CuLaO}_2$  doped with calcium or strontium. *Japanese Journal Of Applied Physics Part 2-Letters & Express Letters* **2007**, 46, (20-24), L546-L548.
78. Yasukawa, M.; Ikeuchi, K.; Kono, T.; Ueda, K.; Hosono, H., Thermoelectric properties of delafossite-type layered oxides  $\text{AgIn}_{(1-x)}\text{Sn}_{(x)}\text{O}_{(2)}$ . *Journal Of Applied Physics* **2005**, 98, (1).
79. Hayashi, K.; Nozaki, T.; Kajitani, T., Structure and high temperature thermoelectric properties of delafossite-type oxide  $\text{CuFe}_{1-x}\text{Ni}_x\text{O}_2$  ( $0 \leq x \leq 0.05$ ). *Japanese Journal Of Applied Physics Part 1-Regular Papers Brief Communications & Review Papers* **2007**, 46, (8A), 5226-5229.
80. Zhu, C. F.; Zheng, S. Y.; Jiang, G. S.; Su, J. R., The structural and electrical property of  $\text{CuCr}_{1-x}\text{Ni}_x\text{O}_2$  delafossite compounds. *Materials Letters* **2006**, vol.60, no.29-30, 3871-3.
81. Koumoto, K.; Koduka, H.; Seo, W. S., Thermoelectric properties of single crystal  $\text{CuAlO}_2$  with a layered structure. *Journal Of Materials Chemistry* **2001**, 11, (2), 251-252.
82. Isawa, K.; Yaegashi, Y.; Ogota, S.; Nagano, M.; Sudo, S.; Yamada, K.; Yamauchi, H., Thermoelectric power of delafossite-derived compounds  $\text{RCuO}_{2+\delta}$ ; (R = Y, La, Pr, Nd, Sm, and Eu). *Physical Review B* **1998**, 57, (13), 7950-7954.
83. Takahashi, Y.; Matsushita, H.; Katsui, A., Synthesis and characterization of delafossite  $\text{CuLaO}_2$  for thermoelectric application. *Progress in Powder Metallurgy, Pts 1 and 2* **2007**, 534-536, 1081-1084.

84. Muguerra, H.; Colin, C.; Anne, M.; Julien, M. H.; Strobel, P., Topotactic synthesis, structure and magnetic properties of a new hexagonal polytype of silver cobaltate(III)  $\text{AgCoO}_{2+\delta}$ . *Journal Of Solid State Chemistry* **2008**, 181, (11), 2883-2888.
85. Emons, H. H.; Beger, E., Zur Darstellung Von  $\text{CuCoO}_2$  Und  $\text{AgCoO}_2$ . *Zeitschrift Fur Chemie* **1967**, 7, (5), 200-&.
86. W. Büchner, R. S., G. Winter, K. H. Büchel, Industrielle Anorganische Chemie. **1986**.
87. Demazeau, G.; Maestro, P.; Plante, T.; Pouchard, M.; Hagenmuller, P., Solid-Solution Of Chromium, Rhodium And Oxygen. *Journal Of Physics And Chemistry Of Solids* **1980**, 41, (10), 1139-1145.
88. Demazeau, G.; Maestro, P.; Plante, T.; Pouchard, M.; Hagenmuller, P., Materials For Magnetic Recording Derived From Chromium Dioxide. *Materials Research Bulletin* **1979**, 14, (1), 121-126.
89. Bayer, G.; Wiedemann, H. G., Formation, Dissociation And Expansion Behavior Of Platinum Group Metal-Oxides ( $\text{PdO}$ ,  $\text{RuO}_2$ ,  $\text{IrO}_2$ ). *Thermochimica Acta* **1975**, 11, (1), 79-88.
90. Lang, G., Strukturvergleiche An Ternaren Und Quarternaren Oxiden. *Zeitschrift Fur Anorganische Und Allgemeine Chemie* **1966**, 348, (5-6), 246-&.
91. Kreuzbur.G; Stewner, F.; Hoppe, R., Crystal Structure Of  $\text{Li}_2\text{SnO}_3$ . *Zeitschrift Fur Anorganische Und Allgemeine Chemie* **1970**, 379, (3), 242-&.
92. James, A.; Goodenough, J. B., Structure And Bonding In Lithium Ruthenate,  $\text{Li}_2\text{RuO}_3$ . *Journal Of Solid State Chemistry* **1988**, 74, (2), 287-294.
93. Jansen, M.; Hoppe, R., Knowledge Of Nacl-Type Structure Family - New Investigations On  $\text{Li}_2\text{MnO}_3$ . *Zeitschrift Fur Anorganische Und Allgemeine Chemie* **1973**, 397, (3), 279-289.
94. Strobel, P.; Lambertandron, B., Crystallographic And Magnetic-Structure Of  $\text{Li}_2\text{MnO}_3$ . *Journal Of Solid State Chemistry* **1988**, 75, (1), 90-98.
95. Kobayashi, H.; Tabuchi, M.; Shikano, M.; Kageyama, H.; Kanno, R., Structure, and magnetic and electrochemical properties of layered oxides,  $\text{Li}_2\text{IrO}_3$ . *Journal Of Materials Chemistry* **2003**, 13, (4), 957-962.
96. O'Malley, M. J.; Verweij, H.; Woodward, P. M., Structure and properties of ordered  $\text{Li}_2\text{IrO}_3$  and  $\text{Li}_2\text{PtO}_3$ . *Journal Of Solid State Chemistry* **2008**, 181, (8), 1803-1809.
97. Boulineau, A.; Croguennec, L.; Delmas, C.; Weill, F., Reinvestigation of  $\text{Li}_2\text{MnO}_3$  Structure: Electron Diffraction and High Resolution TEM. *Chemistry Of Materials* **2009**, 21, (18), 4216-4222.

98. Bayer, G.; Wiedemann, H. G., Formation And Thermal-Stability Of Rhodium Oxides. *Thermochimica Acta* **1976**, 15, (2), 213-226.
99. Muller, O.; Roy, R., Formation And Stability Of Platinum And Rhodium Oxides At High Oxygen Pressures And Structures Of Pt<sub>3</sub>O<sub>4</sub>, Beta-PtO<sub>2</sub> And RhO<sub>2</sub>. *Journal Of The Less-Common Metals* **1968**, 16, (2), 129-&.
100. Shannon, R. D., Synthesis And Properties Of 2 New Members Of Rutile Family RhO<sub>2</sub> And PtO<sub>2</sub>. *Solid State Communications* **1968**, 6, (3), 139-&.
101. Bertaut, E. F.; Dulac, J. F., Sur l'isomorphisme d'oxydes ternaires de chrome et de rhodium trivalents. *Journal of Physics and Chemistry of Solids* **1961**, 21, 118-119.
102. Grey, C. P.; Breger, J.; Meng, J.; Dupre, N.; Meng, Y. S.; Yang, S.-H.; Ceder, G., High-resolution X-ray diffraction, DIFFaX, NMR and first principles study of disorder in the Li<sub>2</sub>/MnO<sub>3</sub>-Li[Ni<sub>1/2</sub>/Mn<sub>1/2</sub>]/O<sub>2</sub> solid solution. *Journal of Solid State Chemistry* **2005**, vol.178, no.9, 2575-85.
103. Tromel, M.; Hauck, J., Disorder In Lattices Of Li<sub>2</sub>SnO<sub>3</sub> Type And Low Temperature Form Of This Compound. *Zeitschrift Fur Anorganische Und Allgemeine Chemie* **1970**, 373, (1), 8-&.
104. Jansen, M.; Hoppe, R., New Oxocobaltates (IV) K<sub>6</sub>(Co<sub>2</sub>O<sub>7</sub>) And Li<sub>4</sub>CoO<sub>4</sub>. *Naturwissenschaften* **1973**, 60, (2), 104-105.
105. Jansen, M.; Hoppe, R., Oxocobaltates Of Alkali-Metals - Li<sub>8</sub>CoO<sub>6</sub>. *Zeitschrift Fur Anorganische Und Allgemeine Chemie* **1973**, 398, (1), 54-62.
106. Jansen, M.; Hoppe, R., KCoO<sub>2</sub> And RbCoO<sub>2</sub>. *Zeitschrift Fur Anorganische Und Allgemeine Chemie* **1975**, 417, (1), 31-34.
107. Hoppe, R.; Brachtel, G.; Jansen, M., Knowledge Of Oxomanganates(III) - LiMnO<sub>2</sub> And Beta-NaMnO<sub>2</sub>. *Zeitschrift Fur Anorganische Und Allgemeine Chemie* **1975**, 417, (1), 1-10.
108. Hobbie, K.; Hoppe, R., On Oxorhodates Of Alkali-Metals - Beta-LiRhO<sub>2</sub>. *Zeitschrift Fur Anorganische Und Allgemeine Chemie* **1986**, 535, (4), 20-30.
109. Brown, I. D.; Wu, K. K., Empirical Parameters For Calculating Cation-Oxygen Bond Valences. *Acta Crystallographica Section B-Structural Science* **1976**, 32, (JUL15), 1957-1959.
110. Brown, I. D.; Altermatt, D., Bond-Valence Parameters Obtained From A Systematic Analysis Of The Inorganic Crystal-Structure Database. *Acta Crystallographica Section B-Structural Science* **1985**, 41, (AUG), 244-247.
111. Honda, K., The thermomagnetic properties of the elements. *Annalen Der Physik* **1910**, 32, (10), 1027-1063.

112. Owen, M., Magnetochemical testings. The thermomagnetic properties of elements II. *Annalen Der Physik* **1912**, 37, (4), 657-699.
113. Demazeau, G.; Baranov, A.; Pottgen, R.; Kienle, L.; Moller, M. H.; Hoffmann, R. D.; Valldor, M., An anhydrous high-pressure synthesis route to rutile type RhO<sub>2</sub>. *Zeitschrift Fur Naturforschung Section B-A Journal Of Chemical Sciences* **2006**, 61, (12), 1500-1506.
114. J.B.Goodenough, *Lesxydes des Metaux de Transition*. Gauthier-Villars: Paris, 1973.
115. Lueken, H., *Magnetochemie*. 1999.
116. Okada, S.; Yamaki, J.; Asakura, K.; Ohtsuka, H.; Arai, H.; Tobishima, S.; Sakurai, Y., Cathode characteristics of layered rocksalt oxide, Li<sub>2</sub>PtO<sub>3</sub>. *Electrochimica Acta* **1999**, 45, (1-2), 329-334.
117. Bouchard, G. H.; Sienko, M. J., Magnetic Susceptibility Of Barium Molybdate(4) And Strontium Molybdate(4) In Range 2-300 Degrees K. *Inorganic Chemistry* **1968**, 7, (3), 441-&.
118. Gummow, R. J.; Thackeray, M. M.; David, W. I. F.; Hull, S., Structure And Electrochemistry Of Lithium Cobalt Oxide Synthesized At 400-Degrees-C. *Materials Research Bulletin* **1992**, 27, (3), 327-337.
119. Wang, B.; Bates, J. B.; Hart, F. X.; Sales, B. C.; Zuhr, R. A.; Robertson, J. D., Characterization of thin-film rechargeable lithium batteries with lithium cobalt oxide cathodes. *Journal Of The Electrochemical Society* **1996**, 143, (10), 3203-3213.
120. Kobayashi, H.; Kanno, R.; Kawamoto, Y.; Tabuchi, M.; Nakamura, O.; Takano, M., Structure And Lithium Deintercalation Of Li<sub>2</sub>Xruo<sub>3</sub>. *Solid State Ionics* **1995**, 82, (1-2), 25-31.
121. Weise, E.; Klemm, W., Fluorokomplexe Des Vierwertigen Rhodiums. *Zeitschrift Fur Anorganische Und Allgemeine Chemie* **1953**, 272, (1-4), 211-220.
122. Feldman, I.; Nyholm, R. S.; Watton, E., Magnetochemistry Of Hexachlorohodate(4) Ion. *Journal Of The Chemical Society* **1965**, (SEP), 4724-&.
123. E. A. Boudreaux, L. N. M., *Theory and applications of molecular paramagnetism*. Wiley: New York, 1976.
124. Ballhausen, C. J.; Asmussen, R. W., The Diamagnetic Susceptibility And The High-Frequency Term In Co(III)-Complex And Rh(III)-Complexes. *Acta Chemica Scandinavica* **1957**, 11, (3), 479-483.
125. Stephens, P. W., Phenomenological model of anisotropic peak broadening in powder diffraction. *Journal Of Applied Crystallography* **1999**, 32, 281-289.
126. Leineweber, A., Anisotropic diffraction-line broadening due to microstrain distribution: parametrization opportunities. *Journal Of Applied Crystallography* **2006**, 39, 509-518.

127. Warren, B. E., X-ray diffraction in random layer lattices. *Physical Review* **1941**, 59, (9), 693-698.
128. Treacy, M. M. J.; Newsam, J. M.; Deem, M. W., A General Recursion Method For Calculating Diffracted Intensities From Crystals Containing Planar Faults. *Proceedings Of The Royal Society Of London Series A-Mathematical Physical And Engineering Sciences* **1991**, 433, (1889), 499-520.
129. Gusev, A. I.; Rempel, A. A., Vacancy Distribution In Ordered Me<sub>6</sub>C<sub>5</sub>-Type Carbides. *Journal Of Physics C-Solid State Physics* **1987**, 20, (31), 5011-5025.
130. Hauck, J.; Mika, K., The jig-saw puzzle of crystal structures: Alloys, superconducting oxides, semiconductors, ionic conductors, surface adsorbates and magnetic structures. *Progress In Solid State Chemistry* **2000**, 28, (1-4), 1-200.
131. Berger, T. G.; Leineweber, A.; Mittemeijer, E. J.; Sarbu, C.; Duppel, V.; Fischer, P., On the formation and crystal structure of the Pd6B phase. *Zeitschrift Fur Kristallographie* **2006**, 221, (5-7), 450-463.
132. Tarakina, N. V.; Denisova, T. A.; Maksimova, L. G.; Baklanova, Y. V.; Tyutyunnik, A. P.; Berger, I. F.; Zubkov, V. G.; van Tendeloo, G., Investigation of stacking disorder in Li<sub>2</sub>SnO<sub>3</sub>. *Zeitschrift Fur Kristallographie* **2009**, 375-380.
133. Kienle, L.; Schlosser, M.; Manos, M. J.; Malliakas, C. D.; Duppel, V.; Reiner, C.; Deiseroth, H. J.; Kanatzidis, M. G.; Kelm, K.; Simon, A., Ordering Phenomena in Complex Chalcogenides - the Showcase of A(2)In(12)Q(19) (A = K, Tl, NH<sub>4</sub>; Q = Se, Te) and Pseudobinary In(2)Q(3). *European Journal Of Inorganic Chemistry*, (3), 367-378.
134. Claus, *Journal Praktical Chemistry* **1860**, 80, 302.
135. Wohler, L.; Witzmann, W., Iridium oxides. *Zeitschrift Fur Anorganische Chemie* **1908**, 57, (3), 323-352.
136. Wohler, L.; Witzmann, W., Solid solutions in the dissociation of iridium oxides. *Zeitschrift Fur Elektrochemie Und Angewandte Physikalische Chemie* **1908**, 14, 97-107.
137. Bock, O.; Muller, U., Symmetry relationships in perovskite-type variants. *Acta Crystallographica Section B-Structural Science* **2002**, 58, 594-606.
138. Sleight, A. W.; Gillson, J. L.; Bierstedt, P. E., High-Temperature Superconductivity In BaPb<sub>1-x</sub>Bi<sub>x</sub>O<sub>3</sub> System. *Solid State Communications* **1975**, 17, (1), 27-28.
139. Hair, J.; Blasse, G., Determination Of Valency State Of Bismuth In BaBiO<sub>3</sub> By Infrared Spectroscopy. *Solid State Communications* **1973**, 12, (7), 727-729.

140. Shuvaeva, E. T.; Fesenko, E. G., Synthesis and structural investigations on some perovskites containing bismuth. *Kristallografiya/Kristallografiya/Soviet Physics - Crystallography* **1969**, vol.14, no.6, ISSN 0023-4761|0038-5638.
141. Venevtse.Yn, Ferroelectric Family Of Barium Titanate. *Materials Research Bulletin* **1971**, 6, (10), 1085-&.
142. Cox, D. E.; Sleight, A. W., Mixed-Valent  $Ba_2Bi^{3+}Bi^{5+}O_6$  - Structure And Properties Vs Temperature. *Acta Crystallographica Section B-Structural Science* **1979**, 35, (JAN), 1-10.
143. Kennedy, B. J.; Howard, C. J.; Knight, K. S.; Zhaoming, Z.; Qingdi, Z., Structure and phase transitions in the ordered double perovskites  $Ba_{2/3}Bi_{1/3}V_2O_6$  and  $Ba_{2/3}Bi_{1/3}SbV_2O_6$ . *Acta Crystallographica, Section B (Structural Science)* **2006**, vol.B62, pt.4, 10 pp.
144. Uchida, S.; Kitazawa, K.; Tanaka, S., Superconductivity And Metal-Semiconductor Transition In  $BaPb_{1-x}Bi_xO_3$ . *Phase Transitions* **1987**, 8, (2), 95-128.
145. Sunshine, S. A.; Siegrist, T.; Schneemeyer, L. F.; Murphy, D. W.; Cava, R. J.; Batlogg, B.; Vandover, R. B.; Fleming, R. M.; Glarum, S. H.; Nakahara, S.; Farrow, R.; Krajewski, J. J.; Zahurak, S. M.; Waszczak, J. V.; Marshall, J. H.; Marsh, P.; Rupp, L. W.; Peck, W. F., Structure And Physical-Properties Of Single-Crystals Of The 84-K Superconductor  $Bi_{2.2}Sr_2Ca_{0.8}Cu_2O_{8+\Delta}$ . *Physical Review B* **1988**, 38, (1), 893-896.
146. Mattheiss, L. F.; Gyorgy, E. M.; Johnson, D. W., Superconductivity Above 20 K In The Ba-K-Bi-O System. *Physical Review B* **1988**, 37, (7), 3745-3746.
147. Taraphder, A.; Krishnamurthy, H. R.; Pandit, R.; Ramakrishnan, T. V., Exotic Physics In The Negative-U, Extended-Hubbard Model For Barium Bismuthates. *Europhysics Letters* **1993**, 21, (1), 79-85.
148. Taraphder, A.; Krishnamurthy, H. R.; Pandit, R.; Ramakrishnan, T. V., Negative-U Extended Hubbard-Model For Doped Barium Bismuthates. *Physical Review B* **1995**, 52, (2), 1368-1388.
149. Cava, R. J.; Batlogg, B.; Krajewski, J. J.; Rupp, L. W.; Schneemeyer, L. F.; Siegrist, T.; Vandover, R. B.; Marsh, P.; Peck, W. F.; Gallagher, P. K.; Glarum, S. H.; Marshall, J. H.; Farrow, R. C.; Waszczak, J. V.; Hull, R.; Trevor, P., Superconductivity Near 70-K In A New Family Of Layered Copper Oxides. *Nature* **1988**, 336, (6196), 211-214.
150. Uemura, Y. J.; Sternlieb, B. J.; Cox, D. E.; Brewer, J. H.; Kadono, R.; Kempton, J. R.; Kiefl, R. F.; Kretzmann, S. R.; Luke, G. M.; Mulhern, P.; Riseman, T.; Williams, D. L.;

Kossler, W. J.; Yu, X. H.; Stronach, C. E.; Subramanian, M. A.; Gopalakrishnan, J.; Sleight, A. W., Absence Of Magnetic Order In (Ba, K)BiO<sub>3</sub>. *Nature* **1988**, 335, (6186), 151-152.

151. Machida, K., An Origin Of Tc Enhancement In The Oxide Superconductor Ba(Pb, Bi)O<sub>3</sub>. *Physica C* **1988**, 156, (2), 276-280.

152. Blanton, S. H.; Collins, R. T.; Kelleher, K. H.; Rotter, L. D.; Schlesinger, Z.; Hinks, D. G.; Zheng, Y., Infrared Study Of Ba<sub>1-x</sub>K<sub>x</sub>BiO<sub>3</sub> From Charge-Density-Wave Insulator To Superconductor. *Physical Review B* **1993**, 47, (2), 996-1001.

153. Cava, R. J.; Batlogg, B.; Espinosa, G. P.; Ramirez, A. P.; Krajewski, J. J.; Peck, W. F.; Rupp, L. W.; Cooper, A. S., Superconductivity At 3.5-K In BaPb<sub>0.75</sub>Sb<sub>0.25</sub>O<sub>3</sub> - Why Is Tc So Low. *Nature* **1989**, 339, (6222), 291-293.

154. Pei, S. Y.; Jorgensen, J. D.; Hinks, D. G.; Dabrowski, B.; Richards, D. R.; Mitchell, A. W.; Zheng, Y.; Newsam, J. M.; Sinha, S. K.; Vaknin, D.; Jacobson, A. J., Structural Phase-Diagram Of The Ba<sub>1-x</sub>K<sub>x</sub>BiO<sub>3</sub> System. *Physica C* **1989**, 162, 556-557.

155. Kulkarni, G. U.; Vijayakrishnan, V.; Rao, G. R.; Seshadri, R.; Rao, C. N. R., State Of Bismuth In BaBiO<sub>3</sub> And BaBi<sub>1-x</sub>Pb<sub>x</sub>O<sub>3</sub> - Bi 4f Photoemission And Bi L<sub>3</sub> Absorption Spectroscopic Studies. *Applied Physics Letters* **1990**, 57, (17), 1823-1824.

156. Pei, S. Y.; Jorgensen, J. D.; Dabrowski, B.; Hinks, D. G.; Richards, D. R.; Mitchell, A. W.; Newsam, J. M.; Sinha, S. K.; Vaknin, D.; Jacobson, A. J., Structural Phase-Diagram Of The Ba<sub>1-x</sub>K<sub>x</sub>BiO<sub>3</sub> System. *Physical Review B* **1990**, 41, (7), 4126-4141.

157. Cox, D. E.; Sleight, A. W., Crystal-Structure Of Ba<sub>2</sub>Bi<sup>3+</sup>Bi<sup>5+</sup>O<sub>6</sub>. *Solid State Communications* **1976**, 19, (10), 969-973.

158. Cava, R. J.; Batlogg, B.; Krajewski, J. J.; Farrow, R.; Rupp, L. W.; White, A. E.; Short, K.; Peck, W. F.; Kometani, T., Superconductivity Near 30-K Without Copper - The Ba<sub>0.6</sub>K<sub>0.4</sub>BiO<sub>3</sub> Perovskite. *Nature* **1988**, 332, (6167), 814-816.

159. Batlogg, B.; Cava, R. J.; Rupp, L. W.; Espinosa, G. P.; Krajewski, J. J.; Peck, W. F.; Cooper, A. S., Superconductivity In Bi-O And Sb-O Perovskites. *Physica C* **1989**, 162, 1393-1396.

160. Batlogg, B.; Cava, R. J.; Schneemeyer, L. F.; Espinosa, G. P., High-Tc Superconductivity In Bismuthates - How Many Roads Lead To High-Tc. *Ibm Journal Of Research And Development* **1989**, 33, (3), 208-214.

161. Bishop, D. J.; Batlogg, B.; Varma, C. M.; Bucher, E.; Fisk, Z.; Smith, J. L., Ultrasonic-Attenuation And Sound-Velocity In Upt<sub>3</sub>. *Physica B & C* **1984**, 126, (1-3), 455-456.

162. Sleight, A. W., Ba(Pb,Bi)O/sub 3/ superconductors and their relationship to the copper oxide based superconductors. *Chemistry of oxide superconductors/Chemistry of oxide superconductors* **1988**, 27-33|viii+199.
163. Hinks, D. G.; Dabrowski, B.; Jorgensen, J. D.; Mitchell, A. W.; Richards, D. R.; Pei, S. Y.; Shi, D. L., Synthesis, Structure And Superconductivity In The Ba<sub>1-x</sub>K<sub>x</sub>BiO<sub>3-y</sub> System. *Nature* **1988**, 333, (6176), 836-838.
164. Pei, S. Y.; Zaluzec, N. J.; Jorgensen, J. D.; Dabrowski, B.; Hinks, D. G.; Mitchell, A. W.; Richards, D. R., Charge-Density Waves And Superconductivity In The Ba<sub>1-x</sub>K<sub>x</sub>BiO<sub>3-y</sub> System. *Physical Review B* **1989**, 39, (1), 811-814.
165. Marx, D. T.; Ali, N., Fabrication And Characterization Of Superconducting (Bi,Pb)-Sr-Ca-Cu-O Thick-Films On Sr-Ca-Cu-O Substrates. *International Journal Of Modern Physics B* **1993**, 7, (1-3), 147-150.
166. Nishio, T.; Minami, H.; Uwe, H., Large single crystals of Ba<sub>1-x</sub>K<sub>x</sub>BiO<sub>3</sub> grown by electrochemical technique. *Physica C* **2001**, 357, 376-379.
167. Tomeno, I.; Ando, K., Superconducting Properties Of The Ba<sub>1-x</sub>Rb<sub>x</sub>BiO<sub>3</sub> System. *Physical Review B* **1989**, 40, (4), 2690-2693.
168. Imai, Y.; Kato, M.; Koike, Y.; Sleight, A. W., Synthesis of the electron-doped bismuth oxide (Ba<sub>0.6</sub>Bi<sub>0.4</sub>)BiO<sub>3-x</sub>. *Physica C-Superconductivity And Its Applications* **2003**, 388, 449-450.
169. Imai, Y.; Kato, M.; Noji, T.; Koike, Y., Electrochemical synthesis of the perovskite Ba<sub>1-x</sub>Cs<sub>x</sub>BiO<sub>3</sub> from molten salts. *Low Temperature Physics, Pts A and B* **2006**, 850, 669-670.



## 6. Appendix

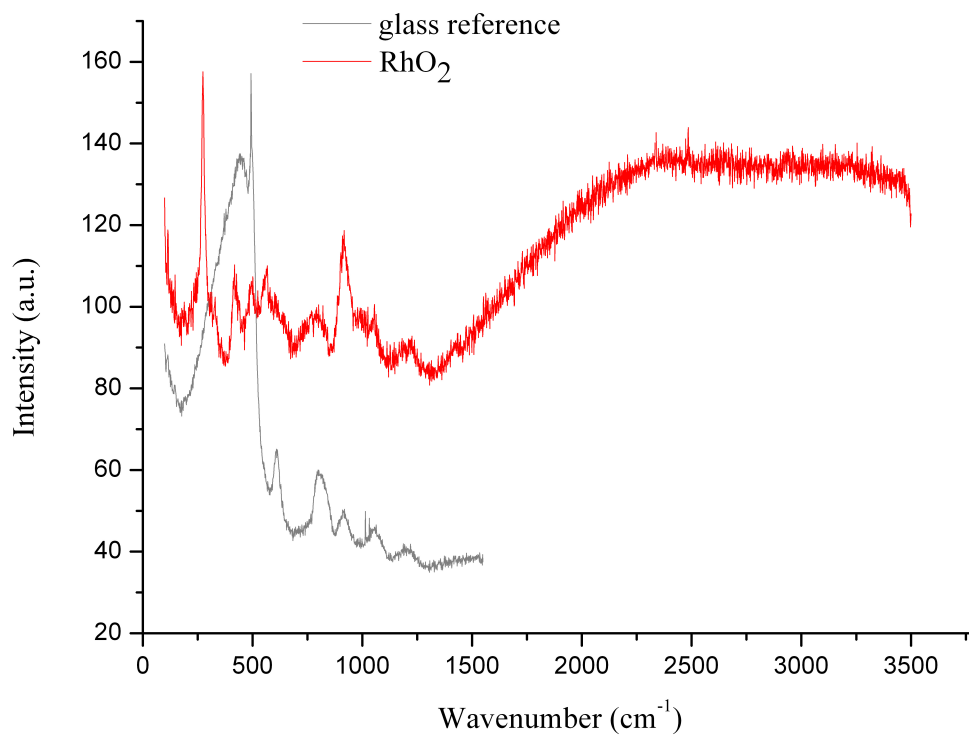


**Figure 1.** Raman spectra of RhO<sub>2</sub>. Proving the absence of -OH or H<sub>2</sub>O vibrations.

Serie 39,40,41 mit sim  $\text{Li}_2\text{IrO}_3$

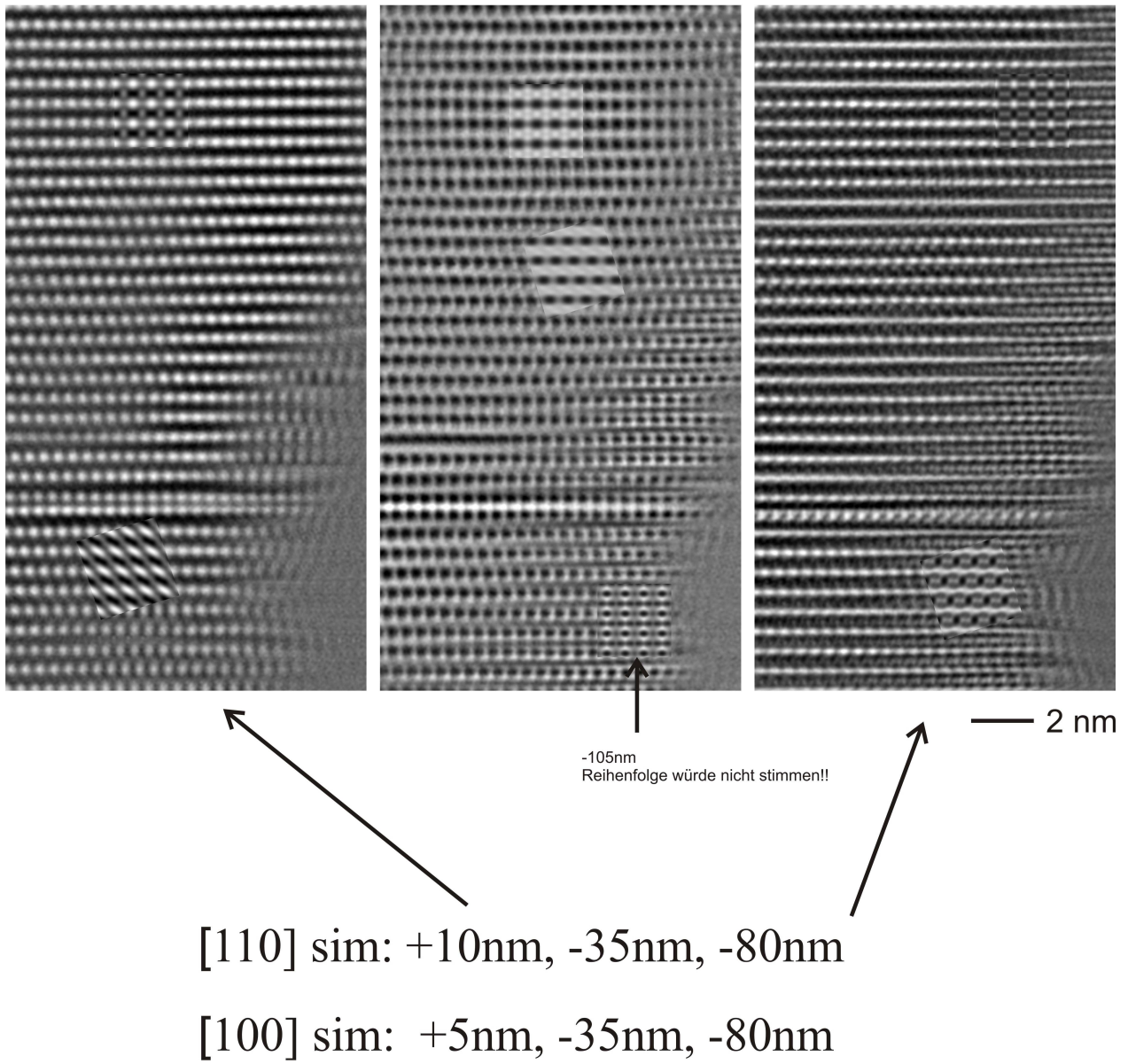
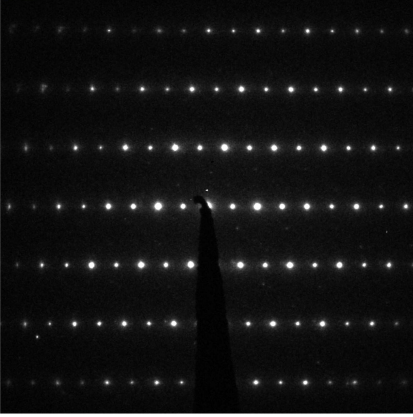


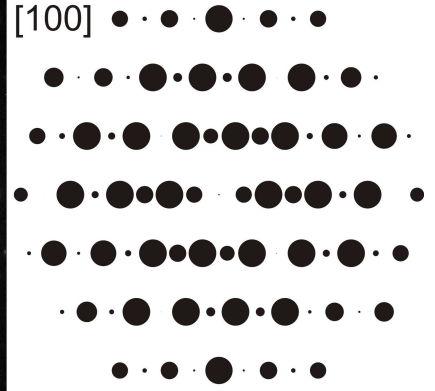
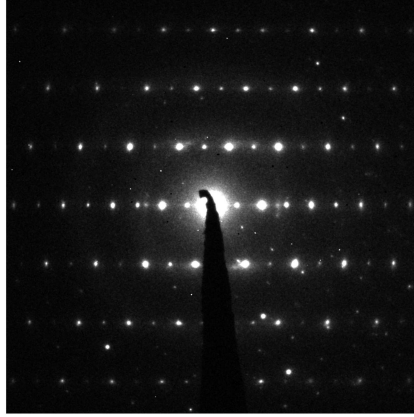
**Figure 2.** HRTEM micrographs recorded on  $\text{Ag}(\text{Li}_{1/3}\text{Ir}_{2/3})\text{O}_2$  samples.

32

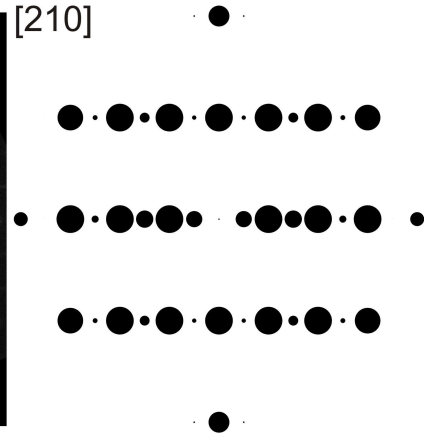
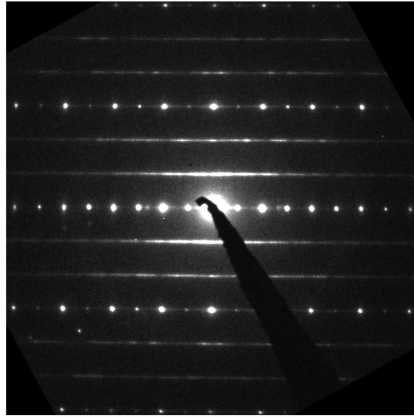
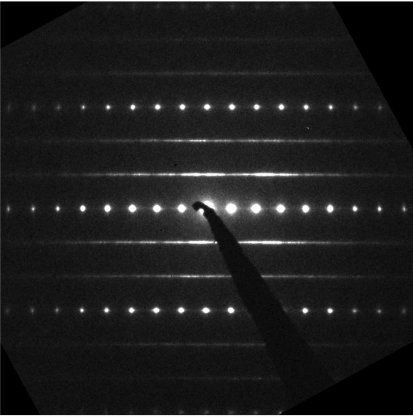
SAD



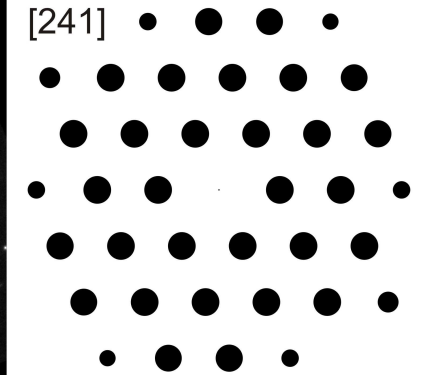
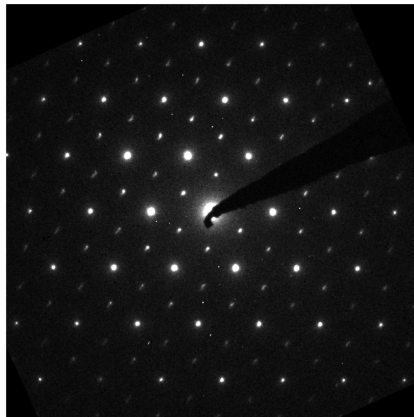
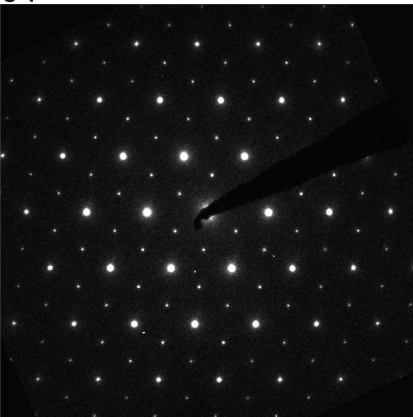
PED

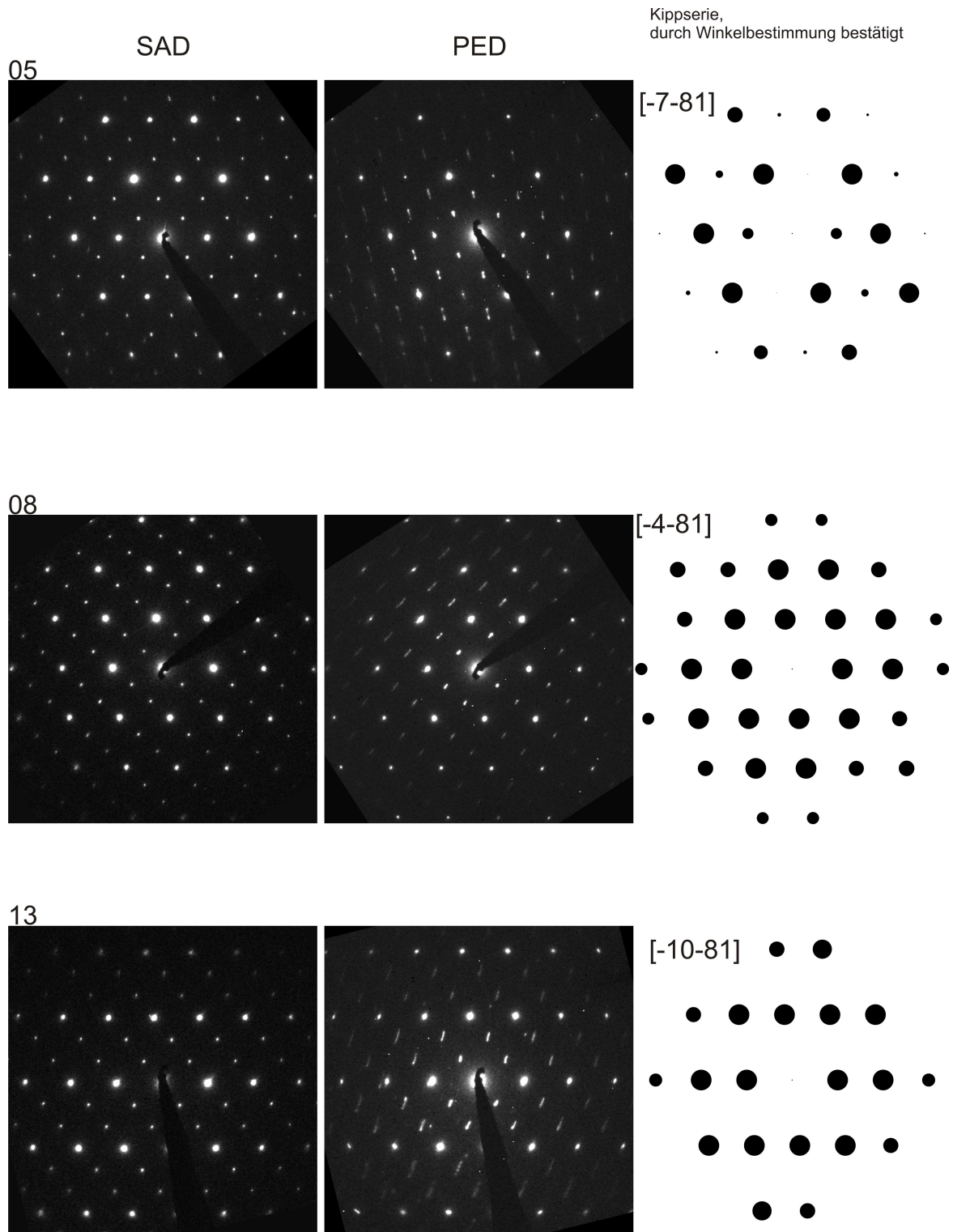


38

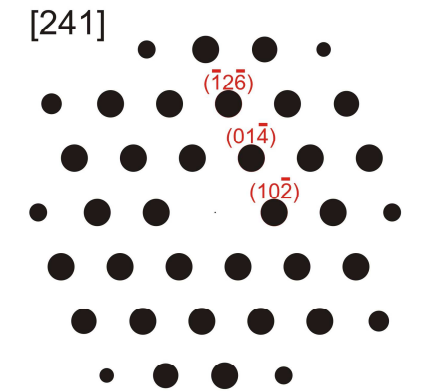
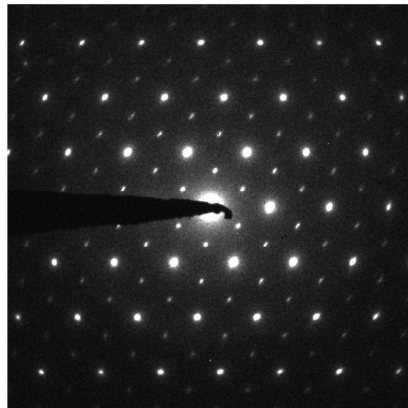
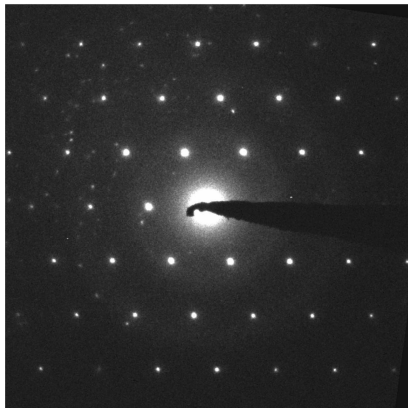
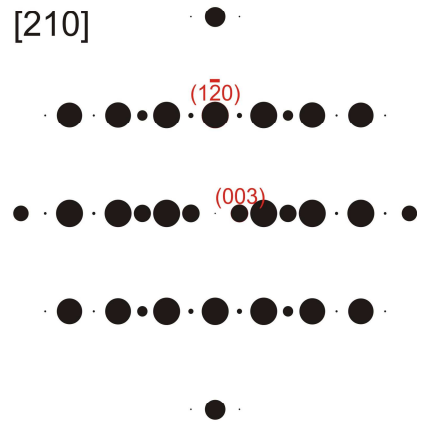
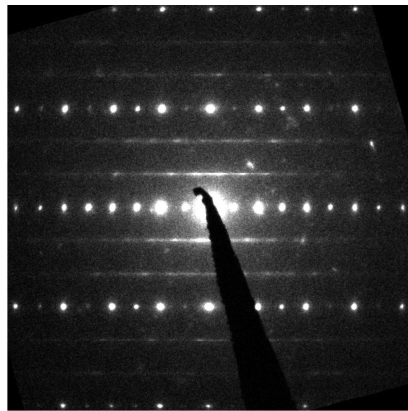
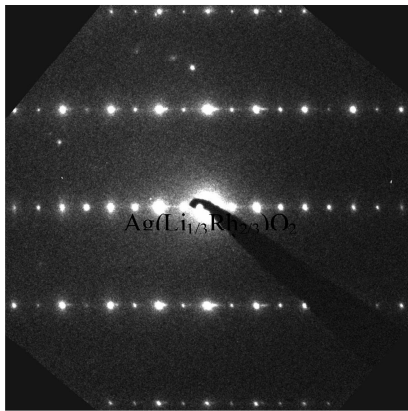
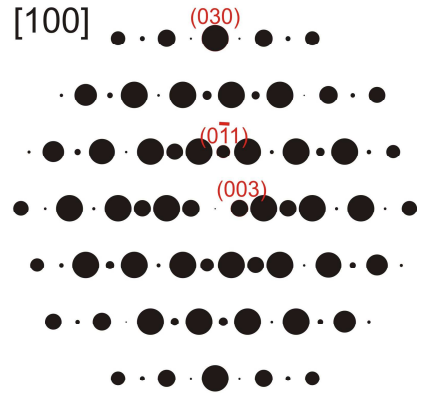
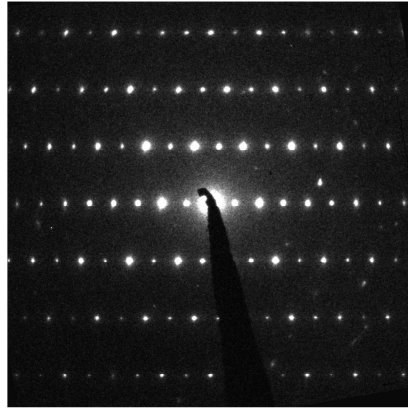
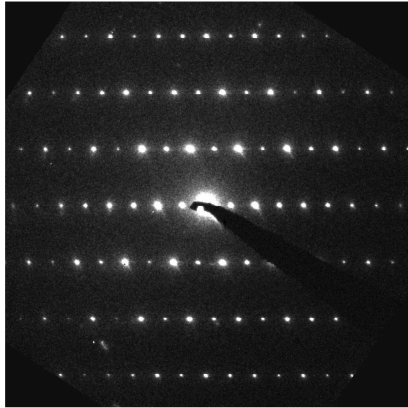


01





**Figure 3.** SED (left) and PED (middle) pattern and simulated (right) for different orientation of the crystal  $\text{Ag}(\text{Li}_{1/3}\text{Ir}_{2/3})\text{O}_2$ .



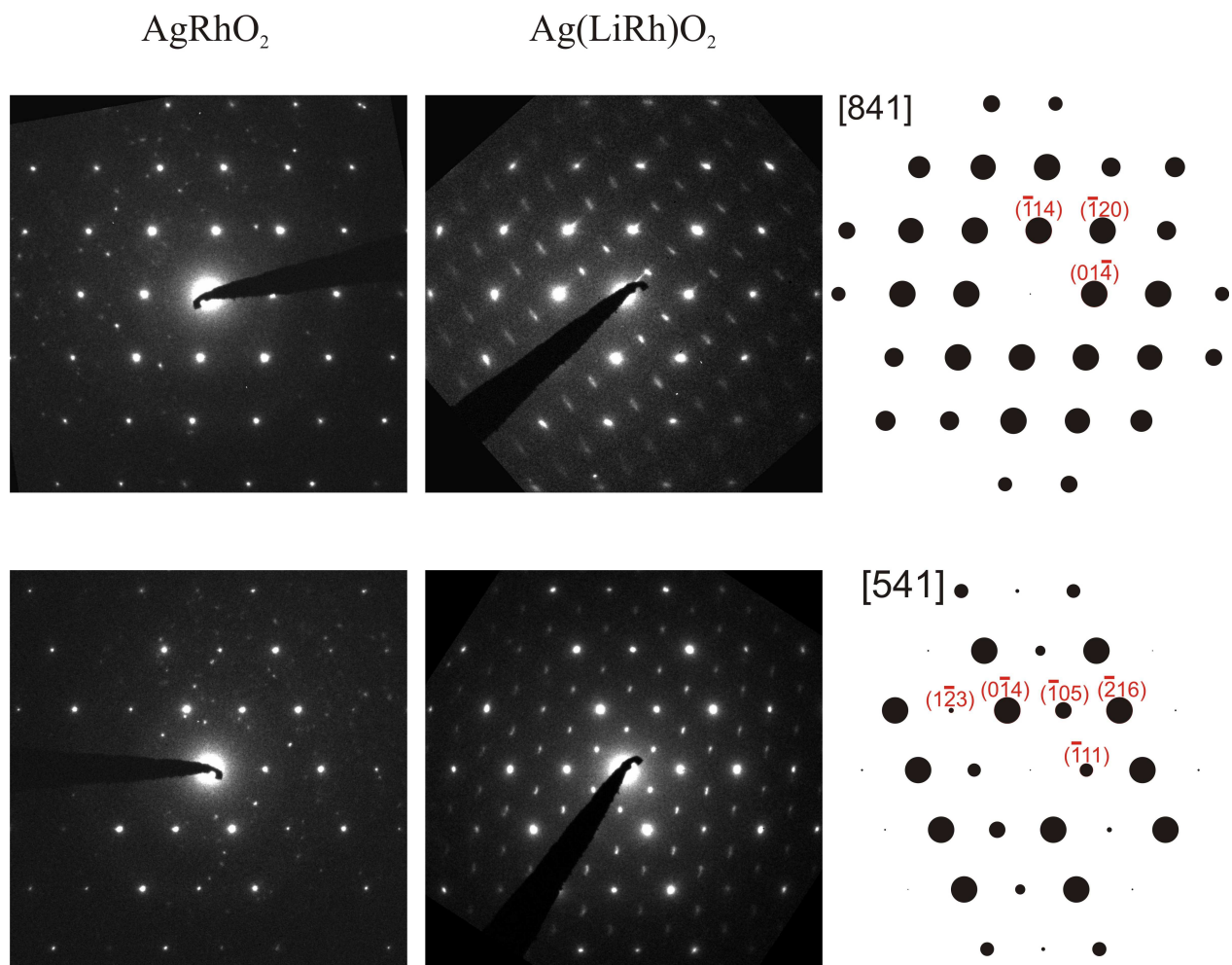


**Figure 4.** SED (left) and PED (middle) pattern and simulated (right) for different orientation of the crystal  $\text{Ag}(\text{Li}_{1/3}\text{Rh}_{2/3})\text{O}_2$ .

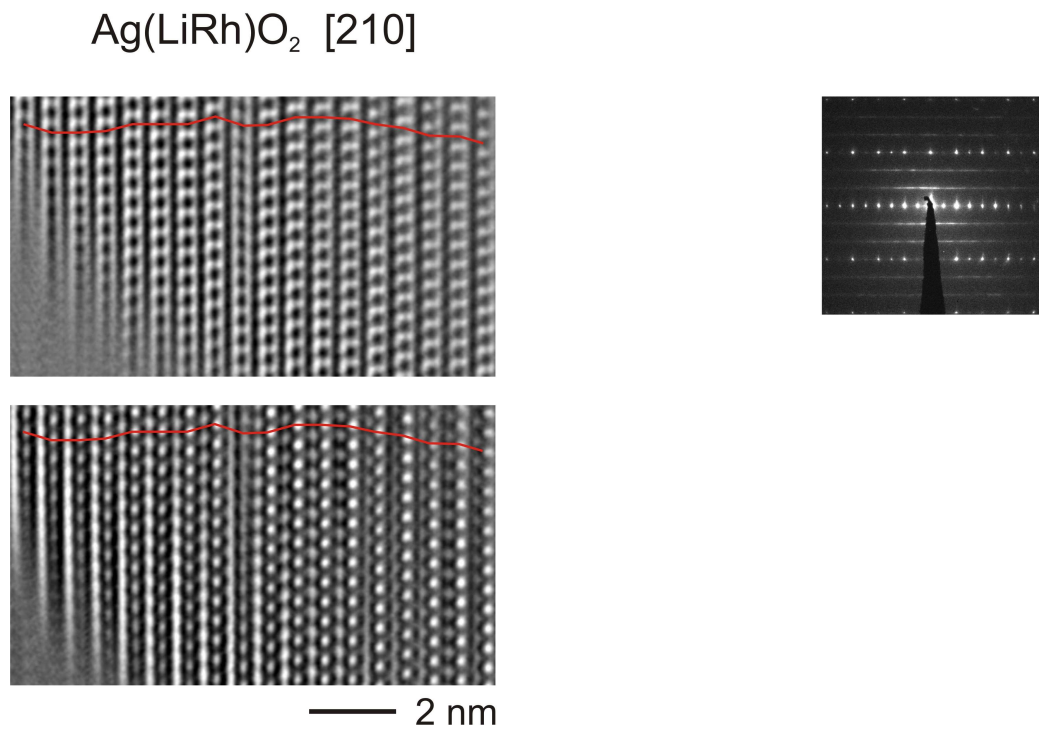
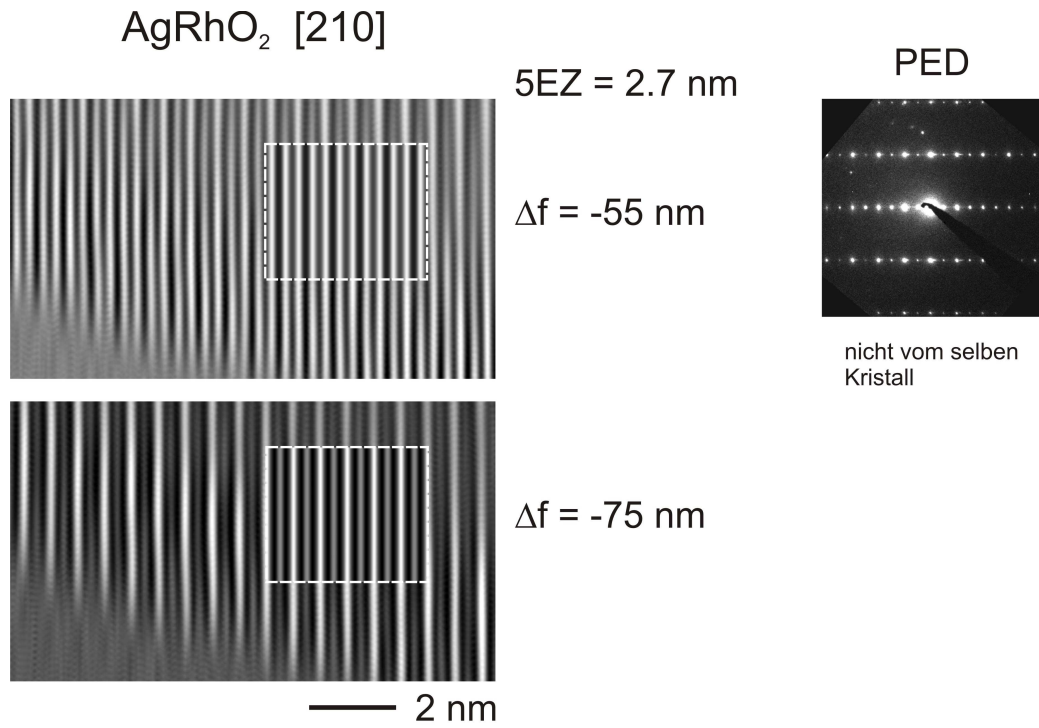


**Figure 5.** HRTEM comparison between AgRhO<sub>2</sub> and Ag(Li<sub>1/3</sub>Rh<sub>2/3</sub>)O<sub>2</sub>.

**Table 1** EDX Analysis data

Ag\_IrO<sub>2</sub> : 1

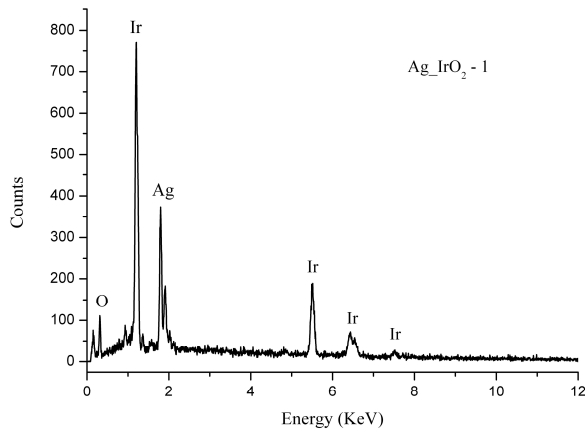
EDAX ZAF Quantification (Standardless)  
Element Normalized

SEC Table : Default

Elem	Wt %	At %	K-Ratio	Z	A	F
O K	9.30	48.91	0.0163	1.2618	0.1392	1.0000
AgL	27.76	21.66	0.1709	1.0173	0.6040	1.0022
IrL	54.65	23.93	0.4993	0.9101	1.0040	1.0000
Total	100.00	100.00				

Element	Net Inte.	Backgrd	Inte. Error	P/B
O K	15.89	1.78	4.99	8.95
AgL	85.34	9.66	2.15	8.84
IrL	63.79	12.57	2.66	5.08

kV: 25.00 Tilt: 0.00 Take-off: 35.00 Tc:  
100.0  
Det Type:SUTW, Sapphire Res: 126.60 Lsec:  
30



Ag\_IrO<sub>2</sub> : 2

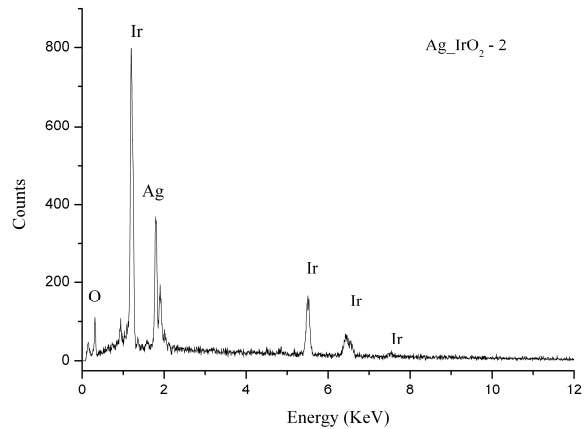
EDAX ZAF Quantification (Standardless)  
Element Normalized

SEC Table : Default

Elem	Wt %	At %	K-Ratio	Z	A	F
O K	9.19	47.98	0.0160	1.2598	0.1383	1.0000
AgL	30.41	23.55	0.1930	1.0145	0.6239	1.0027
IrL	50.45	21.92	0.4590	0.9071	1.0031	1.0000
Total	100.00	100.00				

Element	Net Inte.	Backgrd	Inte. Error	P/B
O K	16.81	3.19	5.51	5.28
AgL	104.00	10.93	2.08	9.52
IrL	63.30	13.89	2.90	4.56

kV: 25.00 Tilt: 0.00 Take-off: 35.00 Tc:  
100.0  
Det Type:SUTW, Sapphire Res: 126.60 Lsec:  
27





## 6.1. Acknowledgements

- I'm very thankful to my supervisor Prof. Dr. Dr. h.c. M. Jansen for giving me the chance to be part of his research group, working on a modern and very challenging topic.
- My special thanks to Prof. T. Schleid and Prof. C. Stubenrauch, as co-referee and co-examiner respectively.
- I also would like to thank to my 3 supervisors – Dr. C. Oberndorfer, Dr H. Kabbour and Dr. D. Pitzschke for their passion and grateful advises during my work. A bit deeper I'd like to thank Dragan, actually he spend the most time (one and half year) with me and had the hardest part of the supervision – revising my writing... as a volunteer.
- I möchte meinen Dank an alle meine Kollegen, die diverse Messungen für meine Doktorarbeit durchgeführt haben, ausdrücken: Marie-Luise Schreiber für Elementanalysen, Thomas Pilz für die Impedanz Messungen, Moritz Stahl für DSC Messungen, Jakob Wilfert für TG – DTA Messungen. Ebenso denen, die nicht in unserem Arbeitskreis sind - Fr. Siegle und Fr. Brücher für die Durchführung von Leitfähigkeit- und SQUID Messungen, Dr. D. Samuelis and L. Fu für die galvanischen Messungen. Danke sehr an Fr. V. Duppel für die TEM Messungen und die Hilfe bei deren Interpretation.
- Thanks a lot to Prof. Maria Antonia Señaris-Rodríguez and Susana Yáñez Vilar (Post Doc in her group) for Seebeck coefficient measurements and for much more....
- Ich möchte mich bei Hanne und Jürgen Nuss bedanken – für die Einkristallmessungen und die Diskussion der Ergebnisse, Hanne zudem für ihre hilfreichen Ratschläge und für die Zeit, die sie sich genommen hat, um mir zu helfen. Bemühe dich sehr mit deiner Habilitation, sonst wäre dein Talent vergeudet, was als großer Nachteil für künftige Studenten betrachtet werden muss.
- Unsere frühere Sekretärin Jeanette Schüller-Knapp und die aktuelle Sabine Paulsen verdient meinen großen Dank für deren Unterstützung und Hilfe in allen möglichen Bereichen.
- Ich möchte mich bei meinem Ex-Bürokollegen und gutem Freund Martin Schulz-Dobrick für alles bedanken. Danke Martin für deine unemotionelle (ist hier positiv gemeint) und mit klarem Kopf geäußerte Meinung; jetzt sieht die Welt schon anders für mich aus....

- Danke schön an meinen aktuellen Bürokollegen Volker Dietrich, du hast die Vanya-Belastung (Nerven – Ausdauer - Test) gut und ohne erkennbare Schäden überstanden!
- Ein spezielles Dankeschön an Denis Kusevic – der HiWi (auch bekannt als der Sklave)! Danke Denis, dass du immer verantwortungsvoll und motiviert im Labor gearbeitet hast.
- Danke schön an Sabine Prill-Diemer und Denis Braginez. Ihr seid sehr gute Menschen und gute Freunde.
- Thanks to Katarina Djuris, for being a good college and brilliant friend. Thank you Katja!
- Специални благодарности на моите родители Таня и Годор Тодорови за безусловната подкрепа, голямата любов и вяра в мен. Благодаря ви мамо и татко! Искам да благодаря и на всички останали членове на чудесното ми семейство сестра ми Петя, Киро, милата ми леля Ваня и братовчедка Рали (и нейното семейство) както на любимите ми баба и дядо, на баба ми Иванка, която не доживя да ме види Доктор... Благодаря ви!
- And my special thanks to my masterpiece - my daughter Eva, thank you my sweetheart, you make my life beautiful and make me strong, I love you. Furthermore thanks to my husband Dr. Kalin Simeonov!

## 6.2. List of Publications:

1. V. Todorova, M. Jansen, Synthesis, structural characterization and physical properties of a new member of ternary lithium layered compounds -  $\text{Li}_2\text{RhO}_3$ . *Z.Anorg.Allg.Chem.*, 2010, DOI: 10.1002/zaac.201000349
2. V. Todorova, A. Leineweber, L. Kienle, V. Duppel, M. Jansen, On  $\text{AgRhO}_2$ , and the new quaternary delafossites  $\text{AgLi}_{1/3}\text{Ir}_{2/3}\text{O}_2$  and  $\text{AgLi}_{1/3}\text{Rh}_{2/3}\text{O}_2$ , synthesis and analysis of real structures, In preparation

## 6.3. Curriculum Vitae

### Personal

Name	Vanya Todorova Todorova
Date of birth	06.05.1978
Place of birth	Sofia, Bulgaria
Nationality	Bulgarian
Marital status	married (1 daughter)

### Educational Background

03/2006 – present	MPI-FKF, PhD Student Doctoral Thesis: Oxide based functional materials through solid state and electrochemical synthesis
10/2004 – 07/2006 (Distance study)	Master in Economics, Marketing, Bulgarian Academy of Sciences, Sofia, Veliko Turnovo University State exam
10/1997 – 07/2002	Master in Chemistry, Sofia University St. Kliment Ohridski Master Thesis: Mass-spectral analysis of flavanoids in <i>Crataegus Oxycantha</i> L.
09/1993 – 06/1997	Technical School of Chemistry, Sofia
09/1993 – 06/1997	Deutsches Gymnasium, Sofia
09/1985 – 06/1993	Elementary and secondary school, Sofia

Hiermit versichere ich an Eides statt, dass ich diese Dissertation unter Verwendung der angegebenen Hilfsmittel selbständig angefertigt und bisher noch keinen Promotionsversuch unternommen habe.

Stuttgart, den

Vanya Todorova